TANAMI

22.3 GHz

8.4 GHz

0.1 pc

HIGH RESOLUTION VLBI OBSERVATIONS OF CENTAURUS A

Diplomarbeit von Cornelia Müller

Friedrich-Alexander-Universtität Erlangen-Nürnberg
Dr. Remeis- Sternwarte Bamberg & ECAP

High resolution VLBI observations of Centaurus A

Diplomarbeit
im Studiengang Diplom Physik
an der Friedrich-Alexander-Universität Erlangen-Nürnberg

vorgelegt von

Cornelia Müller

geboren am 23. Januar 1986 in Nürnberg

Dr. Karl Remeis-Sternwarte Bamberg & ECAP

Betreuer:

Dr. Matthias Kadler
Prof. Dr. Jörn Wilms

Bamberg, 26. November 2010

Zusammenfassung

In meiner Diplomarbeit stelle ich die Auswertung von hochauflösenden *Very Long Baseline Interferometry (VLBI)*-Beobachtungen der Zentralregion der Radiogalaxie Centaurus A vor. Radiolaute aktive Galaxienkerne (AGN) gehören zu den faszinierendsten astronomischen Objekten. Charakteristisch sind ihre stark kollimierten Materieausflüsse, die Jets, die besonders im Radiobereich des elektromagnetischen Spektrums sichtbar sind. Die Jetentstehung und die Wechselwirkung von Jets mit dem intergalaktischen Medium ist mit der Sternentstehungsrate und der Entwicklung sowie dem Wachstum von Galaxien verknüpft. Cen A ist ca. 13 Millionen Lichtjahre enfernt und ist somit die nächste aktive Galaxie in unserer kosmischen Nachbarschaft. Die lineare Ausdehnung ihrer Radiojets erstreckt sich auf Skalen von Lichttagen bis hin zu Tausenden von Lichtjahren. Ihre auf die Himmelssphäre projizierte Fläche ist 20 mal so groß wie die des Vollmondes. Aufgrund der geringen Entfernung eignet sich dieser AGN besonders, um die grundlegenden physikalischen Prozesse solcher Objekte zu erforschen. Die Basis des AGN-Standardmodells bildet ein supermassives schwarzes Loch (SMBH) im Zentrum der umgebenden Galaxie, welches Materie akkretiert. Ein Teil des einfallenden Materials wird dabei ausgestoßen und bildet senkrecht zur Akkretionsscheibe Jets aus. Diese zentralen Bestandteile eines AGNs sind von einem absorbierenden Staubtorus und Gaswolken von verschiedener Geschwindigkeit und Dichte umgeben. In Abhängigkeit der Beobachtungsrichtung bezüglich der AGN-Komponenten versucht dieses fundamentale Modell die verschiedenen, beobachtbaren Erscheinungsformen von AGN zu erklären. Um diese Verallgemeinerung in Verbindung mit theoretischen Jetmodellen zu prüfen, sind hochauflösende Radioaufnahmen zusammen mit simultanen Beobachtungen über das gesamte elektromagnetische Spektrum nötig. Im Rahmen des TANAMI-Programms (*Tracking Active Galactic Nuclei with Austral Milliarcsecond Interferometry*) wurde Cen A zwischen November 2007 und September 2009 viermal bei 8.4 GHz und einmal bei 22.3 GHz beaobachtet. TANAMI führt mit Teleskopen in Australien, Südafrika, Chile und in der Antarktis VLBI-Beobachtungen am Südhimmel durch, wobei Winkelauflösungen von Millibogensekunden (mas) erzielt werden. Die resultierenden Radiokarten zeigen mit nie dagewesener Auflösung den Jet und Counter-Jet von Cen A. Darunter ist das bisher am höchsten räumlich aufgelöste Bild eines AGN-Jets, welches deutlich Strukturen mit Ausdehnungen von nur ∼0.02 pc erkennen lässt. Mit zeitgleichen Beobachtungen in beiden Frequenzbändern lässt sich eine detailreiche Spektralindexkarte des Jets erstellen, welche mehrere optisch dicke Bereiche aufzeigt. Dieses Ergebnis hilft die möglichen Entstehungsregionen der detektierten hochenergtischer Strahlung zu lokalisieren. Die Zeitentwicklung der 8.4 GHz-Beobachtungen ergibt eine sehr komplexe Kinematik des Jetflusses mit einer scheinbaren Geschwindigkeit von ∼0.2c. Allerdings weist die Jetstruktur erhebliche Inhomogenitäten durch Wechselwirkungen mit dem umgebenden Medium und durch innere Einflüsse auf. Zwei Merkmale sind in allen Radiokarten besonders auffällig: Bei einer Entfernung von ∼3.5 mas vom Kern wird eine leuchtkräftige, stationäre Komponente detektiert. Im äußeren Jetbereich, ∼23 mas vom Kern entfernt, ist Störung des Jetflusses erkennbar, wobei es zu einer lokalen Verbreiterung des Jetkegels kommt. Die graphische Darstellung und Auswertung der VLBI-Beobachtungen führt zu einem komplexen Bild des Jets von Cen A. Diese Ergebnisse geben Aufschluss über die Bildung und die Strahlungsmechanismen von Jets im Allgemeinen.

Abstract

In this diploma thesis I present the analysis of Very Long Baseline Interferometry (VLBI) observations of the radio galaxy Centaurus A resolving its central region down to sub-parsec scales. Radio-loud active galactic nuclei (AGN) are among the most exciting astronomical objects, exhibiting highly collimated plasma outflows, called jets. Their formation and interaction with the intergalactic medium is connected with the star forming rate, and the evolution and growth of galaxies. At a distance of about 13 million lightyears, Cen A is the closest active galaxy showing powerful jets from scales of lightdays to thousands of lightyears. Due to its proximity, it is an exceptional laboratory for studying the underlying physics and emission mechanism of AGN in general. The standard model for radio-loud AGN assumes a supermassive black hole in the galaxy center, accreting material which is partially released in form of jets perpendicular to the accretion disk. The black hole and the disc are surrounded by a dusty absorbing torus and gas clouds with different velocities and densities. The variety of different observed AGN types can be explained by this unified model considering different orientations of these basic components with respect to the line of sight. In order to test this unification scheme and theoretical jet models, high resolution radio images combined with quasi-simultaneous multiwavelength observations are required. Within the framework of the Southern Hemisphere VLBI monitoring program TANAMI (Tracking Active Galactic Nuclei with Austral Milliarcsecond Interferometry) Cen A was observed between November 2007 and September 2009, four times at 8.4 GHz and one time at 22.3 GHz. In the resulting radio images of the central region, the jet-counterjet system is imaged with unprecedented angular resolution. The TANAMI radio interferomter array, consisting of telescopes in Australia, South-Africa, Antarctica, and Chile, achieves milliarcsecond (mas) angular resolution. This results in the so far highest-linear-resolution image of an AGN jet, uncovering for the first time features on a linear scale of only ~ 0.02 pc. With simultaneous dual-frequency measurements, a detailed spectral index map of the sub-parsec scale jet is obtained revealing several distinct optically thick emission regions. The putative origin of the detected high energy emission can be constrained with this result. The time dependent analysis of the four TANAMI observations at 8.4 GHz reveals a very complex kinematical behaviour of the jet. An overall apparent motion of $\sim 0.2 c$ is determined. However, the jet shows an inhomogeneous structure due to possible interaction with the ambient medium and internal disturbances like shocks. Two prominent stationary features are seen. At a distance of ~ 3.5 mas from the core, a striking compact feature without significant motion is detected in all images and at both frequencies suggesting a standing shock. Further downstream at ~ 23 mas, the collimated flow is disturbed by an obstacle causing a local broadening of the jet cone with subsequent recollimation. The VLBI imaging and analysis leads to a complex jet appearence of Cen A giving valuable information about jet formation and emission mechanism.

# Contents

1 Radio astronomy and the radio sky

EVER since Galileo Galilei first investigated the sky in 1609 with his optical telescope, people endeavored to improve techniques for an increasingly better view on distant objects in our solar system, in our host galaxy, the Milky Way, and far out to the borders of the Universe. The pursuit of knowledge and curiosity pushes astronomers to look deeper into the sky, to discover extraordinary objects and to "perceive whatever holds, the world [and the universe] together in its inmost folds"[1]. Astronomical research is the science which addresses the old desire of mankind to learn, where and how creatures on planet Earth fit into the environment of the Universe. Therefore its discoveries had always an impact on culture and on everyones life. Beyond the observations in the optical part of the electromagnetic spectrum, a large variety of astronomical objects were not detectable until the start of multiwavelength astronomy. Modern astrophysics studies the sky with different observing techniques for the whole frequency range, from gamma to radio waves. Thanks to the (accidental) detection of Galactic radio waves by Karl G. Jansky in 1933, the following early radio observations were the starting point for revealing the optically invisible space (Verschuur, 2007; Burke & Graham-Smith, 2002).

With his "merry-go-round", a radio antenna receiving at 20.5 MHz and mounted on a turntable, K. G. Jansky identified, during measurements for a transatlantic radio telephone service, a weak radio signal coming from outside the solar system (Jansky, 1933, 2005) – by this serendipity, radio astronomy was born. Radio astronomy addresses cosmic waves of wavelengths of tenth of centimeters to several meters. For visible light ($\sim 400\ldots 700\,\text{nm}$) and for radio waves the Earth's atmosphere is transparent (optical and radio window), permitting to observe with ground-based facilities. Radio telescopes operate similarly to optical ones, focusing light, at a certain observing (receiving) frequency, from distant objects with parabolic reflectors. However, due to the long wavelengths, radio antennas need to have large reflectors up to several meters (e.g., Effelsberg 100 m-telescope) to reach good angular resolutions. The cosmic radio emission is comparably weak[2] and on top of that it has to compete with the man-made radio signals for, e.g., television or communication. Thus, astronomical measurements have to deal with disturbances or radio interference effects. Radio emission from cosmic objects can originate basically from two processes: thermal

---

[1] adapted from J. W. v. Goethe's "Faust"
[2] At $\sim 900\,\text{MHz}$, the third brightest cosmic radio source besides the sun would be a mobile phone (power of 2 Watt) placed on the moon, right after the supernova remnant Cassiopeia A and the radio galaxy Cygnus A.
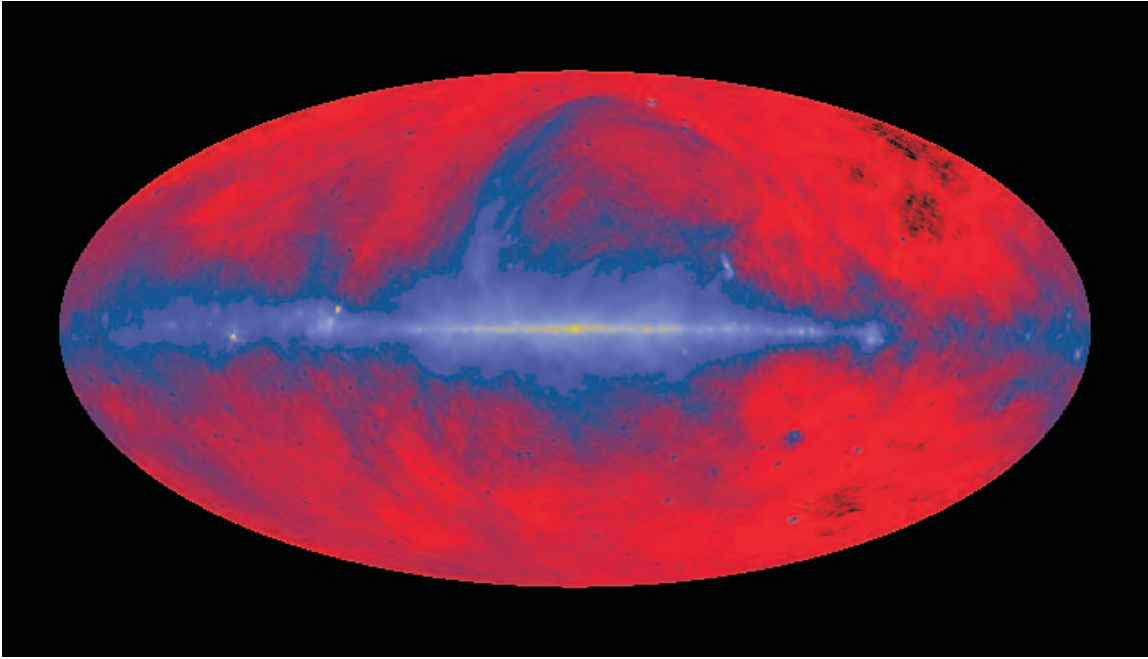
Figure 1.1: 408 MHz all-sky-survey of Haslam et al. (1982) made with the Jordrell-Bank, Parkes and Effelsberg antennas. The sky is shown in Galactic coordinates, with the radio bright Galactic center and radio emission mainly from starburst regions, supernova remnants and radio galaxies.

black body radiation (described by Planck's law) and non-thermal synchrotron radiation (see Sect. 3.2). An all-sky-view at 408 MHz (Fig. 1.1) shows the overall distribution of radio emission. In contrast to optical emission, which is mainly emitted from stars and thus clustered as pointlike sources in the Galactic plane, the radio view reveals large scale structures of diffuse emission. The pointlike radio sources can be identified with powerful sources as supernova remnants or distant (active) galaxies.

The evolution of radio astronomy after the surprising discovery by Jansky was mainly dominated by the development of radar techniques during World War II. Only Grote Reber carried on the investigations started by Jansky and constructed the first all sky map in the radio band showing salient structures of the Galactic radiation with maximal brightness around the center of the Milky Way (now known as Sagittarius A; Reber, 1940, 1944). He was one of the pioneers of radio astronomical research and thanks to his work, after World War II, the invention progress in radar techniques and receiving devices pushed the first non-optical branch of astronomy. Begelman et al. (1984) gave a detailed disquisition of the development of extragalactic radio astronomy, highlighting the identification of "radio stars" with radio galaxies (Baade & Minkowski, 1954), the detection of extended radio emission in powerful nearby galaxies like Cygnus A, or the discovery of quasars ("quasi-stellar radio object") by Schmidt (1963). Further developments in imaging techniques made it possible to build radio interferometers to use not only the amplitude but also the visibility phase of the incoming electromagnetic waves (see Chapt. 4), leading to the highest achievable angular resolution for astronomical observations. More details on the development

of high resolution radio astronomy are reported by Kellermann & Moran (2001). Hence, radio astronomy provides one of the most powerful tools to investigate the sky on smallest accessible resolution scales, from planets to the most distant extragalactic objects. First big radio surveys were conducted in the early 1950s, e.g., the Cambridge Radio Surveys resulting in the 3C Catalogue (Edge et al., 1959) including first detections of famous extragalactic sources like 3C273 or 3C545.3. Since radio astronomers provide the highest spatially resolved sight into space, radio monitoring seeks also to answer questions concerning galaxy formation or evolution of the universe as a whole. Taking advantage of the close connection to other wavebands, radio observations are indispensable for the framework of multiwavelength studies (see e.g., Sect. 5.1.2).

In this diploma thesis, the focus lies on high-resolution radio observations of the subparsec scale jet of the closest radio galaxy Centaurus A, hereafter Cen A. This object is classified as an active galactic nucleus (AGN). In Chapt. 2, the general properties and the unification scheme of AGN are presented. The theoretical description of jets , including emission mechanism, formation and kinematical behaviour is discussed in Chapt. 3. The high-resolution observations are made with the techniques of Very Long Baseline Interferometry (VLBI), thus, in Chapt. 4, I put emphasis on explaining the basics of radio interferometry. A short overview of the VLBI data reduction is given. The analyzed data in this thesis are obtained from observations within the framework of TANAMI, a Southern Hemisphere VLBI monitoring program (Sect. 4.2). Chapter 5 addresses first Cen A, the main character of this diploma thesis and describes its properties in more detail (Sect. 5.1). In the following, Chapt. 5 is concerned with the data analysis and results of the dual-frequency Cen A observations. I conclude with an interpretation and discussion of the derived results by constructing a model explaining the observed phenomena (Chapt. 6).

2 Active galactic nuclei

TWO of the main results of early radio astronomical observations were the discovery of the Cosmic Microwave Background (CMB) by Penzias & Wilson (1965) and the identification of a new class of objects due to multiwavelength investigation: Active Galactic Nuclei (AGN), unifying astrophysical appearances like radio galaxies and quasars. In the following, a short outline about AGN will be given, concentrating on basic information based on the textbooks by Krolik (1999) and Schneider (2006).

AGN are among the most spectacular objects in the universe. The term 'AGN' is used for a galactic central region exhibiting powerful radiative phenomena over a broad energy range, which cannot be explained by stellar emission from the host galaxy[1]. Such a galaxy is then denoted as 'active', referring to the presence of powerful multiwavelength emission, contrary to a 'normal' or 'non-active' galaxy dominated by stellar radiation. Figure 2.1 demonstrates their main characteristic: compared to 'normal' galaxies, they feature luminosities thousand times brighter in small volumes ($< 1\,\mathrm{pc}^3$) centered at the galaxy nucleus. For near objects, the host galaxy is visible in the optical, but in multiwavelength images the true amazing nature is revealed. Large-scale structures radiating over the whole range of the electromagnetic spectrum are exhibited, first detectable by non-optical surveys. Optical measurements show redshifted emission lines which manifest the extragalactic origin of AGN. The extreme radiative energy of AGN is most likely produced by accretion onto a supermassive black hole (SMBH) at their center.

The history of AGN research started at the beginning of the 20th century when strong emission lines of high ionization states were detected from NGC 1068 by Edward A. Fath (1909). Carl Seyfert (1943) recognized a class of spiral galaxies with a bright core and strong optical emission lines (*Seyfert galaxies*, see Sect. 2.1). The first suggestion that the AGN power might originate from a very massive, compact object was made by Woltjer (1959). The large radio all-sky-surveys performed in the 1950 and 1960 such as the Cambridge surveys (e.g., Edge et al., 1959) pushed on the field of extragalactic research, so that M. Schmidt (1963) found that AGN are far distant objects. It was realized that AGN can be divided into a radio-quiet and a radio-loud sub-group. Over the last decades, the advent of important space based observatories like *ROSAT* (Voges et al., 1999), CGRO/*EGRET*

---

[1]To first order, stars are thermal emitters. The spectrum of a normal galaxy is a superposition of Planck spectra according to the stellar temperature distribution. Thus, the intensity distribution is concentrated in between IR and UV.
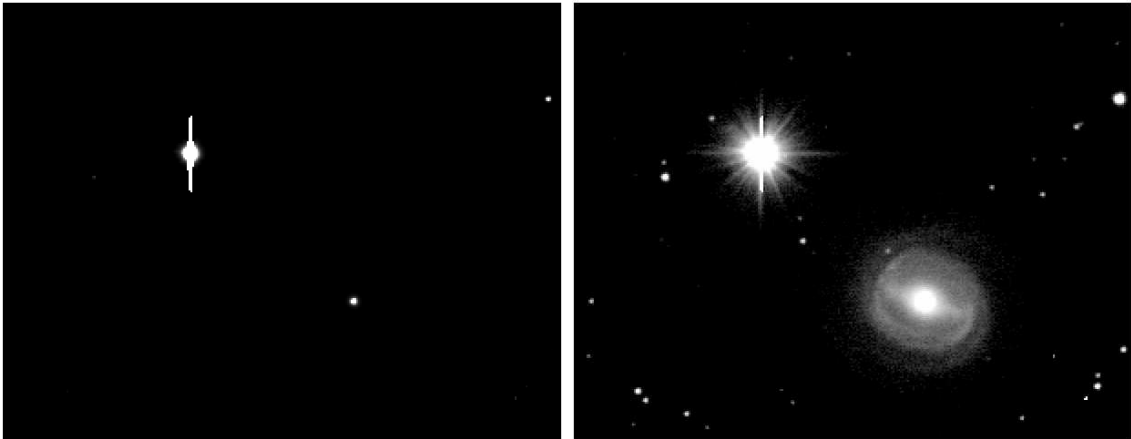
Figure 2.1: Optical image of the galaxy NGC 3783 with linear (left) and logarithmic (right) intensity scale. The latter shows the origin of the bright pointlike emission revealing the underlying host galaxy. At the left sight of the image, a foreground star of the Milky Way can be seen.

(Hartman et al., 1992, 1999), the *Hubble Space Telescope (HST)* (e.g., Williams et al., 1996), or *Chandra* (Weisskopf et al., 2002) gave a more precise, deep and multiwavelength view of the AGN population. Today new missions like, e.g., the γ-ray Large Area Telescope (LAT) on *Fermi Gamma-ray Space Telescope* (e.g., Atwood et al., 2009), address with quasi-simultaneous observations to multiwavelength monitoring programs proceeding questions on AGN formation, emission mechanism and how these objects fit into the "big picture" of the evolution of the universe.

2.1 The different types of active galaxies

General properties

Multiwavelength studies reveal a large variety in the appearance of active galaxies. Moreover the properties seen in the non-optical frequency bands, e.g., the ratio of X-ray or γ-ray to optical flux of active compared to normal galaxies, can be used to find and identify such sources. AGN have certain observable characteristics on which will be focused now, concentrating on the physical appearance and spectral measurement results. Based on these properties they are classified as different AGN types (see below and e.g., Hoffmeister, 1929; Seyfert, 1943; Schmidt, 1963; Fanaroff & Riley, 1974; Lawrence, 1987). The most visually catching property is the high luminosity of the galaxy nucleus ($\sim 10^{42} \ldots 10^{48}\,\mathrm{erg\,s^{-1}}$) compared to the overall brightness of the host (or a normal) galaxy ($\sim 10^{44}\,\mathrm{erg\,s^{-1}}$). Optical images of AGN show a very bright central point source dominating the total intensity and suggesting a very small size of the emitting region (see Fig. 2.1). This appearance led to the definition of "quasi-stellar objects" (QSOs) or "quasi-stellar radio sources" (Quasars), when this puzzling objects were identified with radio sources but not yet resolved. There is only a historical difference between those two terms due to the fact that quasars are seen in

the radio band while QSOs are not. All quasars show emission and often a strong temporal variability over the whole range of the electromagnetic spectrum on timescales of days. The variability depends strongly on the observed wavelength, with shorter variations for higher frequencies (e.g., Wagner & Witzel, 1995; Ciaramella et al., 2004). The time scale gives an approximation of the spatial extent of the radiating source due to the finite speed of light. Moreover, the region radiating at a particular frequency band, where the variability is observed, can be constrained in size. The only way to produce this amount of energy in a volume $< 1\,\mathrm{pc}^3$ is accretion onto a very compact and massive object (Shakura & Sunyaev, 1973). This is the most efficient astrophysical energy release mechanism. Hence, the energetic emission of AGN can be explained by spherical accretion of material onto a SMBH. The *Eddington luminosity* is defined as the maximum luminosity produced by an accreting object with mass M when considering the force balance between gravitation and radiation pressure (Krolik, 1999, Sect. 6.2)

$$L < L_{\mathrm{Edd}} = \frac{4\pi G M m_{\mathrm{p}} c}{\sigma_{\mathrm{T}}} = 1.3 \times 10^{38}\,\mathrm{erg\,s^{-1}} \cdot \frac{M}{M_{\odot}} \tag{2.1}$$

with the gravitational constant G, the Thomson cross section σ_{T}, the solar mass $M_{\odot}$, and the proton mass m_{p}. This is called the *Eddington limit*, describing the maximum of possible energy release when converting potential energy into kinetic energy and radiation. The accreted matter falling onto a black hole usually has angular momentum and thus, is forming an *accretion disk*. In this disk, matter is transported inwards while angular momentum is transported outwards due to friction in the viscous material heating the orbiting medium. An optically thick medium forming a geometrically thin accretion disk has a (stretched) blackbody spectrum with a radial temperature dependence $T(r) \sim r^{-3/4}$ with temperatures of $T \sim 10^5\,\mathrm{K}$. Observations give increasing evidences that massive black holes are present in the center of all galaxies including the Milky Way (e.g., Ghez et al., 1998). It is proposed that the accretion flow onto the central SMBH defines the state of AGN activity, i.e., an increasing amount of material feeding the central engine will cause a "turning-on" of emission and vice versa (e.g., Salpeter, 1964; Di Matteo et al., 2005). The process regulating the inflow of material is not yet understood but it is suggested that galaxy mergers can cause a rise in AGN activity (see also Sect. 3.4.2). The high luminosity of AGN offers the possibility to study their cosmological evolution back to redshifts $z \sim 6$ corresponding to a relative size of the universe compared to today by $a = \frac{1}{1+z}$. AGN show a population maximum around $z \sim 2$ and a decline above $z \sim 3$ (Richards et al., 2006), hence their number is decreasing today. This is is one of the indications for suggesting a close connection between the growth and formation of AGN, cluster of galaxies and the evolution of the universe[2].

Some optical AGN spectra show (highly redshifted) broad and narrow emission lines of transition between high ionization states where the Doppler broadend linewidths display velocities $\sim 10^4\,\mathrm{km\,s^{-1}}$ of the emitting medium surrounding the AGN center. For the innermost regions, especially the research on the iron K_{α} line, which shows often a relativistic broadened shape, sheds light on the behaviour of the inner accretion disk or even of the black hole (e.g., Fabian et al., 2000; Dauser et al., 2010). The radio continuum spectrum

---

[2]This connection is usually termed AGN feedback (see, e.g., Croton et al., 2006).

is determined by non-thermal emission processes indicated by a powerlaw

$$F_\nu \sim \nu^\alpha \tag{2.2}$$

with specific flux F_ν and the spectral (or energy) index α, connected with the photon index $\Gamma = \alpha + 1$. Here, $-0.5 \leq \alpha \leq +0.5$ is called a flat, $\alpha \leq -0.5$ a steep, and $\alpha \geq +0.5$ an inverted spectrum. The spectral shape suggests synchrotron emission to be the main mechanism in the radio band (for more details, see Sect. 3.2). The broad band spectral energy emission of an AGN is observed to be roughly constant over the whole range of the electromagnetic spectrum. Thus, $\alpha = -1$ determines spectra with equal emission flux density per logarithmic frequency bin. However, small deviations can be seen. The νF_ν-spectrum of a (radio-loud) quasar shows a double-humped shape (Fossati et al., 1998), with the synchrotron emission component peaking in the infrared (IR) band and the inverse-Compton component peaking in the X-ray to γ-ray range (for more details, see Sect. 3.3).

The radio-loud active galaxies can exhibit powerful, strongly collimated, material outflows perpendicular to the accretion disk, called *jets* ranging from sub-parsec to Mpc scales (Bridle & Perley, 1984). Their appearance suggests that they are formed at the vicinity of the SMBH and carry energy and matter along. They end in huge radio lobes with bright hot spots of extensions of several 100 kiloparsec when striking the intergalactic medium (see Sect. 3.4). Jets often show inner substructures like 'knots', which are jet features with an enhanced surface brightness, relativistic moving 'blobs', or bends. The emission is mainly observed in the radio band but can also be seen in the X-rays and even in the optical (e.g. in M87, Marshall et al., 2002). Thus it is noteworthy that the visible morphology of AGN is often strongly dependent on the observing frequency.

AGN zoo

Besides these general properties, AGN exhibits several characteristic and dominating features. On the basis of these various appearances a certain notation for different object classes was developed. In principle, AGN can be divided into two sub-classes: radio-loud and radio-quiet (i.e., the radio emission is weak but exists). More distinguishing features are mainly provided by optical measurements. Therefore the following classification scheme is (historically) mainly based on optical measurements.

- **Seyfert galaxies**
  Named after Carl Seyfert, this kind of objects are identified as optical detectable spiral galaxies with an exceptionally bright pointlike nucleus (Seyfert, 1943). Spectral measurements show continuum emission with distinct optical emission lines being highly redshifted. They are divided into two sub-classes: Seyfert type 1 and Seyfert type 2 depending on their spectral (UV/optical) behaviour. Seyfert 1 galaxies show narrow forbidden lines from a low density medium and broad allowed lines from high density matter. The optical spectrum of Seyfert 2 galaxies differs by showing narrow forbidden lines but no broad lines. Moreover a weak continuum and absorption lines from the host galaxy are detected. The full width half maximum (FWHM) of the broad lines can reach a broadening, due to the Doppler effect, equivalent to velocities up to $10^4 \, \mathrm{km \, s^{-1}}$. Seyfert galaxies show only weak radio emission.

- **LINERs**
  An AGN is denoted as a LINER (Low-Ionization Nuclear Emission Region) when showing an optical spectrum like a Seyfert 2 but with a weaker continuum, i.e., the spectrum is dominated by strong emission lines from low-ionization states. These objects belong to the radio-weak sub-class of AGN.

- **Quasars**
  Quasars are the most luminous AGN with bolometric brightness values up to $M < -21.5\,\mathrm{mag}$ (Wilms & Kadler, 2010). Historically, all bright extragalactic objects which appeared pointlike and could not be identified with Seyfert spiral galaxies were denoted as quasi-stellar objects or quasars (see above). They show similar spectral characteristics to Seyfert galaxies, but are brighter with weaker absorption features and weaker narrow lines. They are divided into radio-quiet and radio-loud quasars while 'radio-loud' refers to jet activity (see Sect. 3.4). A clear distinction between Seyferts and (radio-weak) quasars does not exist. In general an AGN is called a quasar when it shows the same optical spectrum like a Seyfert type but its host galaxy is not visible due to the exceeding nuclear intensity. The continuum emission of radio-loud quasars can be described by a powerlaw. Depending on this powerlaw index, these objects are called flat-spectrum radio quasars (FSRQs) compact steep-spectrum sources (CSS). With high angular resolution techniques (i.e., VLBI, see Chap. 4) the innermost regions of radio quasars can be imaged, revealing jet like features.

- **BL Lac objects**
  The name 'BL Lac' originates from the misclassification of the prototype of this class which was thought to be a highly variable star in the constellation Lacerta (Hoffmeister, 1929). BL Lacs are compact (on pc scales) unresolved objects showing a high variability of the continuum emission over the whole energy range. They are characterized as radio-loud AGN with a flat spectrum without significant spectral emission features. In addition, their spectrum is highly polarized indicating synchrotron radiation (see Sect. 3.2). Due to the lack of optical emission lines, it is often difficult to determine a redshift. Hence, the distances of BL Lacs are often unknown, unless (during low-activity states) emission of the host galaxy is detectable. The difference between BL Lacs and FSQRs is described by the total luminosity as FSQRs are more luminous. High resolution radio images of BL Lacs show very compact and mostly unresolved central regions. Since BL Lacs are highly variable, the optical classification can depend on the activity state, i.e., during low emission phases spectral lines may be visible leading to possible misclassifications.

- **OVV quasars**
  OVV (optical violently variable) quasars are objects which show weaker radio emission and hence more optical features in their spectrum than BL Lacs. In the optical, they show a high variability on the scale of days. These objects connect BL Lacs and radio-loud quasars to one group, also known as **blazars**. Blazars are radio-loud objects showing a strong variability in their spectrum and moreover often a high-energy component peaking in the γ-rays.

- **Radio galaxies**
  For the radio-loud sub-class of AGN a complement to Seyfert galaxies can be found, i.e., optical detectable galaxies showing high activity in the radio band. These objects are then called Broad or Narrow Line Radio Galaxies (BLRG/NLRG). Typically the host galaxies are elliptical. Since radio-loud galaxies exhibit double sided jets with different appearances in the radio band, Fanaroff & Riley (1974) created the Fanaroff-Riley (FR) classification scheme with types denoted as FR I and FR II. The structure of FR I objects shows a bright nucleus and two asymmetric jets with broad ends. The total intensity decreases from the center outwards. FR II galaxies are in total more luminous and exhibit bright lobes and hot spots where the jets hit the intergalactic medium. For FR IIs, the lobes and the hot spots are the most striking components with the highest surface brightness. The division into FR I and FR II radio galaxies can be also made by considering their radio luminosity versus the SMBH mass, i.e., their accretion properties (Ghisellini & Celotti, 2001).

Besides the separation into radio-quiet and radio-loud AGN, a classification according to the presence of broad lines can also be made, independent of radio loudness: referring to Type 1 for a broad line spectrum, and in contrast to Type 2 (see Table 2.1).

Table 2.1: Summary of unification scheme

	radio-quiet	**radio-loud**
Type 1	Seyfert 1 radio-quiet quasar	BLRG, BL Lac, OVV radio-loud quasar (FSQR)
Type 2	Seyfert 2 radio-quiet quasar	NLRG (FR I & II) radio-loud quasar (CSS)

(inclination angle ↓)

2.2 Unified AGN model

The similarity of the spectral features detected in BL Lacs, OVVs and radio-loud quasars suggests a close connection or intersection between the different optical classes. In order to assemble all optical classes in one comprehensive AGN theory, the unification scheme was invented. The unified model (Antonucci & Miller, 1985; Lawrence, 1987; Antonucci, 1993; Urry & Padovani, 1995) tries to explain the variety of optical appearances, seen in different AGN classes, with basic components included in every AGN and with determining orientations to the line of sight. The latter can lead to projection and geometrical effects being able to explain the different observed phenomena. A 'model AGN' is composed of (from the center outwards) a SMBH ($M \sim 10^8 M_\odot$), an accretion disk ($r \sim 10^{-3}$ pc), a surrounding broad line region (BLR, $r \sim 0.01 - 0.1$ pc) of a dense and fast rotating medium, a cold dust torus ($r \sim 1 - 10$ pc) and a narrow line region (NLR, $r \sim 100 - 1000$ pc).

The radio-loud sub-class contains also collimated jets of relativistic outflowing material

perpendicular to the accretion disk. The AGN shape differs much from the spherical symmetry implying a strong influence of the inclination angle on the particular appearance. This basic picture (see Fig. 2.2) is designed to explain the main spectral and visible characteristics of the different AGN types only depending on the orientation to the line of sight and the particular luminosity of these components. The model is based on observational constraints and tries to simplify and generalize the AGN object class.

To understand this kind of theoretical generalization, the behaviour (i.e., emission and kinematics) of this basic components is now explained in more detail. As already mentioned above, the extrem power output of AGN and their short-time variability leads to the conclusion that accretion onto a very massive black hole is the relevant power engine. The thermal emission produced in the accretion disk is mainly responsible for the high optical brightness known as the 'big blue bump' in the spectrum. BLR and NLR refer to the relevant formation regions of the broad and narrow lines, respectively. They consist of material and gas clouds of certain densities. The high ionization state and the large width of the broad lines can be explained for an emitting material close to the hot (ionizing) accretion disk. Here the rotation velocity is larger than for the outer regions where the narrow lines are produced. The occurrence of narrow (partially forbidden) lines is due to less dense environment for increasing distance from the SMBH. The cold dust torus surrounding the central region absorbs light and, thus, is blocking the view onto the accretion disk when looking from edge-on. The twin system of jet and counterjet[3] is perpendicularly aligned to the accretion disk. When viewing the jet under a very small inclination angle, relativistic effects (see Sect. 3.4.1) occur and cause enhanced brightness and variability.

With the difference between edge-on and face-on orientations to the line of sight the unification scheme can be summarized. The different spectral features of Seyfert galaxies can be explained by the viewing angle onto the nuclear region of an AGN. Hence, an AGN is classified as a Seyfert 1 type for a view onto the plane of the accretion disk and the dust torus. Here, both the NLR and the BLR are clearly visible. For decreasing viewing angles, the cold dust absorbs the BLR emission - the AGN is classified as a type 2. The same classification principles counts for radio-quiet quasars where the emission of the bright central region exceeds the one of the circumnuclear medium.

For the radio-loud sub-class of AGN the orientation principle works in a similar way. BLR and NLR are visible for certain inclination angles with respect to the torus but also to the jet. The bright jet emission is exceeding the remaining radiation when pointing towards the observer. Blazars (i.e., BL Lacs, OVVs, and radio quasars) exhibit a jet pointing close to the line of sight. BL Lacs appear pointlike even in high resolution images. Therefore it is proposed that the jet has a very small inclination angle, dominating the total intensity in a small volume. The intrinsic spectral varieties are known as the blazar sequence according to their total luminosity (Fossati et al., 1998). In this general picture, the appearance of radio galaxies fits well, since there it is assumed to see an extragalactic radio jet from the side. When imaging a radio galaxy, the jet is clearly detectable. The jets often end in prominent radio lobes which are thought to be unbeamed (see Sect. 3.4.1) when looking along the line of the jet. In contrast, the core emission is expected to be beamed and will

---

[3]The approaching outflow is generally denoted as 'jet' and the departing one as 'counterjet' due to weaker surface brightness caused by relativistic beaming effects (see Sect. 3.4.1).

determine the overall brightness. Thus, with the FR scheme, BL Lacs can be associated with 'misaligned' FR I galaxies and steep-spectrum quasars with FR II objects.

The unification scheme is summarized in Table 2.1. The only difference in radio-loudness can be traced back to the fact that radio-quiet AGN seem to have spiral host galaxies while radio-loud ones are often centered in elliptical hosts. This model is obviously a simplification of the real, not yet resolved central AGN engine and emission mechanism. There is evidence that this model is too simple (e.g., Landt & Bignall, 2008). With improving imaging techniques, observations will reveal a more and more complex structure raising questions on the accuracy of this theory. However, with these components the overall structure and diverse AGN physics can be explained quite well. Results of high resolution images of toroidal dust structures in Seyfert galaxies (e.g., in NGC 4261, Jaffe et al., 1993) or of radio jets in nearby AGN argue for validity of the unification scheme even though a higher complexity of these objects is seen. Concentrating on the connection between the different blazar types, high energy observations (e.g., Sambruna et al., 2010) reconsider the blazar sequence, i.e., the luminosity dependence of the position of the Compton peak (Fossati et al., 1998, and Sect. 3.3), and try to test the radio part of the unified model. More observational evidences are needed to set constraints on the assumptions of the overall model. The dependence on the inclination angle suggests an even distribution of the different types of AGN. In order to test this statistically, large unbiased samples need to be collected. For example, the *Swift* Burst Alert Telescope (BAT) survey of local AGN provides indications for the necessity of a modified model involving additional parameters (Winter et al., 2009). Moreover, all active galaxies which can be classified as 'intermediate' types (showing features allocated to different optical types) do not fit in such a simple picture. A significant fraction of AGN can be found in irregular/peculiar or merger galaxies. Hence, to first order, a simple orientation based model can explain the behaviour of the different AGN types (Barthel, 1989), but in order to address more complicated structures, other variables, like AGN evolution and intrinsic properties, need to be considered. Finally, a reasonable AGN model influences also theories about SMBH growth, star formation, and evolution of both, the galaxies and the intergalactic medium (e.g., Krolik, 1999; Marconi et al., 2004; Merloni & Heinz, 2008; Lagos et al., 2008).
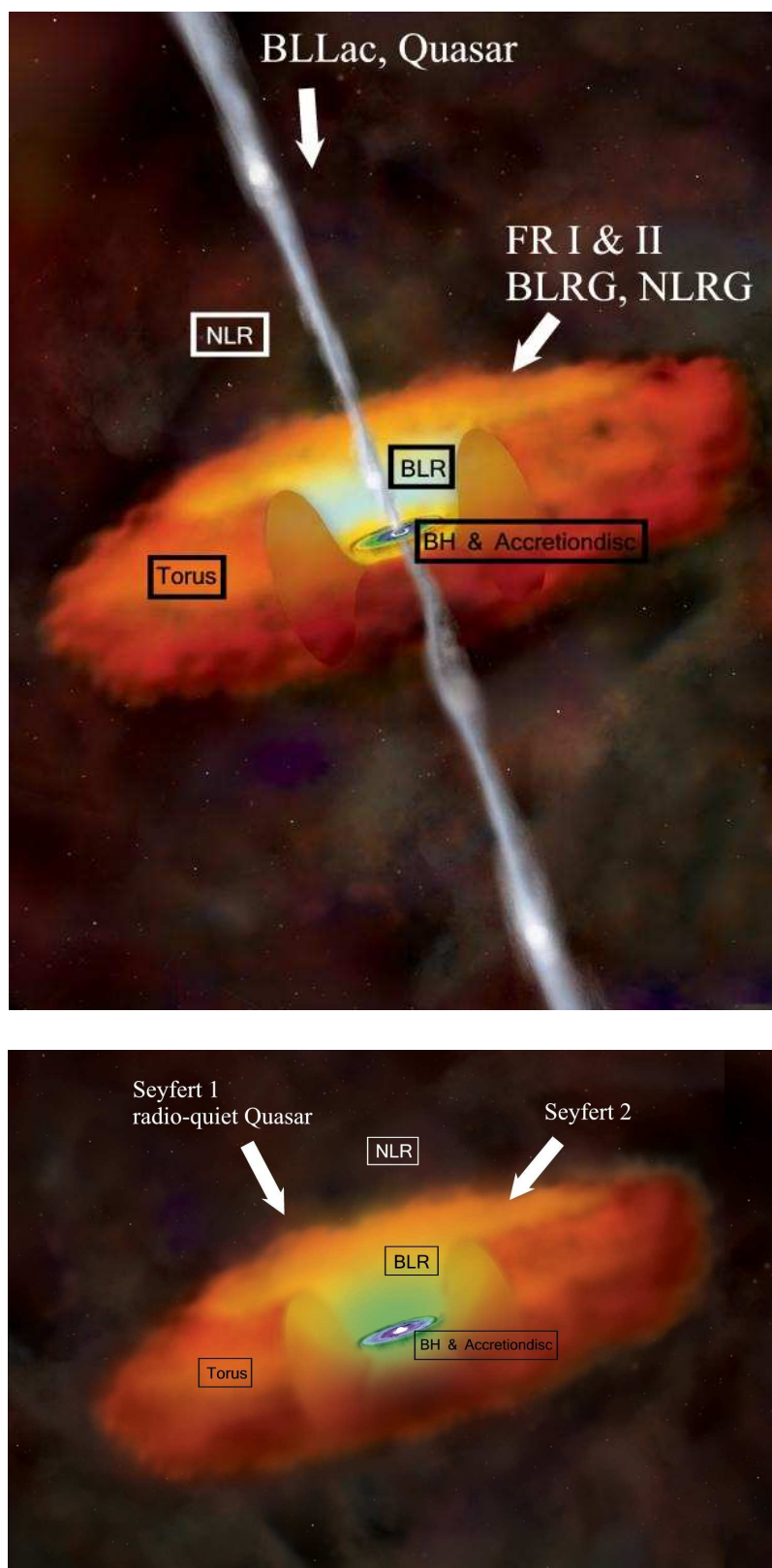
Figure 2.2: Unified model for radio-loud (top) and radio-quiet (bottom) AGN (Image credit: NASA/CXC/M.Weiss). The arrows indicate the viewing angle.

3 Theoretical background

T HE theoretical description of AGN involves the consideration of a possible emission and absorption mechanism producing the observed powerful and specific radiation over the whole range of the electromagnetic spectrum. The observed kind of energy release is dependent on the particular observing frequency and of the AGN region of interest. In the following sections, the main focus lies on the emission and absorption mechanism producing the observed radio spectrum. Especially the bremsstrahlung and synchrotron radiation seen in extragalactic jets is discussed since this work addresses a very close view on the radio jet of the radio galaxy Centaurus A (see Sect. 5.1). In principle, by comparing the measured spectrum with this theoretical considerations, conclusions about the underlying mechanism can be drawn. The energy distribution is discussed by subsequently concentrating also on the formation theory of these collimated plasma outflows. The relativistic effects occuring in extragalactic radio jets are presented in order to explain the observed characteristics later.

3.1 Bremsstrahlung

Bremsstrahlung or *free-free emission* denotes the radiation of accelerated charges in a Coulomb field. A detailed understanding requires quantum electrodynamics, thus, the following considerations refer to Rybicki & Lightman (1979) and give only a short overview.

Classical electrodynamics describe the emission of electromagnetic waves by moving charges. For a single charge q accelerated by an electric field, *Larmor's formula* gives the total emitted power over the solid angle Ω:

$$P = \frac{q^2 \dot{v}^2}{4\pi c^3} \int \sin^2(\Theta) \, d\Omega = \frac{2q^2 \dot{v}^2}{3c^3} \quad . \tag{3.1}$$

The radiation is orientated perpendicular to the direction of motion (dipole pattern) determined by the velocity field. Using the dipole approximation for group of particles, this leads to

$$P = \frac{2\ddot{\mathbf{d}}^2}{3c^3} \quad \text{with} \quad \mathbf{d} = \sum_i q_i \mathbf{r}_i \quad . \tag{3.2}$$

To obtain the spectrum of non-relativistic bremsstrahlung emitted by a single charged particle, quantum mechanics need to be considered since the energies of the photons can

be in the same range like those of the emitting particles. For electron-ion (with charge e and Z, respectively) bremsstrahlung, the electron is the primary radiator since the relative acceleration scales with $\sim \frac{1}{m_{\text{particle}}}$. The radiative power $P = \frac{dW}{dt}$ per volume V and frequency ω is

$$\frac{dW}{d\omega \, dV \, dt} = \frac{16\pi e^6}{3\sqrt{3}c^3 m_e^2 v} n_{\text{e}} n_{\text{i}} Z^2 g_{\text{ff}}(\omega, v) \tag{3.3}$$

with the electron and ion densities $n_{\text{e,i}}$ and the Gaunt factor g_{ff} being a function of the electron energy (according to its velocity v) and the emission frequency. To derive the bremsstrahlung for a certain electron distribution, one needs to know the actual velocities. For a thermal electron distribution (according to the Maxwell-Boltzmann statistics) the emissivity results in

$$\frac{dW}{d\omega \, dV \, dt} \propto n_{\text{e}} n_{\text{i}} Z^2 T^{-\frac{1}{2}} \bar{g}_{\text{ff}} \exp\left(\frac{h\nu}{kT}\right) \quad . \tag{3.4}$$

with the velocity averaged Gaunt factor $\bar{g}_{\text{ff}}$. For optical thin emission (i.e., without absorption), the spectrum is a straight line in a log-log plot. Hence, free-free emission describes the radiation of a free accelerated charged particle (e.g., an electron). The inverse process is called free-free absorption, i.e. , the absorption of a photon by an unbound electron moving in an electric field. The thermal bremsstrahlung absorption coefficient α_{ff} can be derived

$$a_{\text{ff}} \propto T^{-\frac{1}{2}} \nu^{-3} n_{\text{e}} n_{\text{i}} Z^2 \bar{g}_{\text{ff}} \left(1 - \exp\left(\frac{h\nu}{kT}\right)\right) \quad . \tag{3.5}$$

In the Rayleigh-Jeans regime ($h\nu \ll kT$, valid in the radio regime), one gets $a_{\text{ff}} \propto T^{-\frac{3}{2}} \nu^{-2}$, which basically means that for a flat bremsstrahlung spectrum the lower frequencies are affected by absorption.

For the further discussion of jet emission, this self-absorption process of free-free-emission is especially important when looking at radiation absorbed by e.g., an obscurring torus.

3.2 Synchrotron radiation

Synchrotron emission or *magnetobremsstrahlung* is the relativistic equivalent to cyclotron radiation. It concerns extreme relativistic, charged particles moving in a magnetic field and producing a characteristic radiation.

3.2.1 Emission mechanism

The relativistic motion of a charged particle with charge q, velocity v, mass m, and energy E in a magnetic field $\mathbf{B}$ is described by

$$m\gamma\dot{\mathbf{v}} = \frac{q}{c}\mathbf{v} \times \mathbf{B} \quad \text{with} \quad \gamma = \frac{1}{\sqrt{1 - (\frac{v}{c})^2}} = \frac{E}{mc^2} \tag{3.6}$$
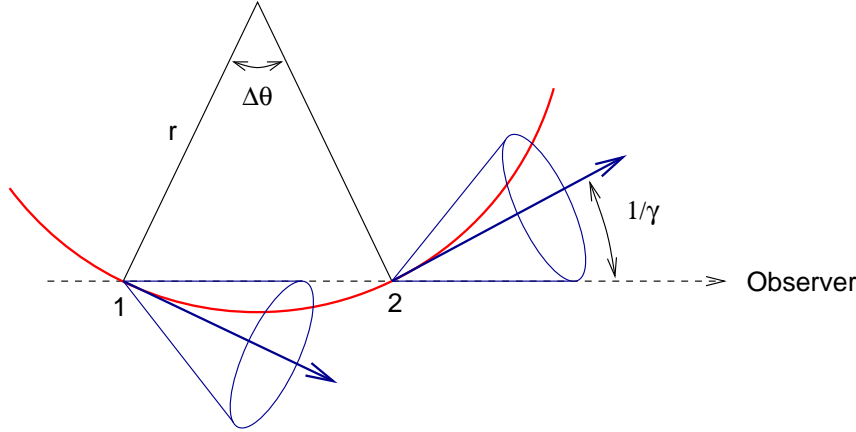
Figure 3.1:
Synchrotron emission cone of a single electron (after Rybicki & Lightman, 1979) moving along a helical path perpendicular to the magnetic field lines.

indicating an helical motion of the particle along the magnetic field lines. The total radiative power of a single electron moving in a magnetic field is then

$$P = \frac{4}{3}\sigma_T c\beta^2 \left(\frac{E}{mc^2}\right)^2 \frac{B^2}{8\pi} \tag{3.7}$$

with $\beta = \frac{v}{c}$ and the Thomson cross section σ_T. The emission is $\propto m^{-2}$, i.e. , synchrotron radiation of more massive particles, e.g., protons, is negligible.

The geometry of the single electron synchrotron emission is shown in Fig. 3.1. The emission of a single electron has a dipole characteristic (Eq. 3.2) in the rest frame of the electron. For relativistic particles, the Lorentz transform into the laboratory system is influenced by the Doppler beaming effect, resulting in an emission cone with an opening angle $\propto \gamma^{-1}$. The observer sees only a short pulse when the emission cone is pointing towards him (lighthouse effect). Depending on the characteristic gyration frequency ω_c with

$$\omega_c = \gamma^2 \frac{eB}{m_e c} \quad , \tag{3.8}$$

Fourier analysis shows, that the observed spectrum is widely spread around $\nu_c = \frac{\omega_c}{2\pi}$ for a short pulse.

In nature a typical electron velocity distribution can be described by a powerlaw with a powerlaw index p

$$n(\gamma)d\gamma = n_0 \gamma^{-p} d\gamma \tag{3.9}$$

(Rybicki & Lightman, 1979, Sect. 6.5). Assuming every electron with a certain energy (velocity) is emitting at a corresponding ν_c, the overall spectrum is calculated as

$$P_\nu \propto \nu^{\frac{-(p-1)}{2}} \tag{3.10}$$

with the *spectral index* α

$$\alpha = \frac{1-p}{2} \quad . \tag{3.11}$$

Thus, the non-thermal synchrotron spectrum of an electron ensemble with a powerlaw velocity distribution is again a powerlaw. It is the superposition of all individual electron
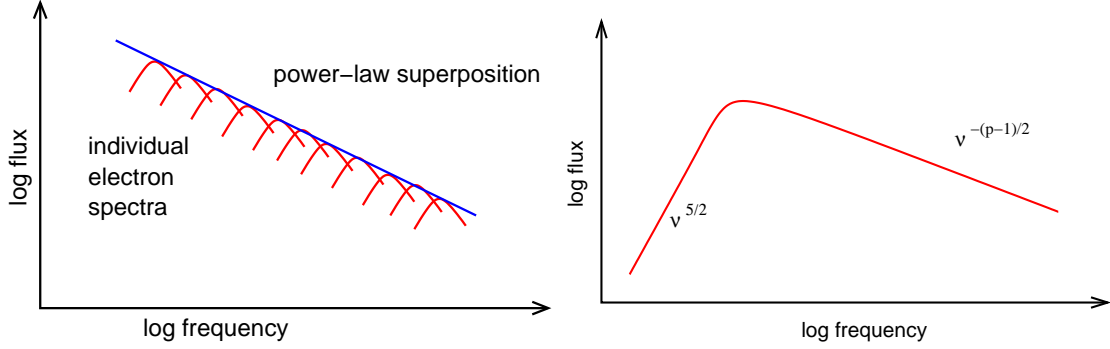
Figure 3.2: Synchrotron radiation of a typical electron distribution (left) giving in total a powerlaw spectrum ($F_\nu \sim \nu^\alpha$) with a spectral index α and synchrotron self-absorption (right) resulting in a cutoff at lower energies (after Shu, 1991).

spectra, depending on the particular gyration frequency (see Fig. 3.2). The energy distribution of the charged particles can be derived from the spectral slope. Synchrotron emission often shows high linear polarization.

3.2.2 Synchrotron-self-absorption and -Compton mechanism

Below a certain frequency ν_t the powerlaw spectrum of a synchrotron spectrum source breaks. This is called the turnover frequency when absorption effects have to be taken into account. Synchrotron self-absorption is a special case, where low energy photons can be absorbed by their synchrotron emitting 'parent' electrons. The resulting spectral shape for a powerlaw electron distribution $\propto E^{-p}$ is

$$P_\nu \propto B^{-\frac{1}{2}}\nu^{\frac{5}{2}} \quad \text{for} \quad \text{low frequencies} \tag{3.12}$$

$$P_\nu \propto \nu^{\frac{-(p-1)}{2}} \quad \text{for} \quad \text{high frequencies} \tag{3.13}$$

which can be seen in Fig. 3.2. Thus, for unabsorbed emission the spectral shape is proportional to the emission function while for an absorbed medium it produces a spectral cutoff (independent of p). The turnover frequency gives the position of this break.

The optical depth (or thickness) τ_ν along a ray travelling path ds is defined as

$$\tau_\nu(s) = \int a_\nu(s')\,ds' \tag{3.14}$$

with the particular frequency dependent absorption coefficient $a_{\nu,\text{sync}} \sim \nu^{\frac{-(p+4)}{2}}$ (here for synchrotron self-absorption). By convention, a medium is called optically thick or opaque when $\tau_\nu > 1$. Contrary when $\tau_\nu < 1$, the medium is optically thin or transparent. Hence, the so called ($\tau_\nu = 1$)-surface of a medium is denoting the border between material layers affected by absorption and those which are unaffected. The ($\tau_\nu = 1$)-surface depends on the observing frequency. The spectral turnover frequency ν_t is hence related to the ($\tau_\nu = 1$)-surface of an imaged medium (e.g., jet, cloud). For higher frequencies this medium is still

transparent, for lower frequencies it becomes obscured and the spectrum is then called 'inverted' having a positive spectral index ($\sim E^{+\alpha}$). The energy distribution of electrons in the milkyway is $N(E) \sim E^{-2.4}$, giving an unabsorbed synchrotron spectral slope of $\alpha \sim -0.7$. This is also observed in most AGN with extended structures (Schneider, 2006).

Generally, the energy of photons can be enhanced or decreased due to Compton scattering of other particles. The *inverse Compton effect* describes the energy gain of photons due to collision with energetic particles. A special case is the Synchrotron Self-Compton (SSC) mechanism, where the synchrotron photons are upscattered to higher frequencies by the same electron population which emitted them. Consequently, this energy transfer leads to a loss of the electron energy (Compton losses). It can be shown (Rybicki & Lightman, 1979) that the SSC peak luminosity and the synchrotron peak (break) luminosity are of the same ratio as the (synchrotron) photon density and the magnetic field density $U_{\mathrm{B}} = \frac{B^2}{8\pi}$

$$\frac{P_{\mathrm{C}}}{P_{\mathrm{S}}} = \frac{U_{\mathrm{photons}}}{U_{\mathrm{B}}} \quad . \tag{3.15}$$

Hence, the Compton luminosity is related to the flux density of the synchrotron emission. The resulting peak frequency ν_{C} of the radiation produced by Compton scattering depends on the peak frequency ν_{S} of the seed photons and the energy of the scattering electrons

$$\nu_C \propto \gamma_e^2 \nu_S \tag{3.16}$$

converting very efficiently a low energy photon to a highly energetic one. Therefore the ratio of the peak frequencies relates to the electron Lorentz factor γ_e (Rybicki & Lightman, 1979; Tavecchio et al., 1998). Moreover the spectral shape (powerlaw slope) reflects the original synchrotron spectrum, since the original electron distribution stays the same, with the identical spectral index. More details on these calculations can be found in Rybicki & Lightman (1979).

The Compton losses can lead to the so called Compton catastrophe. For a very efficient amplification, the electrons are cooled down (Kellermann & Pauliny-Toth, 1969). This results in a limited maximum brightness temperature of $\sim 10^{12}\,\mathrm{K}$ (see Eq. 4.4).

Actual discussions address the origin of the observed Compton peak in radio-loud AGN spectra. It is discussed, whether a single zone SSC process takes place, i.e., emission and scattering at the same location with the same electron population. Alternative theories suggest multiple material layers where the seed photons are not emitted by the 'parent' electrons but by external leptons (External Compton, EC) or are Cosmic Microwave Background (CMB) photons (see following sections for more details).

3.3 Spectral energy distribution of radio-loud AGN

Radio loud AGN are broad band emitters, i.e., their spectrum spans from the radio to the γ-ray regime. A typical blazar spectrum is shown in Fig. 3.3. As already mentioned in Sect. 2.1, spectra of radio-loud AGN are dominated by the jet emission and can roughly be described by a powerlaw. Hence, the amount of energy emitted per frequency bin is overall

Figure 3.3: spectral energy distribution (SED) of Blazars: 3C 273 as a prototypical example (Türler et al., 1999). Top: flux density per logarithmic frequency bin , bottom: flat νF_ν-spectrum (spectral luminosity vs. frequency)
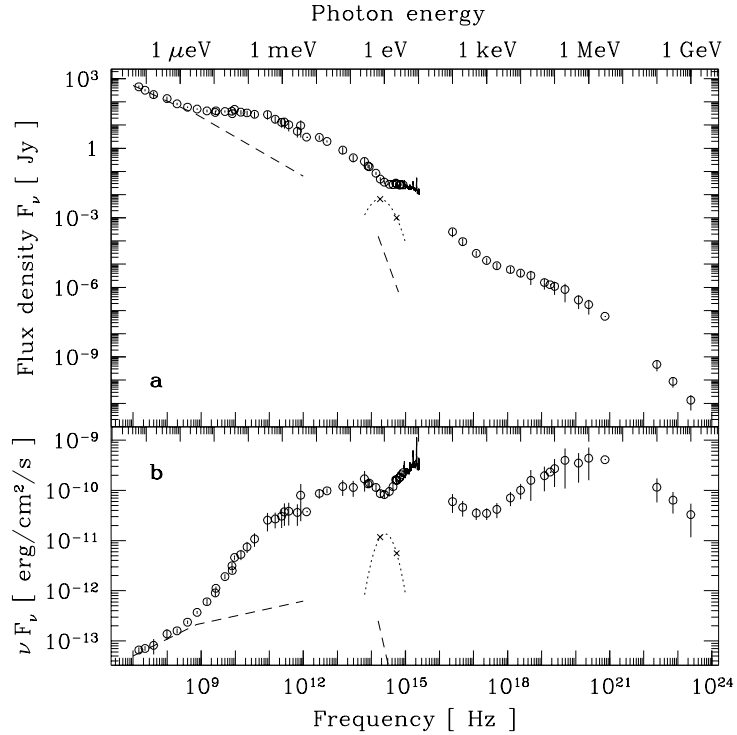
nearly constant indicating non-thermal radiation. Adopting the theoretical description of Sect. 3.2, the broad band emission of AGN can be explained with non-thermal synchrotron emission. The two humps of the spectral energy distribution (SED) are known as the synchrotron peak and the inverse Compton peak, according to Eq. 3.16. There is a general agreement that the low energy synchrotron component is produced by relativistic particles within the jet (Blandford & Königl, 1979; Falcke & Biermann, 1995). Due to polarization measurements of jets, it is known that strong magnetic fields are involved. The high energy hump, peaking in the γ-rays, is either due to synchrotron-self compton (Königl, 1981), external inverse-compton (Sikora et al., 1994), or due to hadronic processes involving the production of pions which decay in energetic photons and neutrinos (Mücke et al., 2003; Becker & Biermann, 2009). SED modeling gives information about the actual emission mechanism and helps to distinguish between these possibilities (e.g., Abdo et al., 2010c).

At lower radio frequencies, the jet spectrum is self-absorbed, i.e., optical thick emission is marked by a spectral break at the turnover frequency ν_t. In general, the self-absorption takes place at the vicinity of the black hole, at the forming region of the jet. Further downstream, the spectrum becomes optically thin. Spectra from the lobes have often steep slopes of $\alpha \sim -0.7$. In contrast, very compact sources, like FSRQs and BL Lacs, show synchrotron spectra with flat indices ($\alpha \sim 0$). For radio galaxies, when seeing the jet edge-on, the spectrum is (overall) steep indicating optically thin emission. The spectrum represents the sum of the single electron spectra, well distributed according to Eq. 3.11. For core dominated sources, due to beaming effects (see Sect. 3.4.1), the spectrum represents a superposition of the inner faster electrons and the outer decelerated ones, resulting in a flat spectral shape (Falcke & Biermann, 1995; Falcke et al., 1995). At low radio frequencies, a spectral cutoff and an inverted spectrum can be seen for denser regions due to absorption.
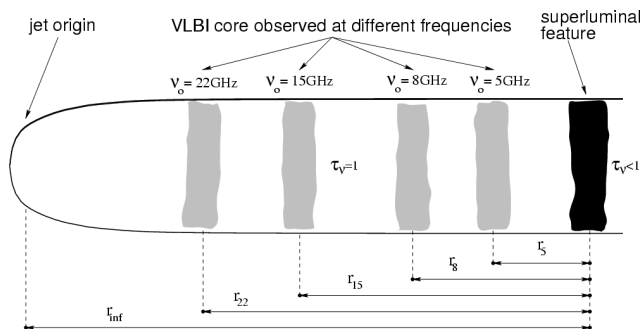
Figure 3.4: Theoretical consideration to frequency dependence of the position of the observed ($\tau = 1$)-surface denoted as 'the VLBI core' (see also 'core shift', Sect. 5.4.1, Kovalev et al., 2008)

With multifrequency measurements the optical depth of different features within a jet can be identified (e.g., Lobanov, 1998). The optically thick regions, especially "the core", are expected candidates for the origin of the high energy emission. The term "radio core"[1] of an AGN usually describes the optically thick region ($\tau = 1$ – surface) which is shifted towards the black hole with increasing observing frequency (see also 'core shift', Fig. 3.4, Marscher, 2008; Kovalev et al., 2008). In most cases, the core is the region with the highest flux density at the upstream end of the jet, close to the central black hole separating jet and counter-jet. The core position depends on the observing frequency and is thus generally not the physical base of the jet (see also Sect. 5.4.1).

Within the blazar regime, the spectrum shows more variations. The double-humped shape of the SED is seen at different frequencies for certain luminosities. This leads to a luminosity classification, known as the 'blazar sequence' (Fossati et al., 1998). The blazars are divided into low-peaked (LBL) and high-peaked (HBL) sources according to the radio luminosity, with the very luminous objects peaking at lower frequencies. This can be explained by a lower initial synchrotron frequency, which leads to a lower Compton bump (Eq. 3.16). The spectral energy distribution is in some cases highly variable. Outbursts or flares are often seen in different wavebands and, moreover, they are correlated. Especially the radio-gamma-connection seen in blazar variability gives information about the physical mechanism taking place at the vicinity of the SMBH and the jet (e.g. Tavecchio et al., 2010; Lähteenmäki & Valtaoja, 2003).

3.4 Extragalactic jets

The emission of radio-loud AGN is generally dominated by the jets, strong collimated outflows, which transport material from the compact central region to the extended lobes. Jets range from sub-parsec to Mega-parsec scales. They can be imaged in detail with VLBI techniques (see Sect. 4.1.3), even for quasars at high redshifts (e.g., Zensus, 1997). High resolution radio observations (e.g., Ojha et al., 2010) obtain close-up images of extragalactic jets of blazars and radio galaxies, showing similar effects and behaviour.

---

[1]It is often also known as "VLBI core", referring to Very Long Baseline Interferometry observations (see Sect. 4.1.3). In VLBI maps, the brightest feature determines the point of origin.
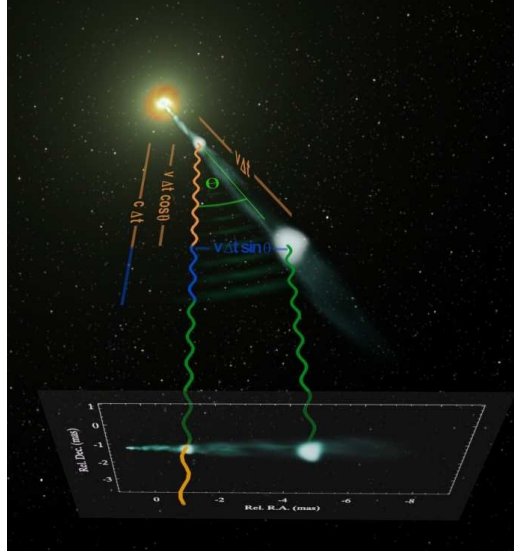
Figure 3.5: Projection effect of superluminal motion
(from http://www.iaa.es/~jlgomez)

3.4.1 Jet propagation

Thanks to milliarcsecond resolution radio observations within the last few decades it has
been shown that AGN jets are no continuously outflowing matter streams but have sub-
structures, like bends or separated matter components moving with relativistic speeds.
With high-resolution imaging one can observe individual jet components of speeds greater
than the speed of light (e.g., Cohen et al., 1977). This phenomenon is called *superluminal
motion* and can be explained as a projection effect. Considering a moving jet blob, with
speed v and ejection angle θ to the line of sight. For the emission of two separated light
signals while travelling a certain distance, the observed velocity of the radiating blob is

$$v_{\mathrm{app}} = \frac{v \sin \theta}{1 - \frac{v}{c} \cos \theta} \quad . \tag{3.17}$$

For $\frac{v}{c} \approx 1$ and small θ, this apparent velocity can reach $v_{app} > c$ (for more details, see
Krolik, 1999, p. 296). For $\sin \theta_C = \gamma^{-1}$, the apparent velocity β_{app} reaches a maximum
with $\beta_{\mathrm{app,max}} = \beta\gamma$ at the critical inclination angle θ_C. This geometric effect is illustrated
in Fig. 3.5 showing the projection of the travel path. The first signal is detected while the
emitting blob is moving towards the observer, implying that the second signal has a shorter
light travelling path. Hence, the observed jet speed is determined on the projected travel
path and the 'shortened' signal separation time. Superluminal motion is strongly dependent
on the angle to the line of sight with higher apparent speeds for smaller inclination angles.

For relativistic moving plasma, further effects occur. Emission of a blob at a certain
frequency ν_{em} is Doppler shifted and is observed as

$$\nu_{\mathrm{obs}} = \frac{\nu_{\mathrm{em}}}{\gamma(1 - \frac{v}{c} \cos \theta)} \quad . \tag{3.18}$$

The relation of observed and emitted frequency defines the Doppler factor $\mathcal{D}$

$$\mathcal{D} = \frac{\nu_{\mathrm{obs}}}{\nu_{\mathrm{em}}} = \frac{\sqrt{1 - \beta^2}}{1 - \beta \cos\theta} \quad \text{with} \quad \beta = \frac{v}{c} \tag{3.19}$$

strongly depending on the jet inclination angle. The Doppler effect influences also the observed flux density $S(\nu_{\mathrm{obs}})$. Since $S_\nu \nu^{-3}$ is Lorentz invariant (for details on argumentation, see Rybicki & Lightman, 1979, Chapt. 4.9), the observed intensity of a relativistic moving blob emitting a power law spectrum ($S \sim \nu^\alpha$) is (Lind & Blandford, 1985)

$$S(\nu_{\mathrm{obs}}) = D^{3-\alpha} S(\nu_{\mathrm{em}}) \quad . \tag{3.20}$$

This is called *relativistic boosting* or *Doppler beaming* amplifying the intensity of a radiating blob which is moving towards the observer and decreasing when departing. In VLBI images (see Sect. 4.1.3) the Doppler beaming is clearly visible as *jet one-sideness*: due to the increasing/decreasing of the intensity for approaching/departing jet components, symmetrically ejected jets appear significantly brighter for the jet pointing to the observer and consequently weaker for the departing outflow ('counterjet'). The relation of the jet-to counterjet surface brightness can be expressed by

$$R = \frac{S_{\mathrm{approach}}}{S_{\mathrm{depart}}} = \left(\frac{1 + \beta \cos\theta}{1 - \beta \cos\theta} \right)^{3-\alpha} \tag{3.21}$$

giving a possibility to determine the inclination angle from measurements of the jet speed (Ryle & Longair, 1967). For a certain flow velocity β, the decrease of the jet ejection angle to the line of sight, results in an enhanced beaming effect.

Cohen et al. (2007) presented the correlations between observed quantities of jets, like apparent superluminal motion and luminosity, and intrinsic parameters (γ, intrinsic luminosity). For a large AGN sample, these quantities can be covered by a theoretical envelope determining limits on the intrinsic speed and luminosity. Moreover, a correlation of high values of β_{app} with luminosity in highly luminous radio jets was found. These considerations assume that the measured apparent speed (with e.g. VLBI observations of jet components) coincidence with the speed responsible for beaming ($\gamma_{\mathrm{component}} = \gamma_{\mathrm{beam}}$) but this is not trivial and has to be reconsidered when explaining high energy emission with the same beaming factor.

Furthermore, it is suggested that γ-ray bright AGN are highly beamed sources, i.e., fast jets pointing very close to the observer (e.g., Sikora et al., 1994; Kovalev et al., 2009). The larger Doppler boosting factors may be responsible for observed higher luminosities and the opening angle of the jet (Lister et al., 2009b; Ojha et al., 2010).

3.4.2 Theories of jet formation

Begelman et al. (1984), Blandford & Rees (1978), and Blandford & Payne (1982) give the basis for the present models explaining physical mechanism and appearance of jets. Considerable progress is made in modeling of jets concluding that the main processes are those
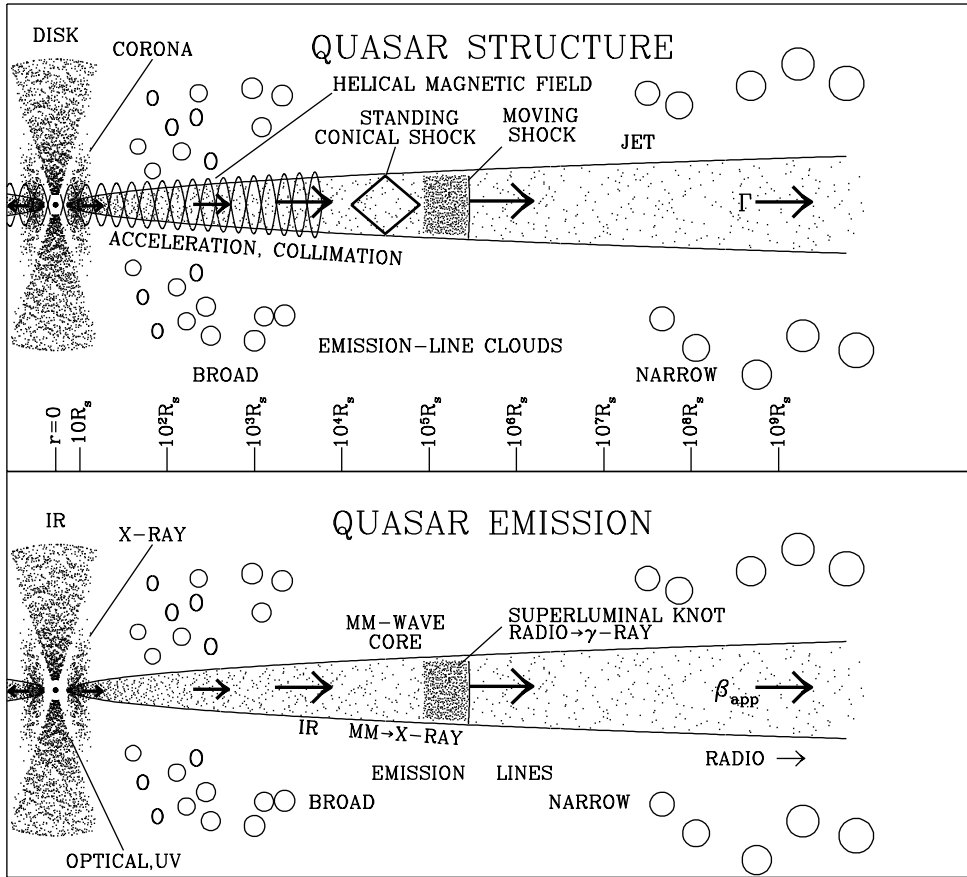
Figure 3.6: AGN jet model showing physical structure and origin of electromagnetic radiation with logarithmic length scale (Marscher, 2009)

of magnetohydrodynamics (MHD) and gas dynamics. In Fig. 3.6, a summary of the phenomenological model of a radio-loud quasar and its emission sites are shown (Marscher, 2009). The gravitational potential of a SMBH at the center of an AGN provides the required large energy tank. Infalling material onto the BH forms a differentially rotating accretion disk (cf., Shakura & Sunyaev, 1973). This differential rotation of the ergosphere of a spinning BH and the disk causes the strong magnetic field to wind up and to form a helical structure. The resulting magnetic coil is perpendicularly aligned to the disk, i.e., parallel to its rotation axis. In order to launch highly collimated plasma outflows, first, angular momentum from the disk has to be transferred and carried away, and secondly, a strong negative outward pressure gradient is required. The latter is given by the toroidal component of the wound-up field which pinches the flow and expels some of the infalling matter. The acceleration to supersonic speeds can be explained by a nozzle near the base of the jet acting like a de-Laval-nozzle (Begelman et al., 1984). Here, the jet is pinched in such a way that subsonic plasma, which is passing through this "bottleneck", is accelerated since the mass flow rate is constant.

The smoothness and self-similarity of the twin jets over several kpc can be disrupted by

instabilities or discontinuities, which are observed as jet knots of enhanced surface brightness. Freely expanding jets, which are mainly described by a higher internal pressure, can be affected by *Kelvin-Helmholtz instabilities*. Due to different velocities at the shearing surface of two fluids, different instability modes can cause jet bending or turbulences (Hardee, 1986; Lobanov & Zensus, 2001). Furthermore, the kinematics and structures of jets are determined by *shock waves* observed as superluminally moving or quasi-stationary jet knots (e.g., Gomez et al., 1993). Pressure oscillations or velocity changes of the flow can result in the formation of a (reverse and forward) shock front. The bulk jet plasma is decelerated abruptly to subsonic velocities while the succeeding material is compressed and increases the jet density locally. Therefore kinematical energy is transferred to internal electron energy and (locally) to magnetic field energy enhancing the local electromagnetic emission. Via the Fermi acceleration (Fermi, 1949), relativistic particles can gain higher energies within the shock due to repeated reflections at the shock fronts. Shock models by, e.g., Marscher & Gear (1985) and Valtaoja et al. (1992) try to explain the frequency dependent evolution of the shock, giving a growth, plateau, and decay stage for the turnover flux S_ν corresponding to the turnover frequency ν_t (see Sect. 3.2.2). The observed stationary jet components (or those with subluminal apparent speeds) are then related to recollimation shocks leading to an amplification of the magnetic field. Superluminally moving features are mostly explained by propagating shock waves produced by surges of newly injected material (e.g., showing up of a new component). However, they can also be due to plasma turbulences or instabilities moving downstream. In any case, the disturbance of the jet flow results in a higher local surface brightness. The frequency of the observed emission is generally dependent on the photon production sites within the AGN core region as seen in Fig. 3.6 (bottom). For example, the radio synchrotron photons can be upscattered to higher energies within a shock (for more details, see Marscher, 2009).

Numerical simulations based on the combination of kinetic theory, Maxwell's equations for electromagnetic fields, and general relativity are invoked to describe the observed jet phenomena. MHD models can account for jet collimation and acceleration to supersonic speeds when regarding accretion onto compact objects for jet-producing sources (Meier et al., 2001; Krolik & Hawley, 2010). When assuming a lower energy density for the magnetic field than for the electromagnetic particles and approximating the plasma with a fluid (Marscher, 2009), the magnetic field is 'frozen in' the plasma and thus, the material will follow the field lines. Such simulation starts with a differentially rotating disk orbiting a compact object. Due to braking forces, angular momentum is transferred up along the magnetic field lines, coiling them to form a helix along the direction of the rotation axis. Hence, the differential rotating magnetic field can produce two opposite collimated jets, taking away rotational energy so that infalling material can be accreted. As it can be shown (Blandford & Znajek, 1977; Meier et al., 2001; Krolik & Hawley, 2010), the spin of the central black hole plays an important role for the formation of jets extracting energy from the ergosphere. For a spinning (Kerr) BH, the jet is driven by the angular momentum of the accretion disk and, moreover, the rotating space, whereas for a non-rotating (Schwarzschild) BH, only the orbital motion of the accretion disk carries the energy. Predictions from simulations show that Schwarzschild BHs cannot produce enough power to launch jets (Wilson & Colbert, 1995). This leads to the suggestion that the 'radio dichotomy of quasars' (Moderski et al., 1998) can be explained if radio-loud quasars contain Kerr BHs and radio-quiet ones host

Schwarzschild BHs. There are indications for a connection between merger and jet activity, since elliptical galaxies host radio-loud AGN while spirals are associated with radio-quiet quasars. Moreover, for negatively (with respect to the accretion disk) spinning BH the jet production is most efficient (Garofalo et al., 2010) supporting the argument of triggering the jet activity through recent merger events.

> We find them smaller and fainter, in
> constantly increasing numbers, and we
> know that we are reaching into space,
> farther and farther, until, with the
> faintest nebulae that can be detected
> with the greatest telescopes, we arrive at
> the frontier of the known universe.
>
> *(Edwin Hubble)*

4 Very Long Baseline Interferometry: Methods and data reduction

RADIO observations of the sky with modern radio telescopes and the advantages of interferometry lead to the highest possible angular resolution of the most distant objects of the known universe. Interferometry involves the superposition of waves coming from the same source but arriving with a certain path difference at different points in the receiving system of different telescopes. By utilizing Fourier transform techniques, interferometry improves the angular resolution of the observational instrument. The combination of two or more (radio) telescopes is called a (radio) interferometer, which can be considered operating as a large antenna of the size of the largest antenna spacing (called baseline), thus increasing the angular resolution of the observing instruments enormously. Research and developments of the last few decades enabled astronomers to build interferometer arrays that span a few kilometers[1], have the size of a continent or even a diameter of the size of the earth operating with the method called Very Long Baseline Interferometry (VLBI)[2] and have one of the array-telescope in space orbiting the Earth[3]. With these instruments angular resolutions down to milliarcsecond (mas) scales can be achieved providing, e.g., excellent radio images of extragalactic jets to study their real-time evolution. The following sections briefly explain the basic principles of single radio telescopes and interferometry. The theoretical framework for VLBI and Earth rotation synthesis is introduced and the characteristics of a VLBI array are highlighted by focusing on the *TANAMI* project as an example[4]. Finally the data reduction techniques which are used to analyze VLBI data, will be presented.

This fundamental introduction is mainly based on the textbooks "Interferometry and Synthesis in Radio Astronomy" by Thompson et al. (2001) and "An introduction to Radio Astronomy" by Burke & Graham-Smith (2002), and the lecture notes about "Multiwavelength Astronomy" by Wilms & Kadler (2009).

---

[1] The most prominent example is the Very Large Array (VLA) (Condon et al., 1998) in New Mexico, USA, with an extent up to 36 km.

[2] e.g., Very Long Baseline Array (VLBA) (Napier, 1995)

[3] space-VLBI, e.g., VLBI Space Observatory Program (VSOP) (Hirabayashi et al., 2000)

[4] The TANAMI project provided the VLBI data of Centaurus A (Sect. 5.1) analyzed in this diploma thesis.

4.1 Radio interferometry

Radio interferometry describes the combination of two (or more) radio antennas to measure incoming radio signals from cosmic sources and the usage of interference effects to achieve highest possible angular resolution. Applications of radio interferometers can be found in the domains of astrometry, geodesy and, of course, in astronomy. To optimize the angular resolution of a single telescope, one uses arrays of antennas operating together like a large single one. This makes it possible, e.g., to measure precisely source positions for astrometry for building up a celestial reference frame of high accuracy (e.g. Bourda et al., 2008), to determine the orientation of the baselines in such a frame or to resolve structures of extragalactic sources with resolutions exceeding those of every other astronomical observing technique.

The development of interferometry in astronomy began at the end of the 19th century when A. A. Michelson built a stellar interferometer using two separated apertures measuring interference fringes. Radio interferometry started with the investigation of advanced signal processing techniques during World War II. The first radio interferometer was the sea-cliff interferometer by Pawsey et al. (1946) which used only one antenna and the sea surface as a second reflector. McCready et al. (1947) mentioned for the first time the possibility to use Fourier synthesis to determine the brightness distribution in the sky. The first astronomical interferometric observations were conducted with a two-element interferometer by Ryle and Vonberg (1952). The invention of the phase-switching interferometer by Ryle (1952) marks the starting point for first survey of radio sources, today known as the 1C catalogue (for details see, e.g. Sullivan, 1991). Ryle & Hewish (1960) proposed the method of Earth-rotation synthesis. With improvements of image processing techniques and construction of large antenna arrays, the first VLBI observations took place in 1967 (Kellermann & Moran, 2001; Clark, 2003).

4.1.1 Radio telescopes

In principle a radio telescope consists of a receiving antenna, a sensitive radio receiver, and a recording system. Conventional radio antennas are parabolic reflectors which are mostly equatorially mounted. An incoming wavefront is reflected and focused to the receiving device. The angular resolution an antenna is determined by the diffraction pattern and can be expressed by the basic formula defined by the Rayleigh criterion

$$\sin(\alpha) = 1.22\frac{\lambda}{D} \qquad (4.1)$$

where α is the angular resolution in radians, D the diameter of the reflector and λ the observing wavelength. The radiation pattern (or reception pattern) of such a single antenna can be seen in Fig. 4.1. It consists of the main beam, whose full width half maximum (FWHM) is defining the angular resolution, and the side lobes, which can cause spurious effects in the detections. It can be described as the Fourier transform of the aperture distribution like the point-spread-function (PSF) or Airy disc for an optical aperture (see below for further explanations). In the simple case of a parabolic reflector, the beam pattern
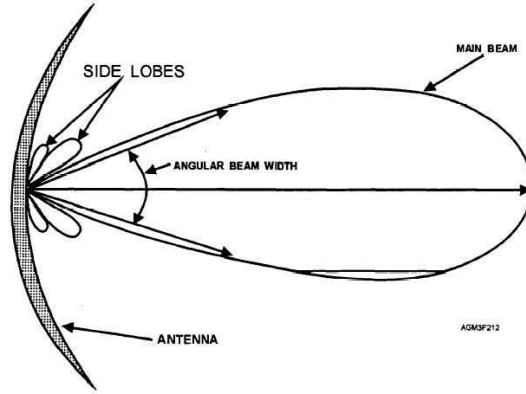
Figure 4.1: Antenna radiation/reception pattern (from `www.tpub.com`)

is described by a sinc-pattern[5]. The received power passed to the antenna output is

$$P = A_{\text{eff}} \cdot S \tag{4.2}$$

with A_{eff}[6] being the effective area of the telescope and S being the incoming total flux density, which is given by

$$S_\nu = \int I_\nu(\theta, \phi) \, d^2\Omega \, d\nu \tag{4.3}$$

where $I_\nu(\theta, \phi)$ denotes the specific source brightness (or intensity) at a given frequency, $d^2\Omega$ the integration over the solid angle, and $d\nu$ the integration over the observed frequency range. In the radio context, by convention, the specific flux density S_ν has the unit *Jansky* (Jy) [$1\,\text{Jy} = 10^{-26}\text{W}\,\text{m}^2\,\text{Hz}^{-1}$]. Furthermore, Eq. 4.2 shows the dependence of A_{eff} on the sensitivity of a radio antenna: the larger the effective area the higher the sensitivity. The incoming signal is then converted into an electric signal at the antenna feed via induced voltage oscillations in a conductor. In radio astronomy, the output quantity of a telescope is called the antenna temperature T_{Ant} (measured in Kelvin). It describes the corresponding temperature of a hypothetical resistor at the receiver input which generates the same output noise power per frequency bandwidth as that at the antenna output at a specified observing frequency. This leads to a useful quantity, the *brightness temperature* T_B which is related to S_ν as

$$S_\nu = \frac{2k_B}{\lambda^2} \int T_B(\Omega) \, d\Omega \quad . \tag{4.4}$$

The Rayleigh-Jeans approximation of the Planck formula for thermal emission is given by

$$T_B = \frac{I_\nu c^2}{2k_B \nu^2} = \frac{1}{\pi r^2} \frac{c^2 S_\nu}{2k_B \nu^2} \quad . \tag{4.5}$$

Consequently and according to Condon et al. (1982) the brightness temperature is defined as

$$T_B = 1.22 \cdot 10^{12} \left(\frac{S_\nu}{\text{Jy}} \right) \left(\frac{\nu}{\text{Hz}} \right)^{-2} \left(\frac{\theta}{\text{mas}} \right)^{-2} \tag{4.6}$$

---

[5]cf. Rayleigh criterion for single slit diffraction
[6]The effective area of an antenna is generally smaller than the real size due to imperfect irradiation.

(with θ being the angular size of the emitting region and ν the observing frequency) which is frequency dependent for non-thermal emitting sources. T_B describes the equivalent temperature of a black body to generate the same amount of power at the same receiving frequency.

4.1.2 Two element interferometer and 1D aperture synthesis

The first interferometric techniques in the optical spectral range were performed by Michelson, who was able to measure angular sizes of some nearby and larger stars. The simplest type of an interferometer consists of two receiving apertures monitoring the same incoming wavefront emitted by a distant source. They are combined to operate as one instrument (see Fig. 4.2) via a *correlator* which matches the two signals. Due to a geometrical delay between the two receivers, interference can occur. Michelson defined the fringe visibility V_M as a measure of the relative amplitude of the interference fringes

$$V_M = \frac{\text{intensity of maxima} - \text{intensity of minima}}{\text{intensity of maxima} + \text{intensity of minima}} \quad . \tag{4.7}$$

For a source with a diameter smaller than the fringe width, this definition leads to $V_M = 1$, i.e., if $V_M < 1$ the source is resolved by the interferometer.

A demonstrative equivalent to the simple two-element interferometer is Young's double-slit-experiment, which can be used to explain the fundamental connection of Fourier optics and interferometry. By looking at the interference pattern of a double-slit aperture irradiated by a light source and considering the Fraunhofer far-field approximation (i.e., the distance between the aperture plane and the observation plane is considered to be much larger than the dimensions of the aperture function), it becomes clear that the function of the diffraction pattern is the Fourier transform of the slit pattern. In other words, the observed intensity distribution $I(x)$ (at the screen) is proportional to the Fourier transform of the intensity distribution in the aperture plane $I(\alpha)$:

$$I(x) \sim \int I(\alpha) e^{2\pi i x \alpha} \, d\alpha \quad . \tag{4.8}$$

This results from Fourier optical calculations. In the case of a slit-experiment the diffration pattern is simply the Fourier transform of a rectangular function, which is a sinc-function.

Now, to make the transition to the radio interferometer, one can imagine the aperture plane to consist of two identical telescopes with a certain spacing b which is generally called the baseline measured in wavelengths (analog to the slit displacement). For simplicity, first a one-dimensional approach will be considered. The observer sees the superposition of the incoming light at both telescopes. The combination of these two signals is done in a correlator, which behaves like a multiplier and integrator (with respect to time)[7]. To get the response of such an interferometer one has to consider the signal paths. The geometrical situation is shown in Fig. 4.2. It will be assumed that the receiver has a narrow bandpass around the observing frequency ν and the inclination angle to the source is θ. The wavefront

---

[7]see phase-switching interferometer Thompson et al. (2001), Sect. 1.3
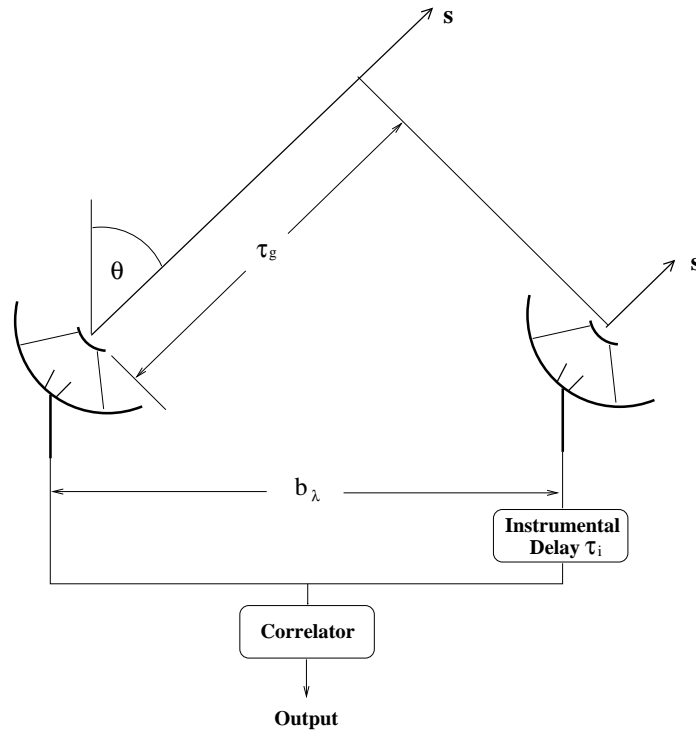
Figure 4.2: Two element interferometer after Burke & Graham-Smith (2002).

arrives at the left antenna with a time delay of

$$\tau_g = \frac{b}{c}\sin\theta \tag{4.9}$$

with respect to the right antenna. This is called the geometrical delay τ_g. At the correlator the two voltage signals are then multiplied and integrated over a time constant which gives the output (in voltage squared) proportional to

$$F = \cos(2\pi\nu\tau_g) = \cos\left(\frac{2\pi\nu b \sin\theta}{c}\right) \quad, \tag{4.10}$$

which is generally called the *fringe function*.

An instrumental time delay τ_i is inserted, so that the net-time delay becomes $\tau = \tau_g - \tau_i$. For tracking the position of the source, it is common to specify a reference position on the sky, which is usually called the *phase reference position*, to which angles of the antenna beam can be measured. Therefore, τ_i is adjusted to balance the geometrical delay τ_g, i.e., the reference position is defined as the direction θ_0 where $\tau_g = \tau_i$ and $\tau_g = \frac{b}{c}\sin\theta_0$. Moreover τ_i compensates bandwidth effects since finite bandwidth diminishes the angular range where fringes appear (delay beam effect).

The resolution of the fringes is determined by the projection of the baseline length onto the sky $b\sin\theta$ (see Eq. 4.10). For this reason, it is common to introduce the quantity u defined as

$$u = \frac{\nu \cdot b \cos\theta}{c} \tag{4.11}$$

which represents the antenna spacing perpendicular to the direction of the reference position. Finally, for an observation of a point source at a position $\theta_0 - \Delta\theta$, the fringe function becomes

$$F(l) = \cos(2\pi\nu\tau) \cong \cos[2\pi\nu(b/c)\sin(\Delta\theta)\cos(\theta_0)] \tag{4.12}$$

$$F(l) = \cos(2\pi u l) \text{ with } l = \sin\theta \quad . \tag{4.13}$$

This is the two-element-interferometer response to a point source where both antennas track the source. It is the real part of the Fourier transform of the intensity of a point source between the spatial domain in the sky (represented by l) and spatial frequency denoted by u.

Considering now extended sources with a certain intensity distribution $I(l)$. The total output power of a single antenna can be expressed as the convolution of the antenna reception pattern $A(l)$ (which is the response to a plane wave) and the intensity of the source (cf. Eq. 4.2). In the case of an interferometer, the overall power pattern must be used, which is defined by the reception pattern of each antenna and by the fringe function (4.10). The interferometer response results in

$$R(l) = \int_{\text{Source}} \mathrm{F}(l')\mathrm{A}(l')\mathrm{I}(l')\,dl' = \mathrm{F}(l')\mathrm{A}(l') * \mathrm{I}(l') \quad . \tag{4.14}$$

The convolution theorem of Fourier transforms

$$f * g \rightleftharpoons \mathcal{F}\mathcal{G} \tag{4.15}$$

describes that the convolution of two functions is equal to the product of their Fourier transforms. This leads to the general expression of the interferometer response:

$$\mathcal{V}(u) = \int_{-\infty}^{\infty} A(l')I(l') \cdot e^{i2\pi u l'}\,dl' \quad . \tag{4.16}$$

The Fourier transform of the flux density distribution is defined as the *Visibility function* $\mathcal{V}$. It is an unnormalized complex quantity (contrary to the original fringe visibility by Michelson, Eq. 4.7), which is measured in units of flux density. The phase of the complex visibility measures the fringe phase in order to deal with resolved and asymmetric sources.

To summarize, the two-element-interferometer output gives a function in the spatial frequency domain, which respresents the Fourier transform of the intensity distribution of the source convolved with the reception pattern. It samples the Fourier space at the spatial frequencies $\pm u_0$ (acting like a filter) with the sampling function

$$S(u) \sim [\mathcal{V}(-u_0)\delta(u + u_0) + \mathcal{V}(u_0)\delta(u - u_0)] \tag{4.17}$$

mainly depending on the length of the baseline (see Eq. 4.11). Hence, varying the spacing of the telescopes leads to different sampling of spatial frequencies and so one obtains more information about the intensity distribution in the spatial domain. This sampling of Fourier components of the source brightness distribution is generally called aperture synthesis. To recover $I(l)$ from the correlator several computational procedures have to be conducted.
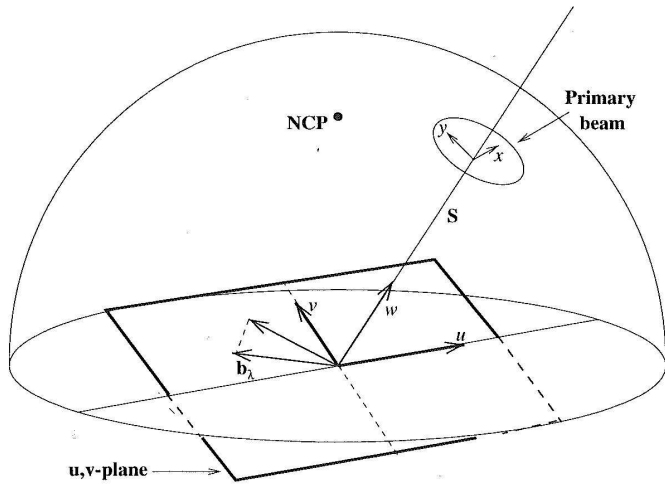
Figure 4.3: (u, v)-geometry with (x, y) stands for (l, m) coordinates in small angle approximation (after Burke & Graham-Smith, 2002, p. 67).

The final resolution limit of this interferometer is defined by the maximum baseline or rather $u_{\max}$.

This 1D-concept can be easily adopted for two-dimensional imaging by amending Eq. 4.16

$$\mathcal{V}(u, v) = \iint_{-\infty}^{\infty} A(l', m')I(l', m') \cdot e^{i2\pi(l'u+m'v)}\, dl'dm' \tag{4.18}$$

with the spatial frequencies $u = \frac{\nu \cdot b \cos\theta}{c}$ and $v = \frac{\nu \cdot b \sin\theta}{c}$ spanning the so called (u, v)-plane. The parameters l and m are the coordinates in the spatial regime, spanning a 2D-space perpendicular to the line of sight in the plane of the source. A single two-element interferometer evaluates the intensity distribution in the sky (during one integration period) at one single spatial frequency (represented by one point in the (u, v)-plane) which is specified by the baseline length b projected onto the (u, v)-plane. The Fourier transform of the source brightness distribution, the visibility, is measured in this plane. The geometry can be seen in Fig. 4.3.

4.1.3 Theory of Very Long Basline Interferometry

In order to significantly improve the angular resolution of radio interferometers, the baseline length needs to be increased. Therefore, the connected interferometer arrays like the VLA were extended to arrays with antennas spread over the globe. Since direct signal processing is then not possible any more, every single antenna output is recorded with storing the exact observation time measured by an atomic clock and the outputs of every telescope pair are correlated offline. The whole VLBI measurement process is illustrated in Fig. 4.4. For exact time measurements, a local oscillator, whose signal is generated by a stable atomic frequency standard, controls the digitization of the measured radio signal at each station by adding a time stamp. The radio signals are then converted to an intermediate frequency (IF), which is low enough to record the signal directly on discs. These storage media are brought together at a central facility and played into the correlator for cross-correlation

and integration[8]. After phase shifting, this results in a set of fringe visibilities $\mathcal{V}_{ij}$ for every pair of antennas i and j, i.e., a set of Fourier components of the brightness distribution of the observed source.

In principle the VLBI techniques resemble the ones for connected-element interferometers, since the fundamental aim of interferometry is always the measurement of coherence properties. However, there are some different practical issues which have to be considered and understood. The atomic frequency standards still have time lags which will cause errors in the local oscillator frequencies and induce phase errors after mixing the signals. Also, (uncorrelated) atmospheric fluctuations above the stations can cause phase noise in the fringes. These offsets in the fringe frequency have to be identified by finding the peak of correlation. This process is called *fringe fitting*. Schwab & Cotton (1983) developed the global fringe fitting technique on the basis of *closure phases*[9], which is superior to the baseline-based fitting (for more details see Thompson et al. (2001), Sect. 9.4). Furthermore, the calibration process is different to a connected interferometer. For a connected array, one finds more easily a calibrator source[10] close to the object of interest, to which the telescope can point to every few minutes for phase reference. This is necessary to correct for phase errors. For VLBI observations the time for alternate pointing is too long and above all, the higher angular resolution makes it more difficult to find suitable (compact) calibrators. Since the technique of phase referencing for VLBI is more complex and requires high instrumental phase stability, VLBI observations often waive absolute position determinations. The obtained measurement results then only include approximate pointing coordinates and the resulting images are scaled with relative coordinates with the origin being the phase center.

The great potential and advantage of radio interferometric observations is the opportunity to improve the (u, v)-coverage by utilizing the Earth rotation. As the Earth rotates, the antenna spacing vector traces ellipses in the (u, v)-plane with the phase reference center as their origin. Depending on the elevation angle of the observed object, these ellipses are deformed to straight lines for very low altitude objects. Since the visibility is a complex

---

[8] The separately recording of signals and subsequent recovering of interference pattern seems to contradict the basic quantum mechanical concept of disturbing the interference by measuring the travel path of a photon. Trying to describe the concept of VLBI in quantum terms leads to the astonishing quantum interference paradox. Burke (1969) states that the phase conservation in the VLBI amplifiers leads to the possibility of subsequent fringe formation. The number of incident photons will be enhanced, giving a stronger interference pattern, but no disturbance is induced. The response of an amplifier has to be consistent with the uncertainty principle $\Delta N \Delta \phi \simeq 1$. To preserve the phase, ΔN should give an uncertainty of at least one photon per unit time at the output of the amplifier. Since every electrical system produces a certain noise (i.e., existence of spontaneous emission), exactly displaying amplitude and phase of one single electron is impossible. Thus, storing of the VLBI receiver outputs and reconstruction of interference pattern is feasible without disagreement with quantum mechanics.

[9] Closure phases are relations between visibility values for all pairs out of three antennas. The sum of these visibility phases is called the closure phase, which is unaffected by phase errors but contains structure information of the source. For a point source the closure phase is always zero. This can be used to check the calibration accuracy and instrumental effects. The best use of closure phases is in the context of phase-self-calibration (see Sect. 4.3), permitting only changes to the measurements such that the closure phases stay constant (Cornwell, 1989).

[10] There are two types of calibrators needed, which ought to be compact sources: 1.) amplitude calibrators with almost constant (known) flux density over a long time interval, and 2.) and phase calibrators with a stable (known) position.
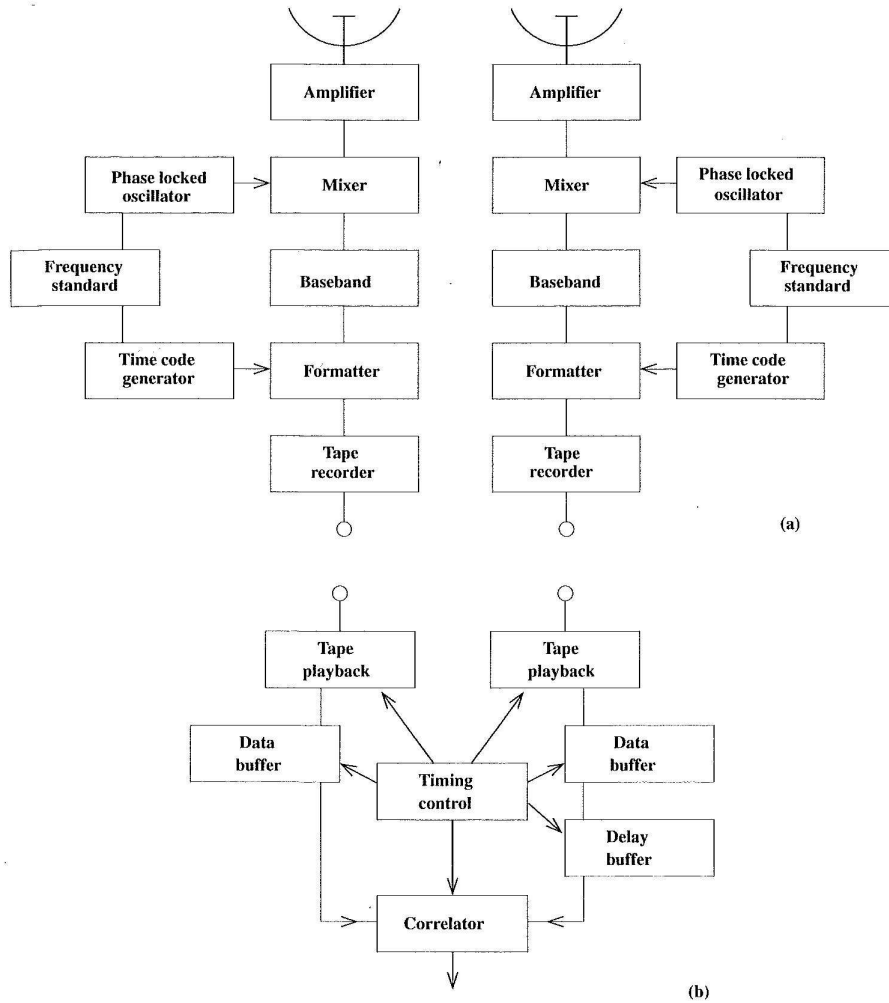
Figure 4.4: VLBI signal processing showing (a) two independent telescopes and (b) the correlator system (after Burke & Graham-Smith, 2002, Sect. 5.4).

quantity, $\mathcal{V}_{ij}^*(u,v) = \mathcal{V}_{ij}(-u,-v)$ leads to two arcs in the (u,v)-plane symmetric to the (u,v)-origin. This movement causes a sampling of the visibility function $\mathcal{V}$ in the spatial frequency domain, as the projected baseline length is the decisive factor (cf. Eq. 4.11 and 4.18), leading to an increasing amount of information about the flux density distribution of the source. This method is called *Earth rotation synthesis*. By combining radio telescopes all over the Earth, the (u,v)-plane can be suitably filled. Long distances bring the highest resolution, while smaller baselines are sensitive to large scale structures. Long baselines correspond to small spatial frequencies and vice versa. Fig. 4.5 shows this scenario for a source at the north celestial pole and a two-element array in east-west direction. In this case the "moving" baseline of a fixed length will provide a sampling of the (u,v)-plane of a concentric circular form. By varying the antenna spacing, the whole spatial frequency domain can be filled up. For non east-west spanned baselines the resulting traces in the (u,v)-plane will look more complicated. A set of N antennas will therefore give a set of
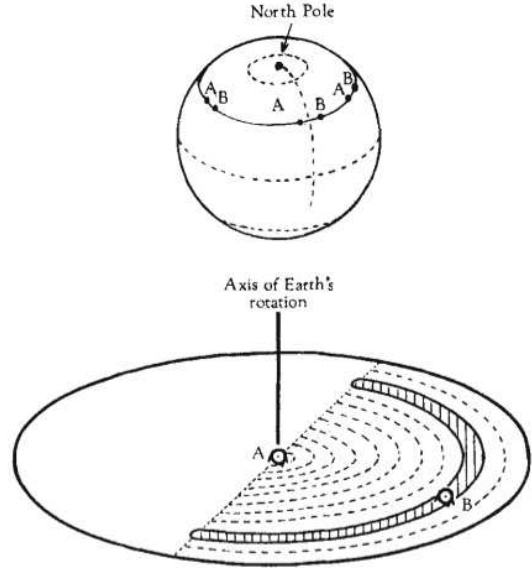
Figure 4.5: Sampling of the (u, v)-plane for a source at the north celestial pole and a two-element array in east-west direction (Ryle, 1962). While tracking the source with a baseline of a fixed length the (u, v)-plane will be sampled in a concentric circular form. By varying the antenna spacing, the whole spatial frequency domain can be filled up.

$\frac{N}{2} \cdot (N - 1)$ visibilities $\mathcal{V}_{ij}$ per integration time period.

The ideal case would be to sample the whole spatial frequency domain, in order to get a full recovery of the real intensity distribution of a source. In practice, this is impossible to achieve and there will always be missing components and $\mathcal{V}(u, v)$ will not be continuously sampled. The quantity which describes the amount of antenna spacing possibilities, i.e., the amount of sampled spatial frequencies, obtainable by a certain array, is the *transfer function* or *spectral sensitivity function*[11] $W(u, v)$. It expresses the limitations for reconstructing $I(l, m)$ due to lack of sampling. It is defined as the autocorrelation function of the electric field distribution $\mathcal{E}(x, y)$ across the aperture, where x and y are coordinates in the aperture plane

$$W(u, v) = \int_{-\infty}^{+\infty} \int_{-\infty}^{+\infty} \mathcal{E}(x, y)\mathcal{E}^*(x - u, y - v) \, dxdy \tag{4.19}$$

It is a measure of the sensitivity to certain spatial frequencies (generalization of Eq. 4.17). The area in the spatial frequency domain, in which measurements can be made, i.e., where $W(u, v)$ is not zero, is generally designated as (u, v)-*coverage*.

$W(u, v)$ of an interferometer array can be compared to the effective area of a single reflector. The response of an interferometer array is given by

$$\mathcal{V}_{\text{measured}}(u, v) = W(u, v)w(u, v)\mathcal{V}(u, v) \tag{4.20}$$

with a given weighting factor $w(u, v)$ of the spatial frequencies: e.g., natural or uniform weighting (see Sect. 5.2 for more details).

Earth rotation synthesis requires joint observations of the source of all telescopes as far as possible. Complex scheduling plans need to be prepared to find the best time window in which the favoured antennas look simultaneously at the source. Every measurement of

---

[11]$W(u, v)$ refers to the spatial frequencies rather than to the radio frequencies to which the receivers responds.

a pair of telescopes with a common observation time slot, is correlated. While the Earth is turning, more (or other) telescopes will be available to see the source and thus, they can be added to the observation schedule, providing more baseline combinations. The baseline sensitivity of two different telescopes is defined (Walker, 1995) with the VLBI system efficiency factor η, the integration or fringe fitting time Δt, and the bandwidth $\Delta \nu$

$$\Delta S_{ij} = \frac{1}{\eta} \sqrt{\frac{\text{SEFD}_i \cdot \text{SEFD}_j}{2\Delta t \Delta \nu}} \qquad (4.21)$$

where SEFD stands for system equivalent flux density. The SEFD is the combined sensitivity of both, antenna and receiver (i.e., system temperature), often dominated by the effective collecting area with SEFD$\sim A^{-1}$ (Thompson et al., 2001, Sect. 1.2). The total noise limit in the final image is the combined sensitivity of all baselines integrated over the observing time. The most challenging part in scheduling a VLBI experiment is to find time windows such that the baseline sensitivity is supported at best to improve the signal-to-noise ratio (SNR). Large reflectors with a low SEFD enable good detections (high SNR) even in combination with smaller telescopes. Thus, experiment time windows are favoured where the source is in the field of view of the largest telescopes to obtain the highest image sensitivity.

Although VLBI techniques were improved during the last few decades, the greatest problem in handling VLBI imaging, are the unavoidable holes in the (u, v)-coverage due to oceans or just sparsely arranged radio telescopes. This causes incomplete sampling of the (u, v)-plane which results in an imperfect image of the flux density distribution of the sky. To compensate smaller effects, the visibility data are interpolated. Nevertheless the holes add unwanted components to the synthesized beam.

The highest possible resolutions, i.e., arrays with the longest baselines, up to now, were achieved by space-VLBI. For example the VSOP mission (Hirabayashi et al., 2000) with the HALCA satellite equipped with a $10\,\text{m}$ antenna obtained the longest baseline up to three times longer than achievable on Earth. However, the image reconstruction process is significantly complicated since the total lack of intermediate baselines and so, special care needs to be taken.

4.2 The TANAMI program

TANAMI (Tracking Active Galactic Nuclei with Austral Milliarcsecond Interferometry)[12] is a VLBI monitoring program which focuses on the parsec-scale structure of extragalactic jets south of $-30°$ declination (Mueller et al., 2009; Kadler et al., 2007; Ojha et al., 2010). The observations are made with the antennas of the Australian Long Baseline Array (LBA) and associated telescopes in the Southern Hemisphere (for details on telescopes see Fig. 4.6 and Table 4.2). The sample of currently 75 sources is monitored approximately every two months at two frequencies, $8.4\,\text{GHz}$ (X-band, $4\,\text{cm}$) and $22\,\text{GHz}$ (K-band, $13\,\text{mm}$). TANAMI is the complement to other ongoing VLBI monitoring programs in the Northern

---

[12]`http://pulsar.sternwarte.uni-erlangen.de/tanami`
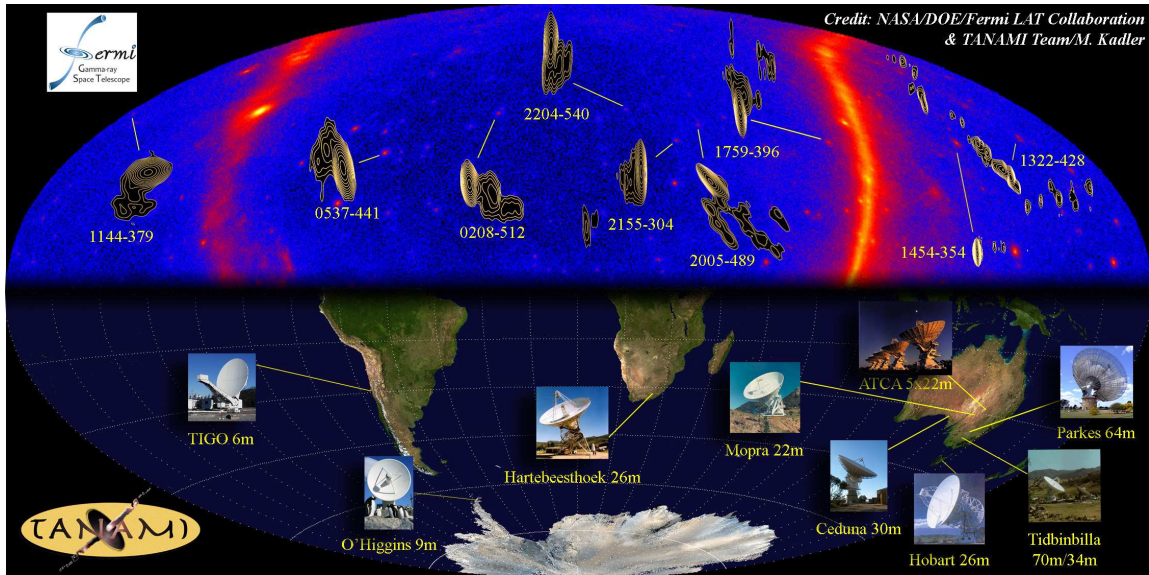
Figure 4.6: Collage of the Southern *Fermi*/LAT γ-ray sky in the top half of this Aitoff
projection (with south being up) and the Southern Hemisphere of the Earth in the bottom
with the positions of the radio telescopes of the TANAMI array indicated. Overlaid on the
Fermi sky image are TANAMI radio images of the brightest extragalactic γ-ray sources.
(Credit: NASA/Fermi-Collaboration, TANAMI-Team/M. Kadler)

Hemisphere (e.g., MOJAVE Lister et al., 2009a) and offers an invaluable data set of AGN
in the southern sky.

The initial TANAMI sample consisted of 43 blazars located south of $-30°$ declination. It
has been defined combining a radio selected flux-density limited subsample and a γ-ray se-
lected subsample of known and candidate γ-ray sources based on results of *CGRO*/EGRET
(Hartman et al., 1992). All known extragalactic radio sources south of $\delta = -30°$ from
the catalogue of Stickel et al. (1994) which are above a limiting radio flux density of
$S_{5\,GHz} > 2\,Jy$ and have a flat radio spectrum ($\alpha > -0.5$, $S \sim \nu^{+\alpha}$) between $2.7\,GHz$
and $5\,GHz$, were included. The γ-ray selected subsample includes all known γ-ray extra-
galactic jets detected by EGRET. The immediate driver for this multiwavelength project
was the launch of the γ-ray observatory *Fermi*. Since then, newly detected *Fermi*/LAT
bright sources (Abdo et al., 2010a) were added continuously to the sample. Centaurus A
is one of the two radio galaxies of the initial TANAMI sample which was detected by
Fermi/LAT within the first three months of operation (Abdo et al., 2009). It was included
to the TANAMI sample according to the flux limits but it is still one of the TANAMI
sources of particular interest due to its proximity providing an excellent view on an AGN
jet. Furthermore, TANAMI provides the first continuous monitoring of this nearby AGN
with (sub-)milliarcsecond resolution.

Besides the tight TANAMI-*Fermi*-connection, a multiwavelength approach is aspired.
Therefore, correlated observations with *Swift* (UV/optical & X-rays) and *INTEGRAL* (X-
rays) and radio flux density measurements through the GHz band with the Australian
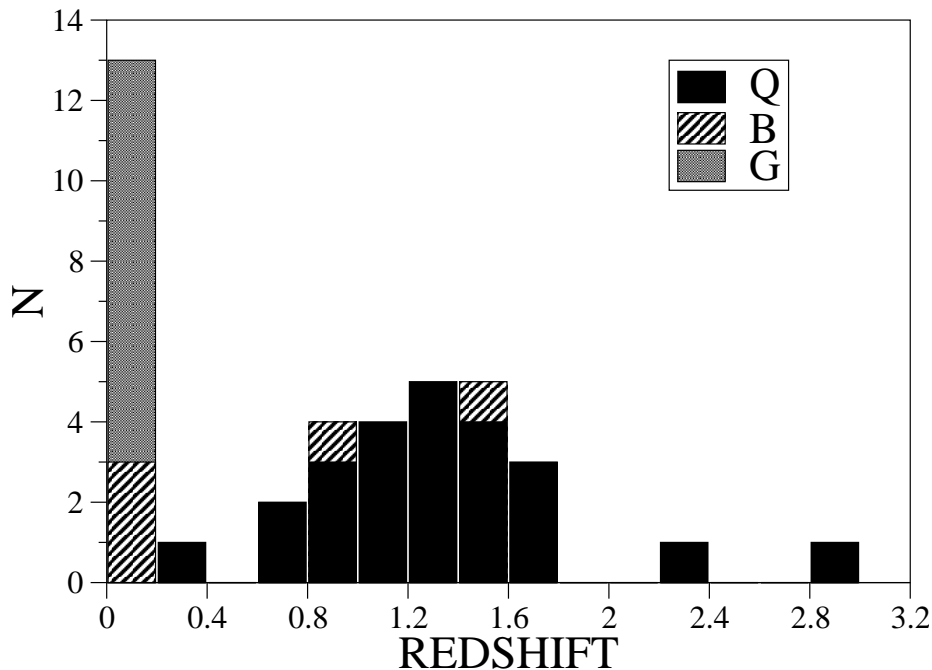
Figure 4.7: Redshift distribution of initial TANAMI sample (Ojha et al., 2010).

Compact Array (ATCA), the antennas in Ceduna, Hobart and Effelsberg complement the VLBI monitoring. Furthermore a quick follow-up of flaring sources seen with *Fermi*/LAT is provided by the use of the Ceduna-Hobart-Interferometer with a baseline of 1700 km.

The data are recorded on the LBADRs (Long Baseline Array Disk Recorders) and correlated on the DiFX software correlator at Curtin University in Perth, Western Australia (Deller et al., 2007). The correlated data are loaded into $\mathcal{AIPS}$ (National Radio Astronomy Observatory's Astronomical Image Processing System software) for data inspection, initial editing and fringe fitting. Amplitude calibration is done by using known flux values of prior observed sources.

The results of the first epoch analysis is presented by Ojha et al. (2010), while the γ-ray properties of selected TANAMI sources were analyzed by Böck et al. (2009). Worth mentioning are the results concerning opening angles of γ-ray-bright and fainter objects: excluding radio galaxies, the jet of the LAT bright TANAMI sources seem to have larger opening angles which suggests that they are pointing closer to the line of sight (see also Pushkarev et al., 2009). Hence relativistic beaming will lead to an apparent geometrical increase of the jet opening angles. The redshift distribution of the TANAMI sources (Fig. 4.7) is similar to those found by *Fermi*/LAT (Abdo et al., 2009).

The TANAMI array

In the following, the participating telescopes for the TANAMI monitoring program will be introduced. Contrary to the VLBA (Napier, 1995) in the North America, whose telescopes

Table 4.1: The TANAMI array

Telescope Name	Diameter (meters)	Location	participation at epochs[*]
Parkes	64	Parkes, New South Wales	X1, X2, X3, X4 & K3
ATCA	5x22	Narrabri, New South Wales	X1, X2, X3, X4 & K3
Mopra	22	Coonabarabran, New South Wales	X1, X2, X3, X4 & K3
Hobart	26	Mt. Pleasant, Tasmania	X1, X2, X3, X4 & K3
Ceduna	30	Ceduna, South Australia	X1, X2, X3, X4 & K3
DSS43[a]	70	Tidbinbilla, ACT	X3, X4& K3
DSS45[a]	34	Tidbinbilla, ACT	
Hartebeesthoek[c]	26	Hartebeesthoek, South Africa	X1, X2
O'Higgins[b]	9	O'Higgins, Antarctica	X3, X4
TIGO[b]	6	Concepcion, Chile	X3, X4

[*] X: 8.4 GHz, K: 22.3 GHz
[a] Operated by the Deep Space Network of the National Aeronautics and Space Administration
[b] Operated by Bundesamt für Kartographie und Geodäsie (BKG)
[c] Due to a major failure not available between Sept. 2008 and Sept. 2010

and technical equipment were designed to operate for VLBI purpose, so that all VLBA antennas are identical with the same receiving systems, the TANAMI array consists of individual telescopes in the southern hemisphere, with different sizes, receiving devices, main applications etc.. Nevertheless it is possible to put such different antennas together to form a VLBI array, even if there are several special properties which have to be understood and considered.

The participating telescopes for the TANAMI project are shown in Fig. 4.6 and the main properties are summarized in Table 4.2. For the Cen A observations analyzed in this diploma thesis, a variable subset of these antennas was used. The Long Baseline Array (LBA)[13] in Australia constitutes the heart of the array, providing smaller baselines and great sensitivity due to comparably large reflectors (e.g., Parkes). Within Australia the individual radio antennas were constructed for various purposes. For example, the Parkes radio telescope was used, among other things, to receive signals from the Apollo 11 moon landing in July 20, 1969. Moreover, the ATCA array is itself a small interferometer of six identical antennas, where five are moveable, and operating at seven frequency bands. Since the LBA was not build to form a VLBI array, the placements of most of the antennas is not optimized for VLBI purpose (see Fig. 4.6) since most of them are located in the south-eastern part of Australia. This leads to several similar projected baselines during a scan and hence no big variety of spatial frequencies. To compensate this and to add longer baselines, the South African antenna at Hartebeesthoek is participating in VLBI observations together with the LBA now for several decades (e.g., SHEVE program SHEVE Team, 1994). Furthermore the TANAMI team was able to bring two additional transoceanic antennas into the observation schedule: the Transportable Integrated Geodetic Observatory (TIGO) in Chile and the German Antarctic Receiving Station (GARS) at O'Higgins (Antarctica). As it will be shown in Chap. 5, these telescopes improve the

---

[13] http://www.atnf.csiro.au
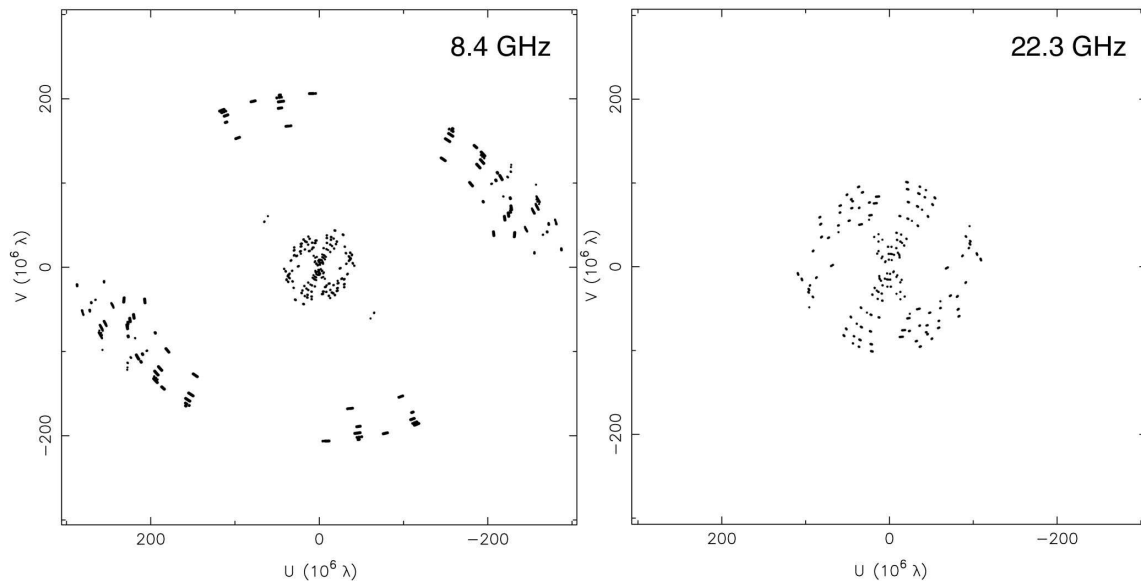
Figure 4.8: (u, v)-coverage for Cen A of November 2008 observations for 8.4 GHz (left) and 22.3 GHz (right)

(u, v)-coverage for the Cen A observations[14] significantly. The situation for the November 2008 observations at both frequencies is shown in Fig. 4.8. At 8.4 GHz the high spatial frequencies at $\sim$200 Mλ are due to these transoceanic telescopes. Observations at baselines spanned between these smaller antennas and e.g., Parkes, will achieve comparable sensitivity. With this array configuration of November 2008, TANAMI achieved the one of the highest angular resolution images for Centaurus A in both bands. This is comparable to former space-VLBI observations by Horiuchi et al. (2006). Due to the proximity of Cen A, this provides the highest linear resolution image of the sub-parsec scale center of an AGN (see Chapt. 5).

4.3 VLBI data reduction

Before actual data analysis of the brightness distribution of a source (imaging) can be performed, a complex data reduction and calibration process has to precede. The following section describes the methods which have to be applied to perform the analysis presented in Chapt. 5. The *a-priori* calibration and data inspection is done in $\mathcal{AIPS}$ (Astronomical Image Processing System; Fomalont, 1981; Greisen, 1998). Afterwards the processed data are loaded into DIFMAP (Shepherd, 1997) for final imaging and self-calibration.

---

[14]TIGO and O'Higgins are not able to operate at 22.3 GHz. Thus the improvement affects only the 8.4 GHz TANAMI observations. Contrary to more general and common radio observations, the angular resolution does not increase with frequency according to Eq. 4.1, but inversely.

4.3.1 Calibration

The data from the correlator are read from the discs and are loaded into $\mathcal{AIPS}$ for first inspection and selection, i.e., bad data (with low SN ratio or due to recording malfunction) are flagged. The following short explanations on the *a-priori* calibration steps is mainly adopted from Diamond (1995). After this pre-calibration data process, the data are calibrated. In $\mathcal{AIPS}$ there is no modification of the original data but all conversion factors of all calibration steps, all flagging information and all baseline corrections are stored in separate files. These can be loaded together with the original visibility data and subsequently examined or manipulated.

The first step is the *a-priori* amplitude calibration to account for instrumental or atmospheric opacity effects. This process estimates the parameters of the transfer functions which define the relationship between observed raw data (output) and true input data. With the help of flux calibrators, the system temperatures and corresponding sensitivities and on-source noise (depending on the elevation) of each telescope is known (see Eq. 4.21). Hence, applying the transfer function, the true observed visibilities can be reconstructed.

The second step is then the *a-priori* phase calibration. Since visibility phases reflect the source positions and extended structure, special effort must be made to correct for delays. Furthermore, the visibility phases need to be almost constant to integrate visibilities coherently. Due to offsets within the different IF channels, appropriate corrections have to be applied (single band instrumental phase and delay correction). After this correction of the visibility for instrumental effects, some phase errors from atmospheric or geometrical effects still remain. This can be compensated via fringe fitting (multiband residual phase and delay correction) to allow the user to average the data in time.

When satisfied with the calibration and editing, these tables are used to create single *uv*-files in FITS format (Flexible Image Transport System, Wells et al., 1981), containing the corrected data for each source. These files are then exported and read into the interactively editing and hybrid mapping program `DIFMAP` (Shepherd, 1997).

4.3.2 Total intensity mapping

According to Eq. 4.18 and Eq. 4.20 the imaging process withtin `DIFMAP` consists of two major steps: 1.) discrete Fourier transformation of the visibility and 2.) deconvolution of the true intensity distribution $I(l,m)$ and the synthesized beam $b_0(l,m)$, which is the Fourier transform of the weighted transfer function (4.19) depending on the (u,v)-coverage:

$$I_{\mathrm{measured}}(l,m) = I(l,m) ** b_0(l,m) \tag{4.22}$$

where the double asterisk symbol indicates the 2D-convolution. In practice it is impossible to solve for $I(l,m)$ analytically, because the unmeasured visibilities provide a fundamental problem when trying to apply the convolution theorem (Eq. 4.15). To avoid this, the imaging procedure has to interpolate between measured visibilities by taking values consistent with most reasonable intensity distribution. The `clean`-algorithm was implemented in the hybrid mapping program `DIFMAP` to perform this deconvolution numerically (Högbom,

1974). In principle, `clean` constructs a model for the true visibility function $\mathcal{V}(u, v)$ to solve the Fourier transform of Eq. 4.22.

At first, averaging of the (u, v)-data over time is recommended by specifying the time bin (in seconds) to correct for the error overestimation done by $\mathcal{AIPS}$. To get an overview of the observation parameters, the on-source time of each antenna during the scan and the resulting (u, v)-coverage can be displayed and expected. Due to incomplete sampling of the (u, v)-plane, the discrete Fourier transform has to be applied to get the brightness distribution. This results in the "dirty map" which is the convolution of the "true" brightness distribution and the so called "dirty beam". The dirty beam is the reception pattern of the whole interferometer array, the synthesized beam $b_0(l, m)$. It is called "dirty" because of being composed of a central peak with a two-dimensional FWHM defined by (u_{max}, v_{max}) and the disruptive sidelobes (weaker local maxima) mainly originating from the holes in the (u, v)-plane. To get rid of spurious effects, the `clean`-algorithm combines the deconvolution of the dirty image and the dirty beam with "smoothing" of the reception pattern. The deconvolution process to produce the "clean map" is operating in the following way (see also Cornwell et al., 1999):

1. The `clean`-algorithm works with the general assumption that the image of the source is build up out of point sources. Therefore the initial model is the brightness distribution of a point source convolved with the dirty beam.

2. These point-source model components are subtracted at the position of maximal brightness in the dirty map and stored temporarily.

3. To predetermine the part of the dirty map where the `clean`-algorithm should be applied, rectangular "clean windows" are placed to mark the position of the brightest residual.

4. Each `clean`-iteration should be followed by a phase self-calibration step on this latest model to correct for changes (originating from `clean`-substraction) concerning the closure phases.

5. After several of these steps, the model consists out of a number of point source components at a certain position with a certain flux density value. The subtractive `clean`ing-process is continued until the remaining flux density of the dirty map is on noise level without any more features. The dirty map remains as "residual map".

6. Out of all "clean components" (i.e., single point source model components) the "clean map" is established by convolving the point source components with the "clean beam" to remove the danger of over-interpretation. The clean beam is a Gaussian approximation to the FWHM of the dirty beam (given by (u_{max}, v_{max})), thus the unsightly sidelobe effects are removed.

7. At last the residual map is added to the clean map, resulting in the final map representing the true $I(l, m)$.

It is worth noting, that the `clean`-algorithm is constructing a model consisting only of point source responses while the model is fitted to the visibility data.

To improve the image quality, several calibration and data examination steps have to be performed besides the `clean`ing. Even after the *a-priori* calibration in $\mathcal{AIPS}$, visibility

phases and amplitudes can still suffer from errors. After building up an initial model, the visibility data should be examined and corrupt data should be flagged. Subsequently an amplitude self-calibration should be applied to determine the overall telescope amplitude corrections. After building up a reasonable model, i.e., when the iteration process has converged, a combined phase and amplitude self-calibration should be performed. When the residual map consists only of evenly distributed emission of $\leq 1\,\mathrm{mJy}$, the imaging process is finished. This ends up with a very complex model of several hundred `clean` components which are necessary to reasonable deconvolve the dirty beam. The final resolution of a VLBI image is determined by mainly the (u, v)-coverage but also by the performance of data recording, fringe fitting and careful mapping. The latter is strongly dependent on the placement of the `clean`-windows. A badly fitting model to visibilities of outer baselines can cause a loss of these data points during calibration steps and, consequently, the final map will suffer from that. Moreover, since the self-calibration process is based on the applied model, good results are only achieved with high preciseness.

5 TANAMI observations of Centaurus A

THIS diploma thesis addresses the first 8.4 GHz and 22.3 GHz VLBI observations of Centaurus A made in the framework of the TANAMI program with the aim to investigate the spectral and kinematical behaviour of the sub-parsec scale radio jet and counterjet. At 8.4 GHz, Cen A was observed in November 2007 (1$^{\text{st}}$ epoch), June 2008 (2$^{\text{nd}}$ epoch), November 2008 (3$^{\text{rd}}$ epoch), separated by $\sim$0.5 yr each, and in September 2009 (4$^{\text{th}}$ epoch). The 22.3 GHz observation took place simultaneously to the 3$^{\text{rd}}$ 8.4 GHz observation in November 2008. These TANAMI observations result in a spectral-index map of Cen A and jet speed determination at a spatial resolution of lightdays.

In this chapter, the analysis of these five VLBI data sets will be discussed. To begin with, Centaurus A will be introduced by focussing on the main properties of this radio galaxy and results of previous multiwavelength observations. Thereafter, the results and challenges of the total intensity mapping with the hybrid imaging method provided by DIFMAP (see Sect. 4.3.2) will be presented. Secondly, besides the complex point source model for best possible deconvolution, a more simple model of components with Gaussian emission profiles was fitted to the visibility data in order to identify the positions of the main emission features of the jet. Based on these resulting models the jet kinematics and spectral index distribution of the innermost Cen A jet-counterjet system will be investigated.

5.1 Centaurus A - The main character of this thesis

Centaurus A, also known as PKS 1322−428, NGC 5128, is one of the most prominent multiwavelength sources and, moreover, one of the most studied extragalactic objects at all (e.g., Malin et al., 1983; Tingay et al., 1998; Steinle et al., 1999; Abdo et al., 2010c). The radio source Cen A is by far the closest AGN classified as a prototype radio galaxy of Fanaroff-Riley type I. It is radiating light over the whole frequency range from γ-ray to radio, showing emission from stars, neutral, molecular and ionised gas, from the accretion disk around th central SMBH and from powerful radio jets. Therefore, only multiwavelength observations can reveal Cen A's peculiar appearance exhibiting emission features from sizes of lightdays to kiloparsec scales. The angular extent of the giant double radio lobes is $\sim$10° compared to the diameter of $\sim$20′ of the host galaxy NGC 5128. In the radio all-sky image (Fig. 1.1) Cen A is clearly visible at galactic coordinates $l \approx 309.5°$ and $b \approx 19.4°$.
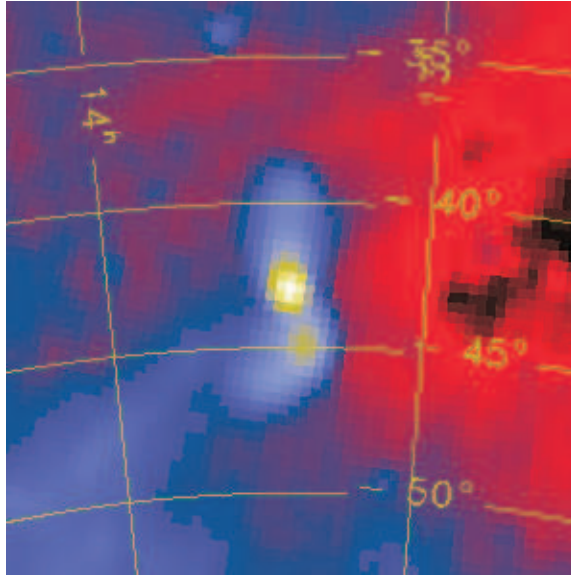
Figure 5.1: This close-up of 408 MHz all-sky-survey shows the prominent giant lobes of
   Cen A spreading over ∼ 10° in the sky (Haslam et al., 1982).

Figure 5.1 shows a close-up of the 408 MHz survey (Haslam et al., 1982) displaying the
enormous radio source, 20 times larger than the projected size of the full moon. Due to its
proximity it is not just one of the most spectacular objects in the sky but also an excellent
laboratory to study AGN physics. Within the last ∼170 years of observations, astronomers
uncovered more and more the nature of Cen A's various appearances, but the complexity
of the physical processes to form and power its components are not yet understood in
detail. High resolution images and spectroscopic measurements provide further details and
deeper insights for inspecting this special active galaxy in particular and AGN properties in
general. In the following section, the main characteristics of Cen A and results of previous
observations will be presented by focussing on the multiwavelength investigations.

5.1.1 Discovery and history

What we know today as an active galaxy with the elliptical host galaxy NGC 5128, named
after its radio properties 'Centaurus A', was first discovered in the optical by James Dun-
lop in 1826 as singular double nebula in the constellation Centaurus (Dunlop, 1828). He
already mentioned the peculiar shape of apparent two distinct emission zones, which were
later explained by a edge-on dust lane crossing the optical visible galaxy. Despite obser-
vations by J. Herschel, the nebula NGC 5128 was not in the focus of astronomical interest
over about 100 years. Due to the lack of large optical telescopes in the southern hemisphere,
Cen A was considered to be just one more of these diffuse objects which were meanwhile
identified as discrete galaxies. Bolton et al. (1949) conducted the first radio observations
of Cen A. The authors were the first to identify NGC 5128 with the radio source Cen A,
denoting it as a radio galaxy. This was the first association of a radio source with an extra-
galactic object. The first explanation for the special appearance of Cen A was proposed by
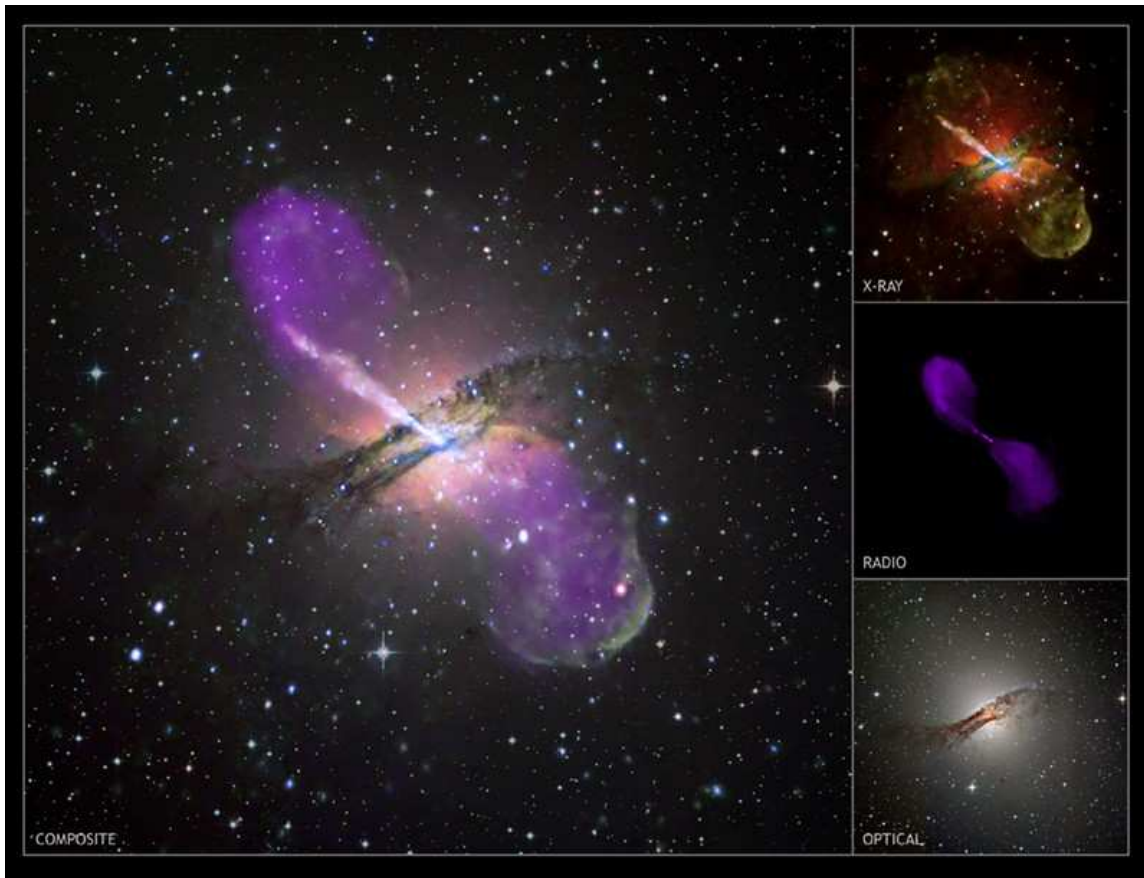
Figure 5.2: Multiwavelength composite of the inner region of Cen A (within $\sim 15'$, cf. also Fig. 5.3) at radio (VLA), X-ray (*Chandra*) and optical (VLT, ESO) (Credit: NASA/CXC/Kraft et al., NSF/VLA/Hardcastle et al., ESO/VLT/ISAAC/Rejkuba et al.)

Baade & Minkowski (1954): the structure is formed due to a merger of two galaxies. This is still today the most reasonable assumption to explain the AGN activity. With the evolution of radio astronomy, improved techniques made it possible to investigate the radio emission extensions and variability (e.g., Bolton & Clark, 1960). Further measurements detected, besides the radio activity, also X-rays (Bowyer et al., 1970), IR emission (Kunkel & Bradt, 1971) and γ-rays (Grindlay et al., 1975).

5.1.2 Multifrequency look from kilo- to sub-parsec scales

In the center of the giant elliptical galaxy NGC 5128 a supermassive black hole with a mass of $M_{\mathrm{SMBH}} = 5.5 \pm 3.0 \times 10^7 \, M_\odot$ (Cappellari et al., 2009) is the engine for the AGN activity. It has a distance of 3.8 ± 0.1 Mpc (Harris et al., 2009) where an angular resolution of 1 milliarcsecond (mas) corresponds to ~ 0.018 pc. It stands in the southern sky at $\alpha = 13\,\mathrm{h}\,25\,\mathrm{min}\,27.6\,\mathrm{s}$, $\delta = -43\,\mathrm{h}\,01\,\mathrm{min}\,09\,\mathrm{s}$ (J2000, Ma et al., 1998). For an overview over the
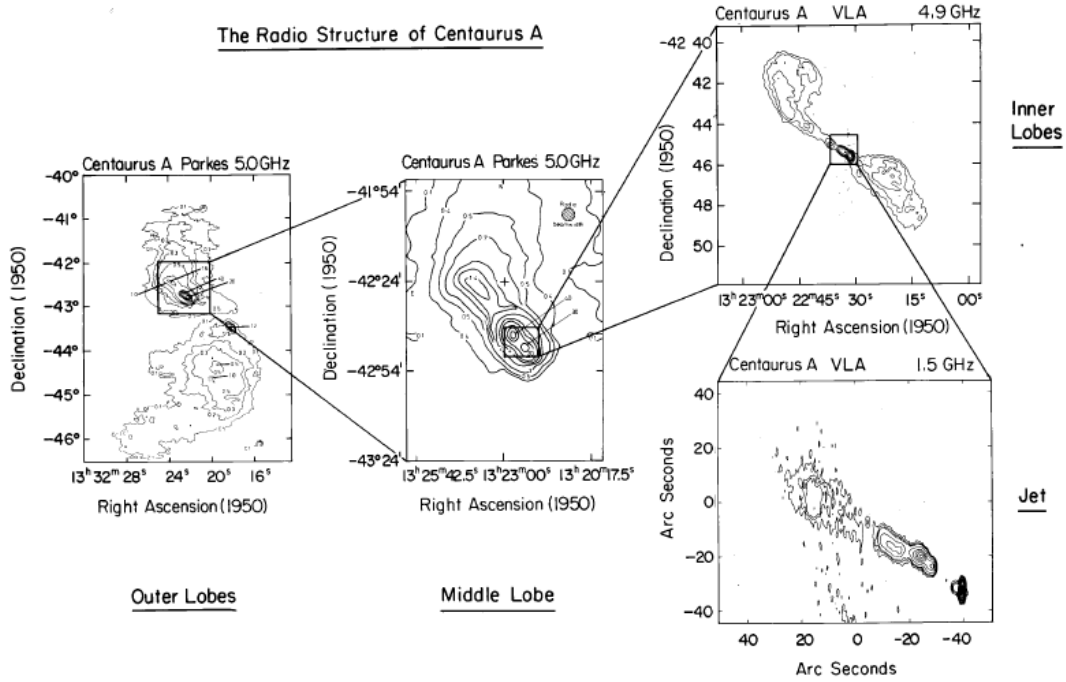
Figure 5.3: Radio maps of the Cen A jets on pc scales to the giant outer lobes extending to 250 kpc (Burns et al., 1983; Israel, 1998).

different visual appearances depending on the observing frequency, in the following a tour through the whole range of Cen A's spectrum will be given (cf. also Israel, 1998; Steinle, 2006).

Figure 5.2 summarizes for the most part the multiwavelength characteristics exhibited by Cen A. It can be clearly seen that the difference in morphology is strongly varying with the observing frequency but certain structures recur at different wavebands.

In the radio band, Cen A exhibits the most extended and impressive structures. An overview is given in Fig. 5.3. It is classified as a FR I type because of the high core brightness compared to the lobes. Due to its proximity and the capability of radio telescopes and interferometers, these features can be imaged in rich detail at high angular resolution. The radio emission is coming from the core and the double-sided radio jets which can be detected from sub-parsec scales up to several kilo-parsec. The whole radio source is known as 'Cen A'. Distinguished measurements led to a complex jet structure: in the very central region of Cen A (angular expansion of a few milliarcseconds, 'VLBI-scale') strongly collimated radio jets with a position angle to the line of sight of P.A. $\sim 50° - 80°$ were detected with VLBI methods (Tingay et al., 1998, 2001; Horiuchi et al., 2006). The jet is clearly detectable whereas the emission of the counterjet is diminished due to relativistic beaming effects. Jones et al. (1996) first detected the sub-parsec scale counterjet. Subluminal motion of $v_{\mathrm{app}} = 0.1 - 0.7c$ is observed (Tingay et al., 1998, 2001). These inner jets continue within arcminutes and end in the inner radio lobes with an extent of $\sim 12'$. In Fig. 5.2 the radio part is showing these inner features. The jet inclination angle to the line of sight is not
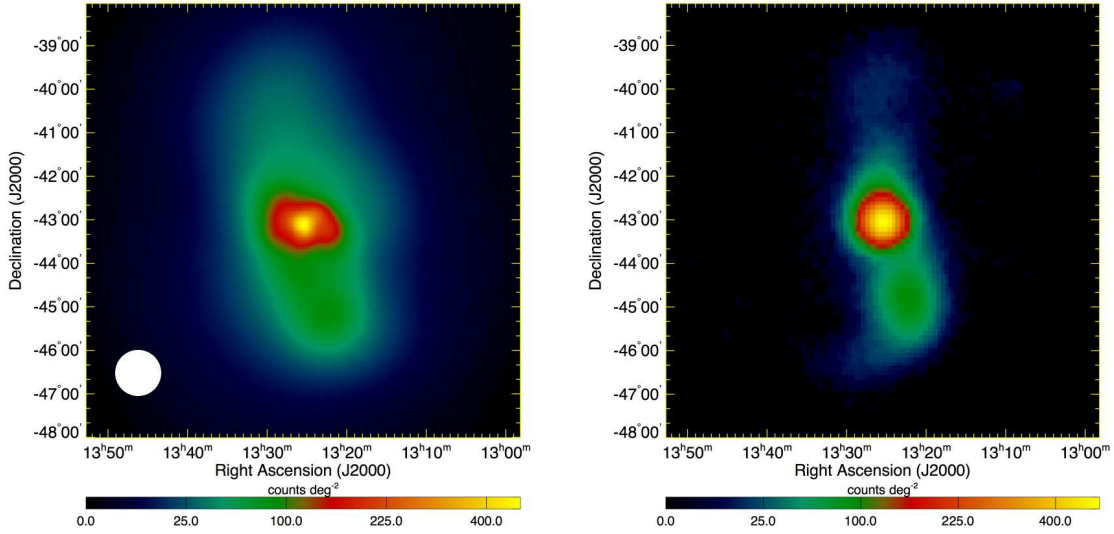
Figure 5.4: Comparison of the Cen A images made by *Fermi*/LAT (right) and by 22 GHz WMAP (left) (Abdo et al., 2010b; Hinshaw et al., 2009) at similar angular resolution, showing firstly the significant core emission and secondly, an excess of emission in the southern giant radio lobe (with the lobe flux densities lower than the emission from the core). The white circle in the LAT image refers to the point-spread-function of the LAT instrument.

constant but thought to be tilted in a different way at larger scales (Hardcastle et al., 2003). In the northern part, a bright extended structure can be seen which as no counterpart in the south, often referred to as the middle lobe. The outer northern and southern giant lobes (Fig. 5.1) spread over $\sim 5° \times 10°$ at the sky. The inner arcminute scale lobes are misaligned to the outer giant ones by $\sim 45°$ (Burns et al., 1983). In general, it is believed that the northern part is tilted towards the observer.

Infrared observations conducted with the *Spitzer* space telescope by Quillen et al. (2006) revealed a dusty wrapped disk with a parallelogram shape around the center. The disk with a radius of $r \sim 100''$ is seen almost edge-on, lying parallel to the dust lane in the galaxy equator. This dusty disk is also an indicator for a recent merger event $\sim 10^7$ years ago (Baade & Minkowski, 1954; Block & Sauvage, 2000; Quillen et al., 2006).

The optical appearance is dominated by the elliptical (S0) galaxy NGC 5128 which has an optically-dark band of absorbing dust projected across its body (see Fig. 5.2) and parallel to the semimajor axis. Hence, the optical view on the nucleus is blocked by this torus (Israel, 1998). NGC 5128 is the stellar body of the radio source. The respective alignment of the dust line and the radio lobes is almost perpendicular to each other. In the optical, it is seen as a Seyfert 2 object (Dermer & Gehrels, 1995).

In the soft ($\sim 0.1-10$ keV) and hard ($\sim 10-100$ keV) X-ray band, Cen A was monitored with balloon, rocket and satellite experiments (for a review see, e.g., Steinle, 2010). It

showed a variability of the order of one magnitude (Bond et al., 1996). The X-ray spectrum ($2\,\text{keV}-2.3\,\text{MeV}$) can be described by a powerlaw with a spectral index of $\alpha \sim -1.8$ (Baity et al., 1981). With *Chandra* (Kraft et al., 2002) high resolution X-ray images of the inner Cen A region reveal a (northern) kiloparsec scale X-ray jet (see Fig. 5.2). Within the jet, several X-ray knots can be detected which can partially be matched with radio knots (Hardcastle et al., 2003) showing a subluminal motion of $\sim 0.5c$. Rothschild et al. (2006) and Benlloch et al. (2001) found a varying column density N_{H}, which could be due to an absorbing disk seen edge-on which shields only a part of the X-ray emission. Moreover, measurements of the Fe Kα line gives information about the origin of X-ray emission. *RXTE* observations over a time period of 12 years led us to the conclusion that the nucleus of Cen A is seen through a clumpy molecular torus (Rothschild et al., 2010).

At higher energies ($\sim 100\,\text{keV}$ to $300\,\text{GeV}$), the γ-ray Large Area Telescope (LAT) on board of the *Fermi* satellite (Abdo et al., 2009) recently confirmed the former *EGRET*/CGRO detection (Hartman et al., 1999). Due to higher sensitivity and resolution, *Fermi*/LAT enabled to separate the γ-ray emission into two discrete bright regions: the galaxy nucleus (Abdo et al., 2010c) and the giant radio lobes (Abdo et al., 2010b). In Fig. 5.4 this connection is clearly visible from a by-eye-inspection, the southern giant lobe exhibits significant emission besides the bright AGN core. It is worth noting that in contrast to the emission of the inner lobes, the southern giant radio/γ-ray lobe is more powerful. The high energy spectrum of the whole extended object is soft with the photon index $\Gamma \sim 2.52$ (north) and $\Gamma \sim 2.6$ (south) (Abdo et al., 2010b)[1]. Abdo et al. (2010b) presented broad band emission for both lobes separately, explaining the high energy component in the spectral energy distribution with inverse Compton scattering.

In the TeV-range, the Cherenkov telescopes of the H.E.S.S. experiment detected a faint very high energy (VHE) γ-ray emission of Cen A (Aharonian et al., 2009), revealing a possible site for cosmic particle acceleration. Cen A is considered as a candidate for ultra high energy cosmic-ray (UHECR) emission, since a close connection between highest-energy cosmic rays and powerful extragalactic objects is suggested (Abraham et al., 2007). Ongoing experiments try to test and prove the individual emission-mechanism models for cosmic particle accelerators. Due to the GZK-effect[2] nearby AGN, like M87 or Cen A, are expected to be UHECR emittors. Hence, Cen A became one of the most important targets of high energy astroparticle physics for distinguishing the origin of cosmic rays (Abraham et al., 2009; Clay et al., 2010). Beaming effects in blazar jets, spine-sheath models involving Compton scattering of high energetic particles, or acceleration in the vicinity of the SMBH are potential UHECR production mechanism which are currently discussed (see, e.g., Abdo et al., 2010c; Aharonian et al., 2009). Moreover, Cen A is suspected to be also a high energy neutrino emitter, since the Pierre Auger Observatory reported on a possible detection (e.g., Cuoco & Hannestad, 2008; Kachelrieß et al., 2009).

Figure 5.5 summarizes this multiwavelength view of Cen A's core region. The spectrum is constructed out of simultaneous data to *Fermi*/LAT observations and of historical data (e.g., H.E.S.S. measurements). The double humped shape of a typical blazar SED is seen,

---

[1]cf. $\alpha_{\mathrm{radio}} \sim 0.7$, see Alvarez et al. (2000)

[2]The Greisen-Zatsepin-Kuzmin effect sets an upper limit to a distance of $\sim 50\,\text{Mpc}$ for a possible high energy emission coming from extragalactic objects (Greisen, 1966).
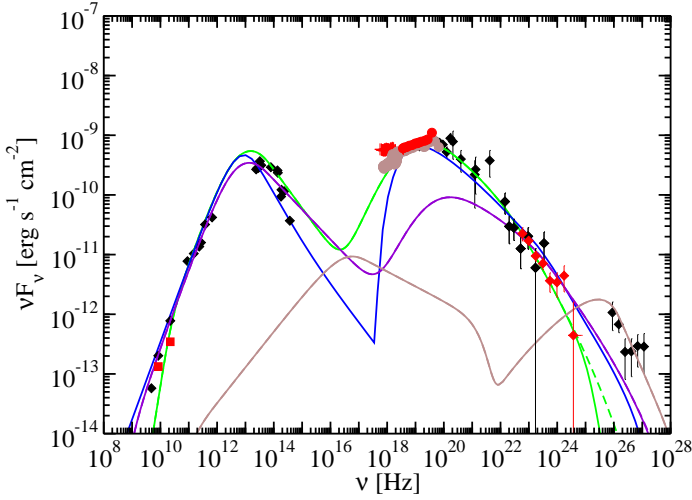
Figure 5.5: Spectral energy distribution of Cen A's core emission by Abdo et al. (2010c) with dual-frequency TANAMI data simultaneous to *Fermi*/LAT observations of November 2008.

indicating synchrotron self compton processes (for more details, see Abdo et al., 2010c, and Sect. 3.3).

5.1.3 Why is Cen A so special and interesting?

As Cen A is the closest AGN in our cosmic neighbourhood, high resolution observations of it can provide the best insights into AGN activity, emission mechanism, and the interaction with the intergalactic medium. The monitoring of Cen A aims for information about AGN in general. Due to its peculiar appearance in the radio band, there is a particular interest to study the radio jet in detail. Spectral and dynamical measurements help to understand the complexity of jet formation, propagation and emission. Furthermore, these mechanisms are linked to the behaviour of the accretion and energy release. The combination of multiwavelength and high resolution observations has shown a close connection between different spectral ranges. In particular, a correlated variability in the radio band and the γ-ray regime is noticed, suggesting a relation of matter ejection ('jet blobs') and high energy flaring (e.g., Sokolovsky et al., 2010; Tavecchio et al., 2010; Jorstad et al., 2001a). In this diploma thesis, radio observations of the central region of Cen A at spatial resolutions of $\leq 0.2\,\mathrm{pc}$ are discussed giving the highest resolved view onto an AGN ever. In order to constrain the production origin of high energetic photons, well resolved images of the possible emitting AGN components are required.

Cen A's peculiarity arises from its proximity and the resulting possibility to study an AGN in great detail. The various connections between AGN activity and other astronomical processes, e.g., star formation or galaxy evolution, make multiwavelength observations of this source crucial in order to apprehend the underlying physics (cf. Chapt. 2). The radio source Cen A offers a great opportunity to test theoretical models for extragalactic jet dynamics and emission. Since these powerful sources illuminate the early universe and shed light on the evolution of galaxies, it is necessary to understand their behaviour in general and thus, observations of Cen A play an decisive role.

5.2 Imaging of VLBI data

The visibility data of the four 8 GHz and the one 22 GHz epoch were imaged using the hybrid mapping method provided by the program `DIFMAP`, described in Sect. 4.3.2. For each epoch, two different weightings of the visibility data (Eq. 4.20), natural and uniform, were applied.

At natural weighting (or equal weighting), every spatial frequency data point is weighted depending on the corresponding sampling density or, in other words, well sampled regions of the (u, v)-plane get a higher weight than sparsely sampled ones. This leads to the best sensitivity and image fidelity, since the data are not over-interpreted but considered according to the particular array parameters. Although intermediate-length baselines are absent in these TANAMI observations, limiting the overall image quality, this constraint does not preclude good images as long as special care is taken in calibration and the imaging process. In the case of the TANAMI array, shorter baselines have a higher contribution to the sampling, hence the (u, v)-coverage is better for baselines with $b \leq 100\,\mathrm{M}\lambda$ (see, e.g., Fig. 4.8).

Contrary to this, at uniform weighting the same weight is given to every baseline, achieving the highest resolution, as low sampled spatial frequencies have equal weight to densely sampled (u, v)-regions. Here the data are weighted inversely to the number of visibilities within one bin with a binning size of 2 pixels in the (u, v)-plane. Obviously, uniform weighting is more sensitive to small-scale structures in the central part of the image because of setting higher priority to (generally) less sampled long baselines. It is the best way to investigate the smallest resolvable features within the jet. However, one looses the image fidelity with respect to natural weighting, since the robust and trustworthy spatial frequencies of the shorter baselines are downweighted. Moreover, in the case of the TANAMI array, the sensitivity is decreased due to giving lower weight to the baselines between larger antennas which are all located in South-East Australia. By comparing both, the naturally and uniformly weighted maps, the best information pool about the overall jet structure is gained. It provides a look onto the innermost jet regions at the highest possible resolution. Accordingly, the discussion of the uniform weighted images will rely on the analysis of the natural weighted images.

By applying Gaussian taper functions to reduce the contribution of longer baselines and to reduce sidelobes, it is possible to inspect extended structures or the overall jet appearance more easily. This method was used during the imaging process in order to detect weaker outer jet features.

The following consideration of the total intensity imaging of the inner Cen A radio jet regards first the higher resolved data sets at 8 GHz (cf. Sect. 4.2). The first 22 GHz epoch of November 2008 will be discussed by attaching great importance to the simultaneity to the 3$^{\mathrm{rd}}$ 8 GHz epoch and resulting consequences.

The 8 GHz epoch image of November 2007 is published by (Ojha et al., 2010) as part of the initial TANAMI sample. An overview of the first three 8 GHz observations and the dual-frequency epoch of November 2008 is given by Müller et al. (2010). A refereed publication is in preparation.

5.2.1 Total intensity images

Within the monitoring of the TANAMI sample (see Sect. 4.2), the core region of Centaurus A was observed five times at 8.4 GHz and two times at 22.3 GHz between November 2007 and August 2010. Due to the time-consuming correlation and calibration process, only the epochs until the end of September 2009 were analyzed for this diploma thesis. The time span between these observations was defined mainly[3] based on the jet speed analysis by Tingay et al. (1998). The first three 8 GHz observations were chosen to be separated by ~ 0.5 years each according to $v_{app} \approx 0.1c \, \hat{=} \, 2 \, \mathrm{mas\,yr^{-1}}$. The next monitoring epoch including Cen A took place in September 2009.

The VLBI data sets were calibrated in $\mathcal{AIPS}$ and afterwards loaded into DIFMAP for preparation of the total intensity maps. The applied clean process for deconvolution of the dirty beam is explained in detail in Sect. 4.3.2. This cleaning and self-calibration process was used to produce naturally weighted images of the total intensity distribution of the Cen A jet on scales of milliarcseconds. The resulting clean images or total intensity maps of the 8 GHz epochs are presented in Figures 5.6 to 5.8. The simultaneous 22 GHz image of November 2008 is shown in Fig. 5.13. The lowest contours in all of these images represent the flux density values at $3\sigma = 3 \times \mathrm{RMS}$. The root mean squared (RMS) values are determined in a region of the final map without significant source flux. An overview of all image and observation parameters is given in Table 5.1.

The different angular resolutions (FWHM of clean beams) of these maps originate from the different array configurations (Table 4.2) and from the data quality depending on the corresponding telescope behaviour (e.g., atmospheric effects, recording, etc.) and sensitivity. For the first two 8 GHz epochs (November 2007 and June 2008) all LBA antennas and the transoceanic antenna at Hartebeesthoek were contributing. Due to a malfunction of the Parkes antenna during the measurements of the 2$^{\mathrm{nd}}$ epoch, the resulting synthesized beam got less sensitive and the angular resolution decreased (Eq. 4.21). Nevertheless, a careful calibration process achieved suitable imaging results. For the 8 GHz November 2008 observation the two transoceanic antennas TIGO and O'Higgins replaced Hartebeesthoek, which was temporarily inaccessible because of a major failure. The resulting (u, v)-coverage (Fig. 4.8) led to a great improvement in resolution. At higher frequency (22.3 GHz) the transoceanic antennas were absent because they do not provide observations at 22 GHz, but due to good (u, v)-sampling the resolution of the resulting map still exceeds the one of former measurements (Tingay & Murphy, 2001; Tingay et al., 2001).

To get into more detail of the actual imaging process of these Cen A data, the analysis of the 3$^{\mathrm{rd}}$ 8 GHz epoch will be highlighted. Later, it will be focused on the methods and the special care used for the successful data reconstruction of the 2$^{\mathrm{nd}}$ epoch.

As the steps for the imaging process are already explained above, I will concentrate now on the essential data inspection and checks during the cleaning-process for producing high quality VLBI intensity maps. The November 2008 data are characterized by the remarkably

---

[3]There are several other constraints on the observation scheduling to find a certain balance and preference of particular sources, e.g., the distribution on the sky of the monitored subsample of one epoch (for more details, see Ojha et al., 2010).
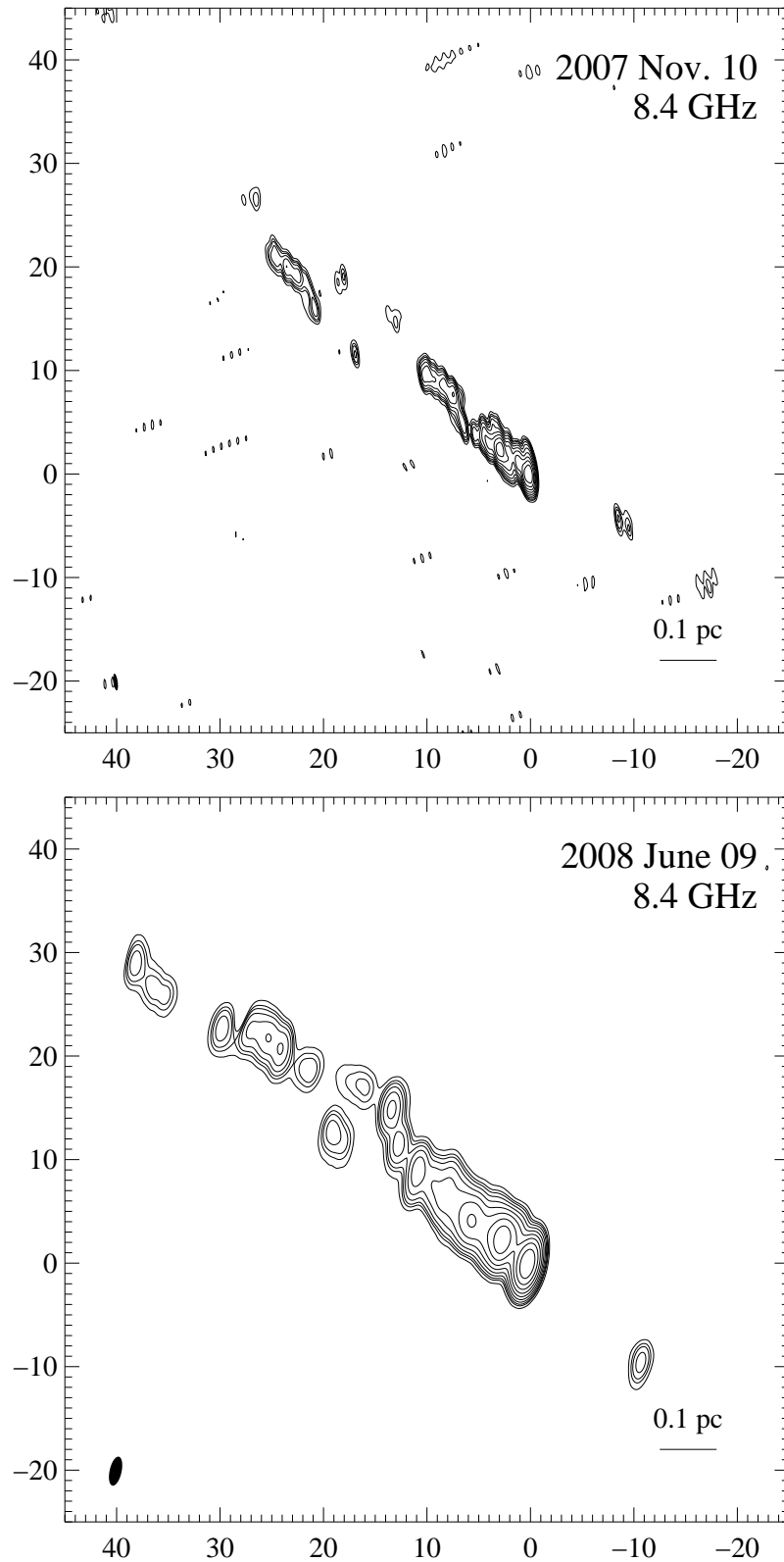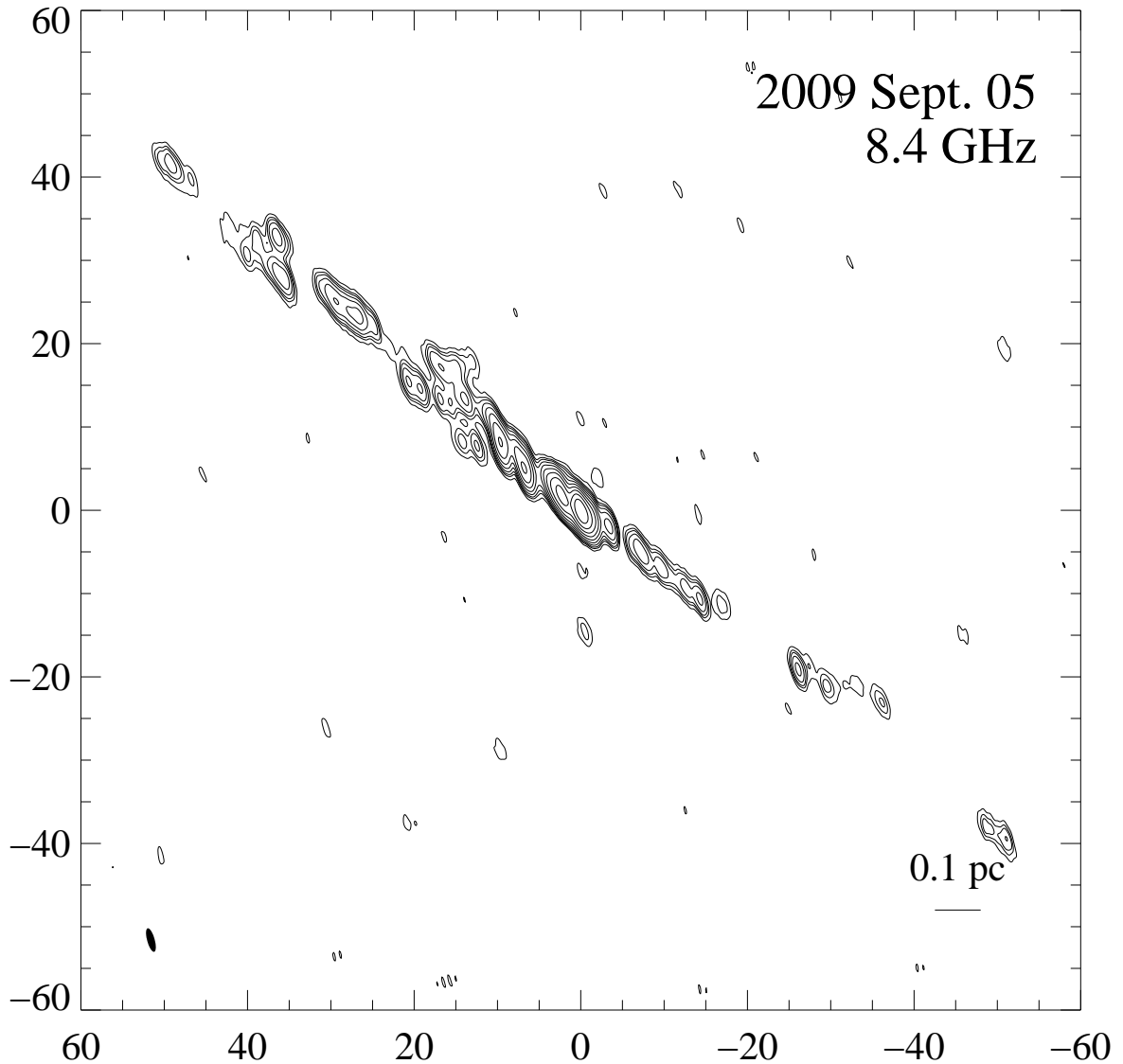
Figure 5.6: 8.4 GHz image of Cen A in November 2007 (top) and June 2008 (bottom) with natural weighting. The lowest contours denote the 3σ-level (see Table 5.1). The axes are in units of mas.
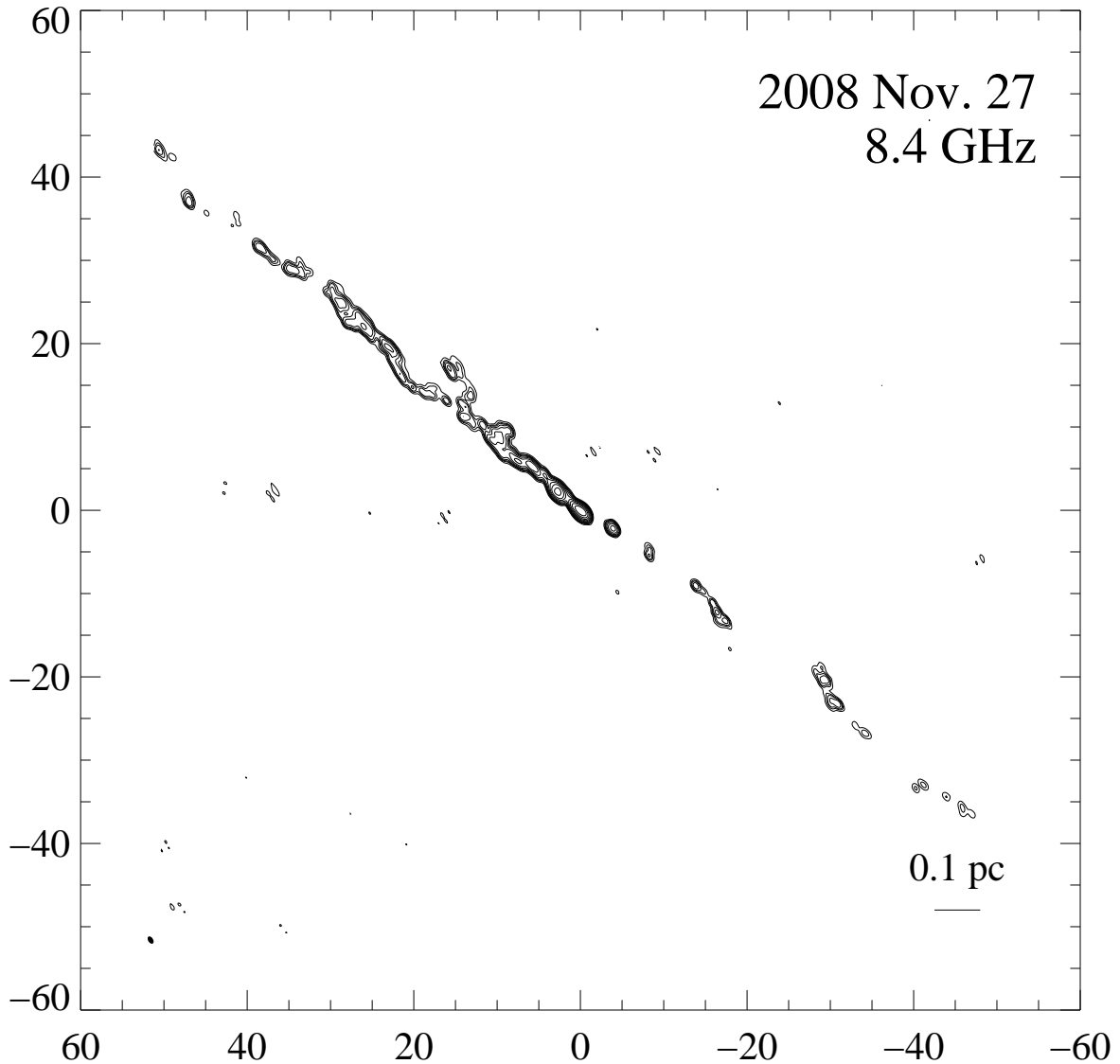
Figure 5.7: 8.4 GHz image of Cen A in November 2008 with natural weighting. The lowest contours denote the 3σ-noise-level (see Table 5.1). The axes are in units of mas.

good (u, v)-coverage for Southern Hemisphere monitoring. Thus, the visibility data are well suited for presenting the flow path of hybrid imaging. The visibility amplitudes and phases are inspected as function of time (Fig. 5.9) for every baseline and IF. The very first model marks the approximate scattering limits for the visibility data. Bad data points are flagged. DIFMAP allows the user to display the visibilities and the actually fitted model as a function of projected (u, v)-distance (depending on the angle) or the (u, v)-radius, respectively. Extended jet structures and their orientation in the (l, m)-plane can thus be identified visually before starting the imaging process. The widths of the resulting clean beams of every epoch, i.e., the resolution limit of the image, can be seen in Table 5.1 and

Figure 5.8: 8.4 GHz image of Cen A in September 2009 with natural weighting. The lowest contours denote the 3σ-noise-level (see Table 5.1). The axes are in units of mas.

represented as a gray ellipse in the lower left corner of the Figs. 5.6 to 5.8. The clean beam is represented by a two-dimensional ellipse with major and minor axis denoted as b_{maj} and b_{min}, respectively, and a position angle (P.A.) of the major axis, standing for the FWHM and orientation of a two-dimensional Gaussian. This specifies the smallest resolvable structures in each image, thus, the unresolved VLBI core region (see Sect. 3.3) is formed depending on the structure of the beam (Figs. 5.6 to 5.8 and 5.13). The angular resolution can be expressed in units of the linear extension, indicating the physical (but projected) size of the resolved jet features and the upper limit of the core size. Generally
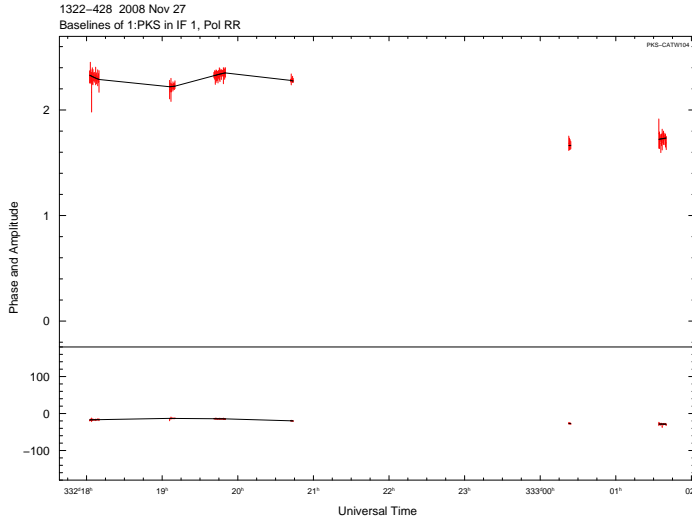
Figure 5.9: Example for visibility amplitudes and phases as function of time for the baseline between Parkes and Ceduna (IF 1) for the 8 GHz Nov. 2008 observations. The black curve denotes the fitted (and interpolated) `clean` model to the data (red).

Hubble's law for expansion of the local universe[4] is used to calculate the connection of redshift and distance, and consequently of linear extensions. Due to the proximity of Cen A, gravitation exceeds the Hubble flow, and therefore the linear scale has to be derived from the distance of 3.8 Mpc (Harris et al., 2009), which is determined independently from the optically measured redshift of $z = 0.001825$ (Saviane & Jerjen, 2007). At this distance, 1 mas corresponds to 0.018 pc (≈ 0.06 ly).

Earlier VLBI observations (see Sect. 5.1.2) led to a distinguished picture of Cen A's central region down to scales of less than one milliarcsecond. With only ground based telescopes, TANAMI achieved the highest linear resolution image of Cen A (and of an AGN jet) ever, comparable with earlier space-VLBI observations by Horiuchi et al. (2006). The size of the naturally weighted synthesized beam of the 3$^{\text{rd}}$ epoch is 0.59 mas ×0.98 mas. Hence, the smallest resolved structures are on a scale of less than 20 light-days. Expressing the scales in units of the Schwarzschild radius

$$r_{\text{S}} = \frac{2GM_{\text{BH}}}{c^2} \tag{5.1}$$

for Cen A with $M_{\text{BH}} = 5.5 \pm 3.0 \cdot 10^7 M_\odot$ (Cappellari et al., 2009), gives a resolution of $\sim 3500\, r_{\text{S}}$. The significant features within the sub-parsec scale jet seen in the November 2007 image of TANAMI observations (Ojha et al., 2010) are in good agreement with those of the two following epochs.

Even though the resolution of these first maps differs by ~ 1 mas, putting all information of these epochs together and matching significant jet features, performs a study of the central region of Cen A like never before. Multifrequency and multi-epoch observations provide better opportunities to make statements about the position of the radio core and moreover about the reliability of imaged features. The single-epoch space-VLBI image by Horiuchi et al. (2006) was by then the best resolved view on the central region of an AGN, but there was no observation to which these data could be compared to. As a result

---

[4] $cz \propto H_0 D$, with the Hubble constant $H_0 = 71 \text{km s}^{-1} \text{Mpc}^{-1}$, the speed of light c, the redshift z and the distance D in Mpc.

the core identification was not unambiguous. In this respect, the TANAMI observations have several advantages: First, the imaging results in a clear separation of the bright jet pointing towards the observer and the fainter counter-jet. Second, the combination of several epochs (at one or more frequencies) helps to set constraints on the position of the core via alignment of jet features (at a single observing frequency) or core-shift-analysis of multifrequency observations (details in Sect. 5.4.1). Finally, a comparison of the space-VLBI and the recent TANAMI observations can help to improve our knowledge of this nearby AGN jet on a time base of 8 years.

The close inspection and correlation of the jet features seen in the four images at 8 GHz and the additional dual-frequency epoch led to the following results. With the TANAMI array, the core region of Cen A, as seen by Tingay et al. (1998), can be resolved into several sub-components. At all epochs, a well collimated jet with an opening angle of $\leq 5°$ at a mean position angle of $\sim 50°$ and a fainter counterjet (P.A. $\sim -130°$) with an emission gap in between are seen. The flux density profiles for a narrow strap of 0.1 mas along this position angle are shown in Fig. 5.10.

The bright unresolved component at the phase center of each VLBI image dominates the jet emission at all epochs and at both frequencies. Due to remarkable similar appearance of the jet emission of all measurements, this feature will be denoted as 'the core' in the following. Also, a distinct division between the bright jet emission and the fainter counterjet features is observable. All observations show a decline in flux density along the jet and a rise at ~ 25 mas from the phase center. The peak flux densities at the 8.4 GHz epochs show only moderate variability with a mean of $S_{\text{peak}} \sim 0.71$ Jy beam^{-1} (see Table 5.1). The peak flux density at 22 GHz is higher than at 8 GHz indicating an inverted core spectrum (for more details, see Sect. 5.4). The evolution of the flux density of the core feature with time is shown in Fig. 5.11. The total flux density at 8 GHz stays almost constant for the first year of monitoring with a mean of $\langle S_{\text{total,8 GHz}} \rangle \sim 3.5$ Jy and drops to $S_{\text{total,8 GHz}} = 1.6$ Jy in the 4$^{\text{th}}$ epoch.

While investigating the 1$^{\text{st}}$ 8 GHz epoch (without further data) the shape of flux density distribution along the jet was quite puzzling as the clearly visible jet emission along the jet axis drops to noise level for ~ 8 mas. It was not clear if this decline in brightness is real or due to incomplete (u, v)-sampling. By comparing this emission region with its counterpart in later 8 GHz observations this feature could be confirmed: the Cen A jet exhibits a widening of the jet at $\sim 23 \pm 4$ mas with weaker emission and with a subsequent recollimation and again increasing surface brightness. At 8 GHz, this jet widening manifests in a hollow or concave shape of a length (along the jet flow direction) of ~ 8 mas and a width of ~ 5 mas. The strong collimation of $\leq 5°$ opening of the inner few mas from the core is therefore interrupted at ~ 18 mas further downstream. The widening can also be seen in the previous two 8 GHz epochs, but not as significant and therefore it has to be confirmed by higher resolved images. Taking this into account, the jet opening angle enlarges to $\sim 16°$. Even more interesting is the comparison of this jet region with the simultaneous dual-frequency images of November 2008. At 22 GHz (Fig. 5.13) the widening is not as obvious as in the lower frequency image (Fig. 5.7). Comparing both images shows that the bright 22 GHz emission at 25 ± 2 mas is embedded approximately in the concave emission feature seen at 8 GHz (see Fig. 5.19). This may suggest a local optical thick medium which cannot be seen at 8 GHz but reveals
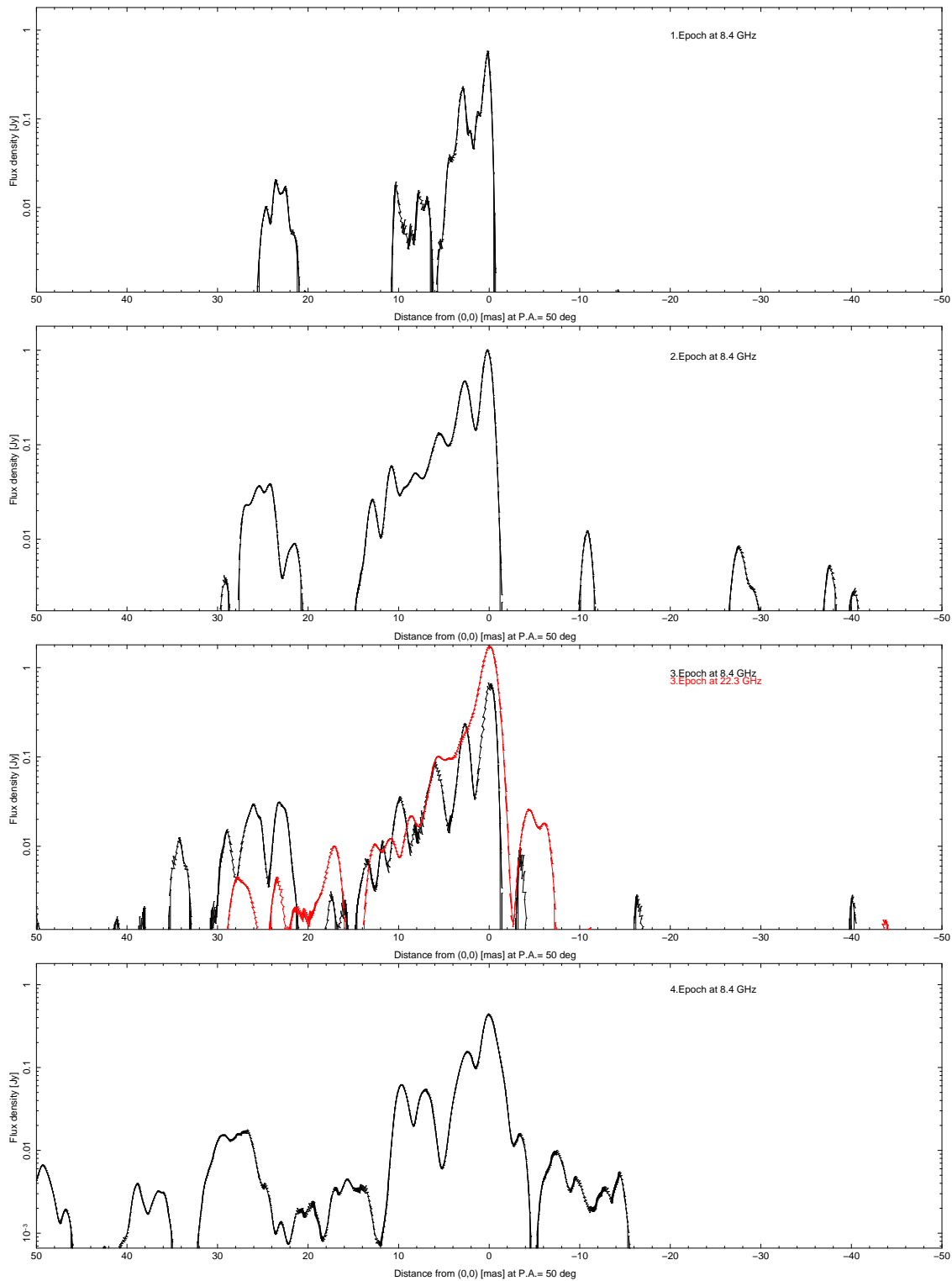
Figure 5.10: Flux density profiles (chronological order) for a narrow strap of 0.1 mas at a position angle of 50° (black: 8 GHz, red: 22 GHz, negative distances denote counterjet emission). The core region with the highest flux density and the bright stationary feature at ∼3.5 mas can be clearly seen.
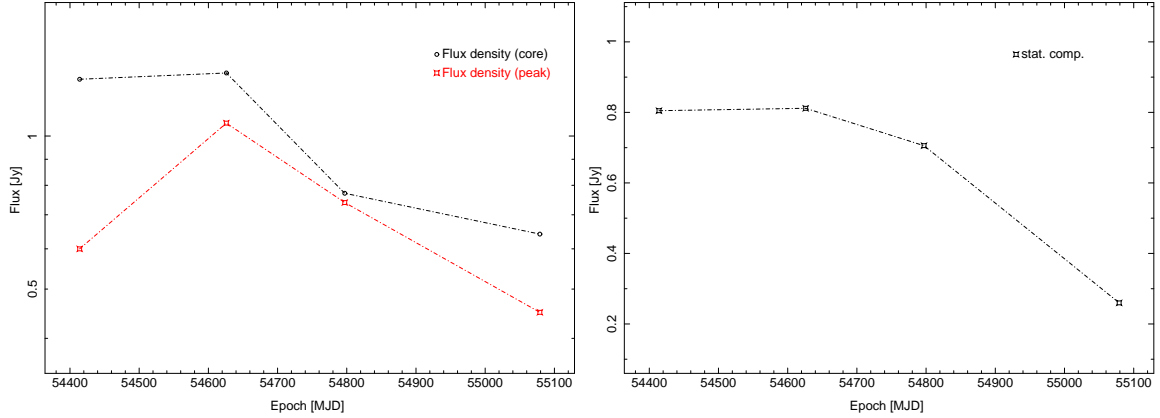
Figure 5.11: Time evolution of the flux density of the core (left) and the component (right)
at ∼3.5 mas (at 8.4 GHz). The core flux density was determined for the peak flux (in
red, see Table 5.1) and for the Gaussian component identified as the core (in black, see
Tables A.1 to A.4).

its appearance at higher frequency. However, due to incomplete (u, v)-sampling, imaging
uncertainties remain, and thus, the data can also be imaged fully suppressing emission
at ∼23 mas. Similar curious features can occur by disturbances within the jet or in the
ambient medium where the jet is breaking through and is then affected by absorption (e.g.,
Hardcastle et al., 2003; Kellermann et al., 2004; Jorstad et al., 2005). Discontinuities can
be stationary but also moving features. For example, an absorbing obstacle (e.g., gas clouds
or high-mass stars) can cause turbulences, instabilities, or standing shocks as well as the
ejection of a new jet component can change the smooth jet flow significantly. On the other
hand one would generally expect an expansion of the jet cone further downstream, after
the main collimation and acceleration zone, when considering an adiabatically expanding
relativistic plasma where the width of the jet cone depends mainly of the Mach number
(Falcke & Biermann, 1995). In this case, the recollimation afterwards is unexpected.

In this context, it is worth mentioning that there is a large similarity between the high res-
olution 8 GHz TANAMI images (November 2008 and September 2009) and the space-VLBI
image at 5 GHz by Horiuchi et al. (2006) of August 2000 illustrated in Fig. 5.12. Comparing
these two images of Cen A turns out to be challenging because of uncertainties based on
(u, v)-coverage and the long time interval. However, the construction of an overlay of these
comparable resolved images shows a couple of similarities. Especially the broadening of the
jet, in contrast to a strong collimation upstream, can be seen at almost the same distance
from the core. Later, in Sect. 5.5, the apparent motion of the Cen A jet will be discussed.
On the results of the jet speed analysis by Tingay et al. (2001), ∼2 mas yr^{-1}, one would
not expect to find many similar jet features (see Chapt. 6 for more detailed discussion). A
more careful comparison of the two data sets is needed to verify these findings.

In all maps and intensity profiles, respectively, a second bright and prominent component
besides the core is detected at ∼3.5 mas downstream. It seems to be stationary since it is
clearly detectable at all epochs and both wavelengths without evident movement. This jet
component plays an important role in the analysis of apparent jet motion discussed later in
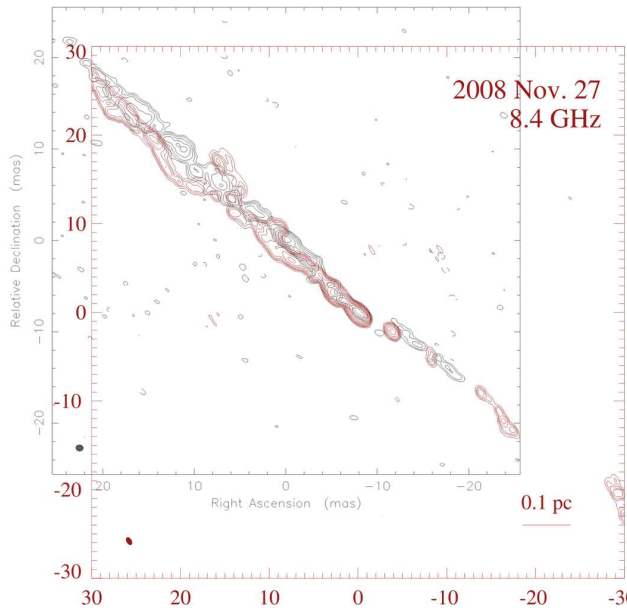
Figure 5.12: Comparison of the space-VLBI by Horiuchi et al. (2006) at 5 GHz of August 2000 (black) and the high resolution TANAMI image at 8 GHz of November 2008 with natural weighting (red). The two images are remarkable similar, especially the widening of the jet at ~ 23 mas jet downstream is consistent with a less collimated jet region.

Sect. 5.5. The flux density of this component shows a weak decline with time (Fig. 5.11).

The sub-parsec scale counterjet of Cen A was discovered for the first time by Jones et al. (1996). The TANAMI observations reveal a fainter counter-jet at P.A. of about 130°. Its components were partly resolved in November 2008 and can also be seen in the previous lower resolved maps. In the dual-frequency November 2008 images, a bright counterjet component close to the core can be identified at both frequencies. Due to limiting sensitivity the counterjet emission is marginally above the 3σ-level. Even though the alignment and comparison of counter-jet components of the first 8 GHz TANAMI observations is not successful, the detection is reliable. At 8 GHz, in the November 2008 image a small counterjet displacement from the jet axis is distinguishable, which can also be seen in the 5 GHz image of Horiuchi et al. (2006). At 22 GHz this offset is not as significant. The reliability of this shape was proven by the next epoch where the displacement is clearly visible.

To improve the resolution of these images, uniform weighting was applied. The resulting maps of all data sets are shown in Figures A.1 to A.5. The image parameters are listed in Table 5.2. As explained above, the image fidelity at uniform weighting is not as high as for natural weighting. Therefore the reliability of imaged features can be checked by comparing both maps (see Fig. A.6). For example, the displacement of the counterjet at 8.4 GHz in the 3rd epoch is also visible here. Then, the uniform maps provide the highest possible resolution, i.e., jet structures can be imaged rich in detail. As being the best example, Fig. 5.14 shows a zoom in the central region of the 8.4 GHz uniform map of November 2008 being the so far highest resolved view on an AGN jet ever.
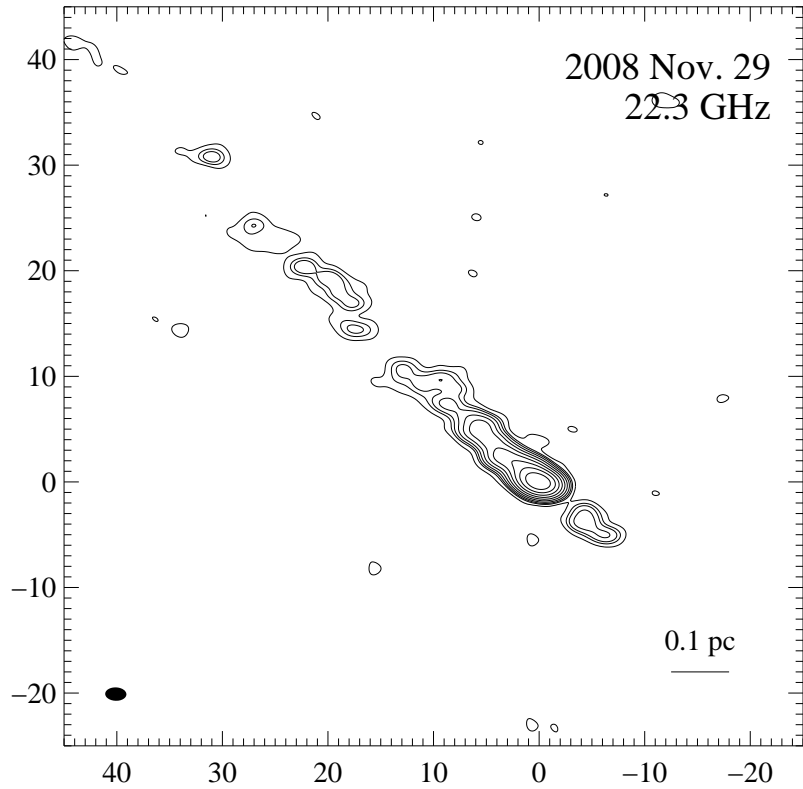
Figure 5.13: 22.3 GHz image of Cen A in November 2008 with natural weighting. The lowest contours denote the 3σ-noise-level (see Table 5.1). The axes are in units of mas.
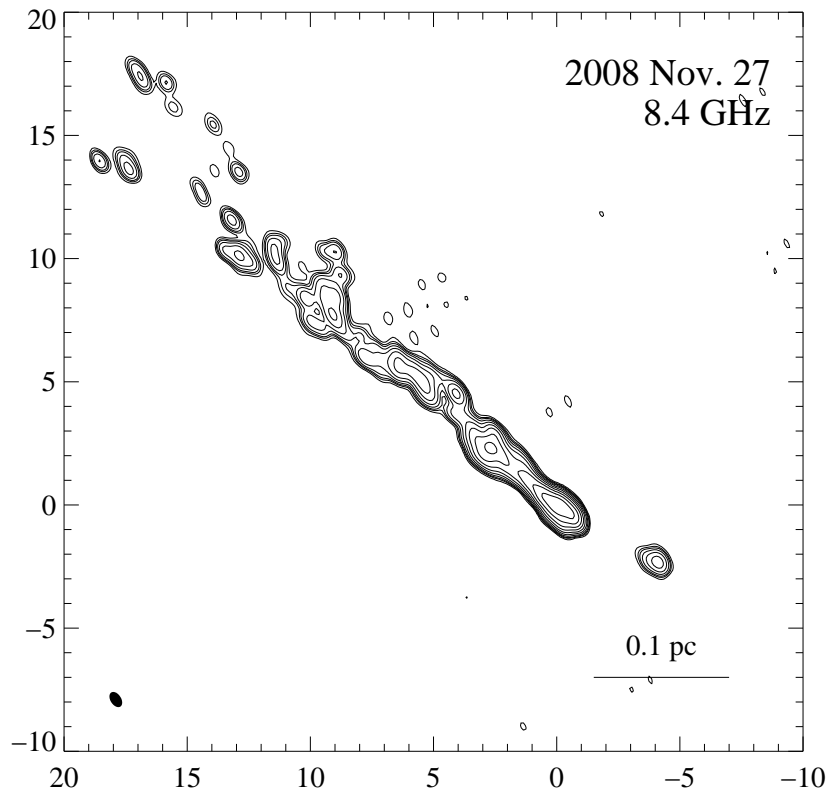
Figure 5.14: Close-up of the central part of the uniformly weighted 8.4 GHz image of Cen A in November 2008. This is the so far highest resolved image of the inner few lightdays of an AGN. The lowest contours denote the 3σ-noise-level (see Table 5.2). The axes are in units of mas.

Table 5.1: Image parameters and observation characteristics of naturally weighted maps

Frequency	Epoch	RMS	S_{peak}	$T^1_{\text{B,peak}}$	$T^2_{\text{B,core}}$	S_{total}	b_{maj}	b_{min}	P.A.	χ^2_{red}
[GHz]	yyyy-mm-dd/MJD	[mJy beam^{-1}]	[Jy beam^{-1}]	[10^{10}K]	[10^{10}K]	[Jy]	[mas]	[mas]	[°]	
8.4	2007-11-10/54414	0.37 ±0.04	0.60	1.5	5.51	2.6 ±0.1	1.64	0.41	7.9	0.38
8.4	2008-06-09/54626	0.58 ±0.05	1.06	0.54	3.77	3.1 ±0.1	2.86	1.18	−12.7	0.37
8.4	2008-11-27/54797	0.39 ±0.02	0.74	2.2	14.7	3.9 ±0.1	0.98	0.59	31.4	0.30
8.4	2009-09-05/55079	0.22 ±0.02	0.45	0.3	2.81	1.6 ±0.1	2.93	0.90	15.6	0.26
22.3	2008-11-29/54842	0.47 ±0.03	1.77	0.17	3.97	3.4 ±0.1	2.01	1.27	87.9	0.20

[1] T_B calculated according to Eq. 4.6 using S_{peak}, b_{maj} & b_{min}
[2] T_B calculated according to Eq. 4.6 using S_{Core} from Tables A.1 to A.5

Table 5.2: Image parameters and observation characteristics uniformly weighted maps

Frequency	Epoch	RMS	S_{peak}	S_{total}	b_{maj}	b_{min}	P.A.	χ^2_{red}
[GHz]	yyyy-mm-dd/MJD	[mJy beam^{-1}]	[Jy beam^{-1}]	[Jy]	[mas]	[mas]	[°]	
8.4	2007-11-10/54414	0.41 ±0.01	0.4	1.73 ±0.1	1.52	0.33	5.7	0.71
8.4	2008-06-09/54626	0.5 ±0.04	0.98	3.24 ±0.1	2.74	0.69	−11.9	0.52
8.4	2008-11-27/54797	0.45 ±0.02	0.48	3.17 ±0.1	0.68	0.43	33.2	0.34
8.4	2009-09-05/55079	0.6 ±0.02	0.3	1.55 ±0.1	1.98	0.46	15.3	0.35
22.3	2008-11-29/54842	1.2 ±0.1	1.46	3.30 ±0.1	1.55	1.21	−75.3	0.35
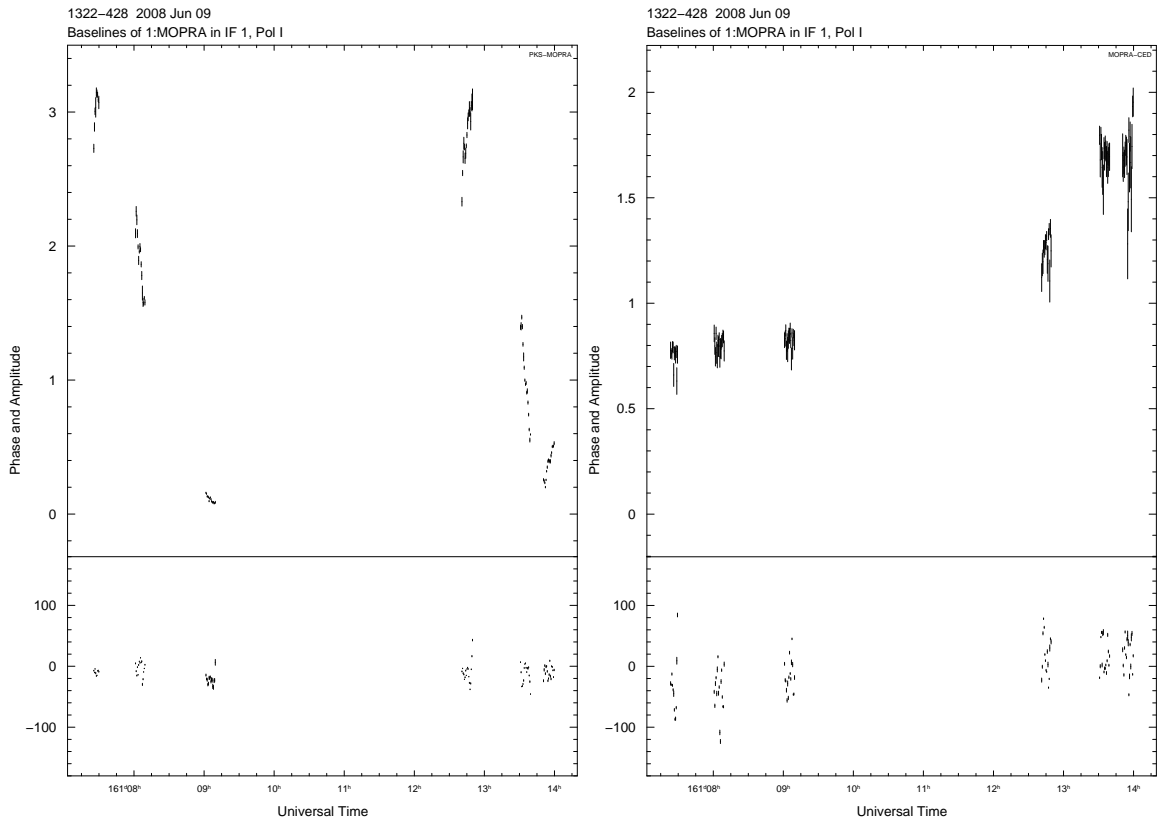
Figure 5.15: Example of affected visibilities (before calibration) for the Parkes-Mopra baseline (left), showing a strong variability, and unaffected Ceduna-Mopra data (right). Such comparisons led to the result that the failure was antenna based.

5.2.2 Successful data reconstruction - Imaging with defective visibility measurements

The first two TANAMI data sets of Cen A had similar initial conditions of (u, v)-coverage because of similar array configurations (except for the ATCA positions CATW113 and CATW109, respectively). Nevertheless the achieved resolution and image fidelity of the 2nd epoch map was worse. This was due to the fact that the Parkes data showed a peculiar behaviour during this experiment (see Fig. 5.15) with respect to all visibilities on all baselines. The comparison of different baseline measurements via `vplot` led to the result that at this epoch the receiving or recording device at Parkes obviously suffered from a major failure. All visibilities measured by baselines including Parkes were affected and showed a strong variability in the visibility amplitude of a factor $\sim$3 while at all other baselines the measured visibility amplitude was almost constant. Parkes is an important telescope of the Southern Hemisphere VLBI array, providing high baseline sensitivity thanks to its large reflector size. The calibration parameters determined from all other telescopes were used to self-calibrate the Parkes measurements.

The imaging process with such poorly calibrated data acts in the following way:

1. The identified disturbance source (here: Parkes) can be eliminated by flagging all visibility data.

2. For all unaffected visibilities the `clean`ing and amplitude self-calibration process described in Sect. 4.3.2 can be applied until a reliable model is established. One amplitude self-calibration step is applied using a constant correction factor for each telescope.

3. This model with a well-balanced amplitude and phase correction can then be used to to calibrate the bad data. To avoid a destruction of this supporting model all visibility data are frozen except the ones which need re-calibration. Another amplitude and phase self-calibration step with a short solution interval operates now on the elaborately constructed model. This leads to an amplitude correction for the defective data compatible with all other baselines.

4. Based on this calibration a new model can be build involving the adjusted data.

This procedure is quite effective as Fig. 5.6 demonstrates. However, the malfunction can not be completely erased and still a decrease in sensitivity and resolution remains. The reconstruction of the Cen A data of June 2008 was successful in that the imaging result can be used for further analysis (see Sect. 5.3).

5.2.3 Consistency and reliability checks for `clean` maps

As the previous section demonstrates, reliability checks of raw data, calibration parameters as well as resulting `clean`-models are important and should be conducted consequently. The most important steps, which were applied to the Cen A data, are shortly summarized in the following. Before starting the `clean`-algorithm, the examination of the raw data in `DIFMAP` is crucial. Disturbance effects can be already discovered and (see above) eliminated. Bad data points are flagged, avoiding influences on the subsequent calibration process. The latter approach is continuously performed during the whole imaging procedure. In order to check the validity of calibration steps, the calibrated and the raw data are compared based on the resulting `clean`-model. Bad visibility points may affect the calculations. This can lead to, e.g., down weighting of baselines and consequently changing observation parameters like flux density or resolution. The reliability of position and appearance of weaker imaged structures may depend on the placements of `clean`-windows. To test this, one relies only on emission features exceeding a certain flux density limit. In general this cutoff is defined as "3σ-confidence-limit", assuming Gaussian noise with a certain RMS $(= \sigma)$ value. Only emission features with flux values above this threshold are considered to be reliable. However, these weak features should be treated with caution. By rearranging or deleting of `clean`-windows, the significance of weaker emission feature can be inspected. Thus, modeling artificial effects from local sidelobe maxima can be avoided. Furthermore, independently imaging the same visibility data with different (u, v)-weighting offers also an accuracy check of weaker intensity structures. Naturally weighted images have a higher sensitivity. Hence, no significant emission should be seen in the uniformly weighted map outside the 3σ-contours of the natural one. This approach constrains the uniform-image

(see Fig. A.6). Finally, the visibility data can also be approximated by a more simple model. Modeling the visibility data with model components with an elliptical Gaussian emission profile addresses the brightest regions, i.e., the most significant structures. This provides another independent opportunity to check whether `clean`ed emission is trustworthy and can also be represented by a simplistic model. The next section will discuss this kind of modeling in further detail.

5.3 Model fitting

After calibration and imaging of the VLBI data sets, the visibility data were also fitted with a much simpler model. To make statements about jet kinematics or spectral changes, an easy parametrization of the (u, v)-data consisting of only a few model components with a two-dimensional Gaussian intensity profile was chosen. Modeling the data with such Gaussian model components is similar to the `clean`ing process. The big advantage of applying a small number of circular or elliptical Gaussians components instead of several hundred point sources (convolved with the `clean` beam) is the reduction in the number of degrees of freedom. Thus, one avoids an over-interpretation of visibility data, especially of incomplete (u, v)-coverage. Fitting such a model is sufficient to describe the positions and flux densities of major jet features. Furthermore, the comparison of different data sets is facilitated.

The well self-calibrated and adjusted Cen A (u, v)-data with natural weighting are approximated by Gaussian model components. At first, the bright core feature is represented by one component. Multiple other components are included in the model while permanently inspecting the residual map to identify the main jet emission regions. The `modelfit`-algorithm is based on the Levenberg-Marquardt non-linear least squares minimization technique (Levenberg, 1944; Bevington & Robinson, 2003). It fits directly the real and imaginary part of the visibility data points. `Selfcal` steps are required in order to converge on the model consistent with the closure phases. The Gaussian model components are determined by their FWHM in two dimensions (represented by major and minor axis), the flux density, the position, and, in case of an elliptical component, the position angle (P.A.) of the ellipse orientation. `DIFMAP` allows to fix or vary the individual properties to find the minimal deviation between model and observed visibilities. The goodness of the fit is expressed by the value of the reduced chi-squared. The χ^2_{red} is defined as the sum of the squared differences between model and data divided by the number of degrees of freedom n

$$\chi^2_{\mathrm{red}} = \frac{\sum_i (y_i - f(x_i))^2}{n} \quad . \tag{5.2}$$

This gives the quality of the fit, where $\chi^2_{\mathrm{red}} \approx 1$ represents a well-suited one. Due to self-calibration of the visibility data in `DIFMAP`, the uncertainties in flux density are often over estimated. Hence, a reasonable comparison of the fit quality can only performed between the χ^2 values of the `clean`ing and the `modelfit`ing results, respectively.

It is important to note that `DIFMAP` provides no possibility to determine the uncertainty for position and flux density for individual components. Therefore, only absolute values

without error bars are given. This affects particularly the kinematic analysis (see Sect. 5.5), where only unweighted linear regressions can be performed implying several presumptions. To determine a correct error estimation for a more reliable interpretation of these fits, a detailed χ^2-analysis would be necessary. By varying all free parameters of the model, suitable confidence levels for position and flux density can be derived. This cannot be done by hand and, thus, an algorithm will be applied in the future to do these computations (see Sect. 6.2). The analysis presented in this diploma thesis is using only the absolute fit values provided by `DIFMAP` and disregards the comprised uncertainties.

5.3.1 Multi-epoch analysis

The model fitting was performed for all epochs and both frequencies first independently of each other. The goal was to find a suitable model, which can be used for tracking the same individual jet components with time (jet kinematics, see Sect. 5.5) and for constructing a spectral-index map (see Sect. 5.4).

In Table A.1 to A.5, the best fit parameters for each data set are given. The position of the Gaussian model components is given in R, which is the distance of designated phase center in mas, and the orientation angle θ (measured counter-clockwise). Since this simpler model is the complement to the significant and bright jet emission regions seen in the `clean`-model, it is useful to compare both models for consistency. In Figs. 5.16 to 5.18 an overlay of both models is presented giving also the FWHM of each Gaussian component.

In general, a Gaussian emission component which is fitted to the visibility data 'joins' the flux distribution around its position and smears out detailed structure information, i.e., such emission zones can hardly be modeled by Gaussian emission features. Therefore, diffuse and expanded emission (near the 3σ threshold) can be represented by one component with typically a broad FWHM. This effect can be clearly seen at all epochs, where the broadened region at $R \sim 23$ mas jet-upstream is underrepresented by Gaussians compared to the emission contours of the `clean` image. Later, for the jet kinematic analysis (see Sect. 5.5), these model components, which represent insignificant or diffuse jet emission, have to be treated with particular caution since their position is more uncertain.

The fitting of Gaussian emission features to the visibility data results in a coincident model for each observation epoch permitting to identify the major jet features. Moreover, the significant emission of the counterjet seen in the `clean` image can be represented. However, due to varying sensibility of the measurements, the search for explicit component complements for different epochs was only successful for the jet.

5.3.2 Identifications of model components and consistency checks

There is a set of methods, which were applied to the '`modelfits`' in order to check the consistency of both models for the visibility data. After building up such a simpler model out of Gaussian components for each epoch, cross identifications are necessary for further investigations.
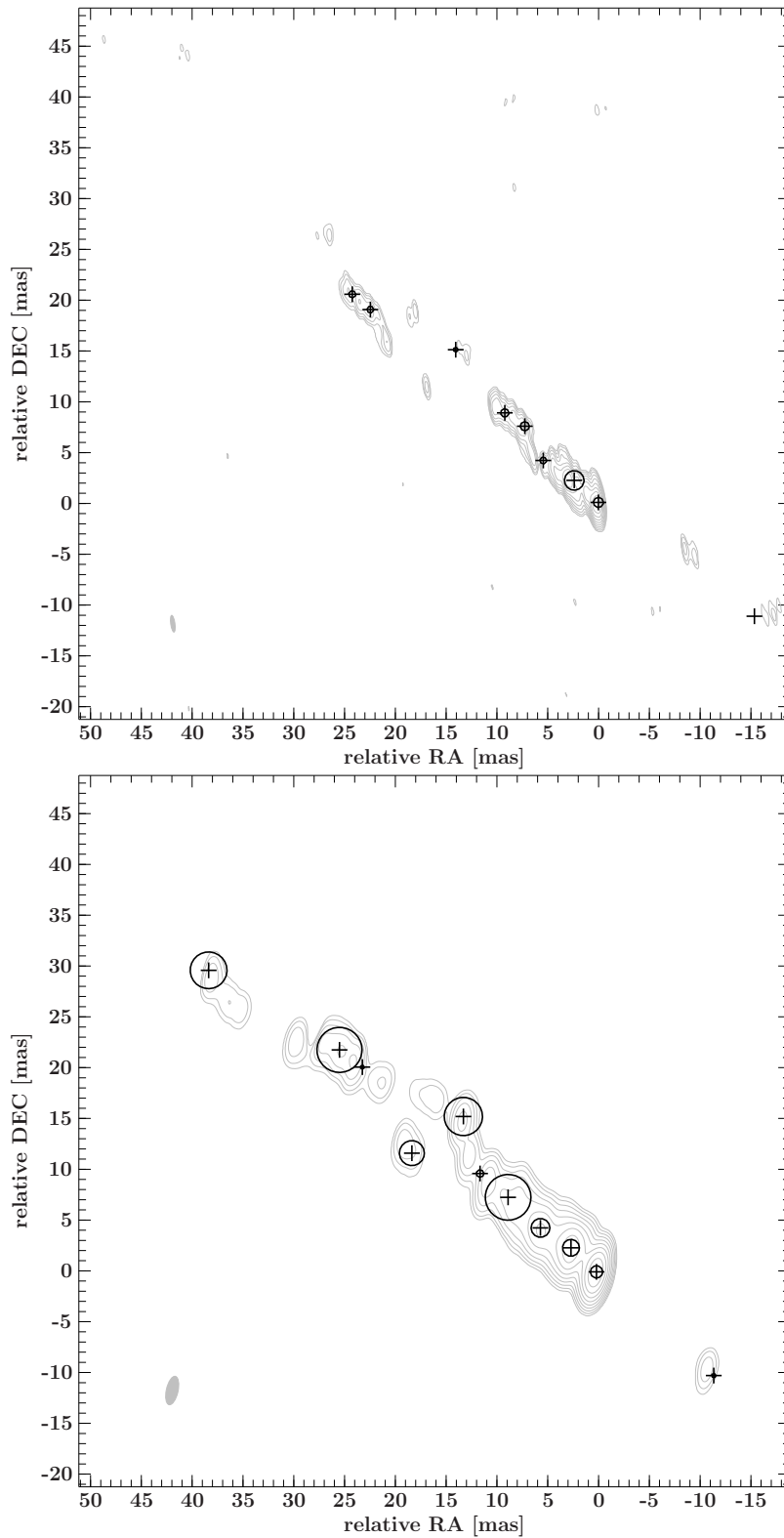
Figure 5.16: Positions of circular Gaussian components (black) in comparison to the
clean image (gray) at 8.4 GHz of Nov. 2007 (top) and June 2008 (bottom). The crosses
denote central positions of Gaussian components with the symbol size representing the
major axis of each component.
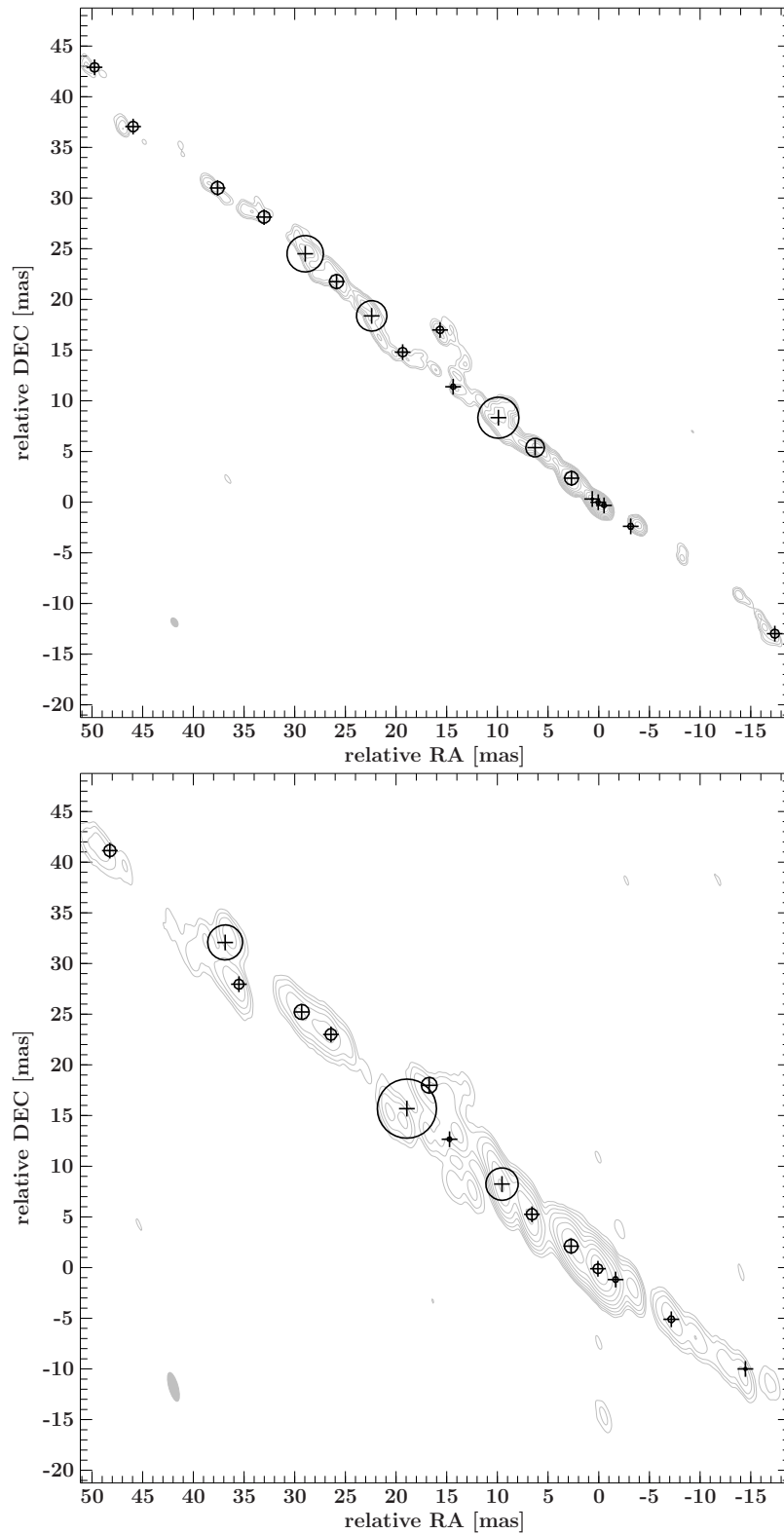
Figure 5.17: Positions of circular Gaussian components (black) in comparison to the
clean image (gray) at 8.4 GHz of Nov. 2008 (top) and Sept. 2009 (bottom). The crosses
denote central positions of Gaussian components with the symbol size representing the
major axis of each component.
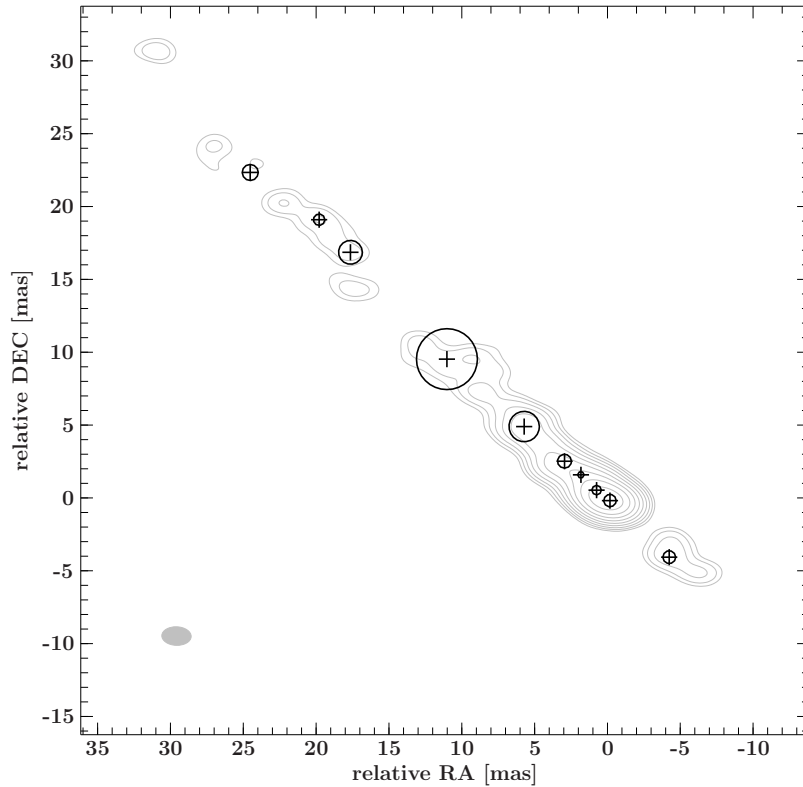
Figure 5.18: Positions of Gaussian components (black) in comparison to the `clean` image (gray) at 22 GHz of Nov. 2008. The crosses denote central positions of Gaussian components with the symbol size representing the major axis of each component.

1. The visibility data were modeled independently in two different ways. At first, every data set is imaged with Gaussians without any comparison to the `clean` model. This avoids over-interpretation of jet structures since only the most significant emission zones were considered. Secondly, the individual data sets of every epoch were modeled independently in order to be not biased.

2. The χ^2-test is crucial. With continuously removing and adding of components and meanwhile checking the differing χ^2-value, the best fit can be found.

3. Overlay images help to constrain the reliability of model components. An overlay of both, `clean` and `modelfit` results, is useful to check the consistency between both models. Significant ($\geq 3\sigma$) emission regions should be represented by Gaussian components with comparable positions, flux density values and FWHM.

4. For the cross identification of model components of separated epochs, one has to be aware of new components showing up with time. For high resolution images, significant jet features can help to cross-identify components belonging together.

If the model satisfies the criteria of these checks, smaller adjustments among the individual epochs can be made, e.g., simplifications for complicated jet structures when comparing with the models of previous and following epochs. For example, the model for the first

8 GHz epoch was simplified by modeling only one Gaussian component instead of two nearly identical ones to the core feature. This formally enlarges the χ^2_{red} value but for the kinematic analysis this simpler model is more convenient and improves the self-consistency of the final multi-epoch model.

5.4 Spectral analysis

In this section, the quasi-simultaneous observations at 8.4 GHz and 22.3 GHz of November 2008 were used to construct a *spectral-index map* giving the spectral characteristics of the spatially resolved features along the Cen A jet. High resolution radio measurements provide the only way to determine and resolve the location of spectral changes along the jet.

5.4.1 Spectral-index maps

Assuming a powerlaw distribution to describe the radio part of the synchrotron spectrum ($S_\nu \propto \nu^\alpha$), the spectral slope between the two frequencies 8 GHz and 22 GHz is given by the spectral index

$$\alpha = \frac{\log(S_{22.3\,\mathrm{GHz}}) - \log(S_{8.4\,\mathrm{GHz}})}{\log(22.3\,\mathrm{GHz}) - \log(8.4\,\mathrm{GHz})} \quad . \tag{5.3}$$

To construct a spectral-index map, i.e., an illustration of the distribution of α along the jet, the logarithm of both images is calculated with subsequently subtracting of each other.

VLBI imaging provides indeed the highest resolution images but the phase-calibration process based on closure phases results in the loss of the absolute position of the observed source[5]. Hence, for determining the position dependent α, a careful alignment of the two images has to be performed. With Eq. 3.12 to 3.14 it can be shown that for a higher observing frequency ν_{obs} the position of the core is shifted (*core-shift*). This is a result of decreasing optical depth τ_ν with higher ν_{obs}, i.e., a shift of the ($\tau = 1$)-surface towards the AGN center. Figure 3.4 illustrates this correlation between the position of the ($\tau = 1$)-surface and the observing frequency. In general, the core of the jet is the brightest feature of a VLBI image but due to absorption, images at two different frequencies are affected by the core shift (Kovalev et al., 2008). For calculating a spectral-index map, a correct alignment is feasible by matching the corresponding optically thin components in each image (e.g., stationary or relativistic moving jet knots, see Fig. 3.4) which are not affected by absorption. Therefore, the Gaussian model components representing the unabsorbed jet features are well suited to perform this alignment. After correctly adjusting the two images the spectral index α can be calculated. Without a proper core-shift analysis, the incorrect matching of components can result in a miscalculation of α and, thus, misleading conclusions about the physical conditions of the jet emission and absorption processes.

---

[5]In order to obtain the absolute position of a source, phase-referencing observations are necessary.

5.4.2 Simultaneous dual-frequency observations of Cen A

AGN jets can be highly variable, thus, it is important to collect spectral information as simultaneous as possible. The quasi-simultaneous dual-frequency TANAMI observations of Cen A of November 2008 at 8.4 GHz and 22.3 GHz are separated by two days. In the radio band, extragalactic jets show generally only flux variations of weeks (e.g., Fan et al., 2007; Hovatta et al., 2007), thus, a time span of a few days is compatible with the simultaneity requirement. These data can be used to calculate a spectral-index map for the inner few lightdays of the Cen A jet.

The two visibility data sets were imaged and model fitted independently of each other. After applying the consistency checks (see Sect. 5.3.1), both Gaussian models were simplified in order to achieve a self-consistent dual-frequency model. To compensate for the core shift, the optical thin model components of both images were identified and aligned (see Fig 5.19). The comparison of the optically thin components reveals a relative shift of the 22.3 GHz image with respect to the 8.4 GHz core in the direction of the central black hole of $\Delta\alpha \approx 0.25$ mas and $\Delta\delta \approx 0.2$ mas. As theoretical considerations predict, the 22 GHz core is closer to the AGN center (cf. Fig. 3.4). The prominent component at 3.58 mas (at 8 GHz), which seems to be stationary (see Sect. 5.2 and 5.5), played an important role for this analysis. At 22 GHz this component has a distance of 3.88 mas from the designated phase center giving the determined core shift. It can be seen in Fig. 5.21 that the spectrum of this component is almost flat to optically thin. Since it appears in every epoch and at different frequencies, it can be used as a 'marker' to determine the proper shift. As mentioned above, the positional uncertainties of the components cannot easily be obtained. These uncertainties need to be considered when determining the core shift.

Taking this alignment correction into account, the spectral index distribution along the jet shown in Fig. 5.20 was obtained. The spectral index was calculated according to Eq. 5.3 for $S_{8.4\,\mathrm{GHz}} \geq 3\sigma_{8.4\,\mathrm{GHz}}$ and $S_{22.3\,\mathrm{GHz}} \geq 3\sigma_{22.3\,\mathrm{GHz}}$ for the `clean` maps. This threshold is used to reduce remaining sidelobe effects (Lobanov, 1998). Both images were restored with a common beam (80% of synthesized beam at 22.3 GHz; (1.61×1.02) mas, P.A. 88°) in order to avoid over-interpretation of lower resolved 22 GHz features and to reduce effects of uneven (u, v)-sampling of the two images relative to each other. The core has an inverted spectrum which changes from to a flat spectral index downstream. The highest spectral indices with values $\alpha \geq 1$ are found in the core, indicating absorption. A clear distinction between free-free or synchrotron-self absorption cannot be made from these results (cf. Eqs. 3.5 and 3.12). Tingay & Murphy (2001) stated that the highly inverted spectrum near the nucleus can be explained by intrinsic synchrotron-self absorption and additional extrinsic absorption since the value of α drops down to values where an explanation with free-free absorption is necessary. This is not seen in Fig. 5.20. While free-free absorption may contribute to the overall absorption, a pure synchrotron-self absorption scenario cannot be ruled out. Figure 5.21 shows an overlay of the flux density profiles along the jet at a P.A.=50° for both frequencies (corrected for the core shift). The lower panel presents the variation of α along this jet axis. Besides the core, the spectral index is of the order of $\alpha \sim \pm 0$, thus, showing a remarkably flat spectrum for the inner few milliarcseconds. The jet region within the first $\sim$6 mas has an inverted spectrum, which changes to almost flat
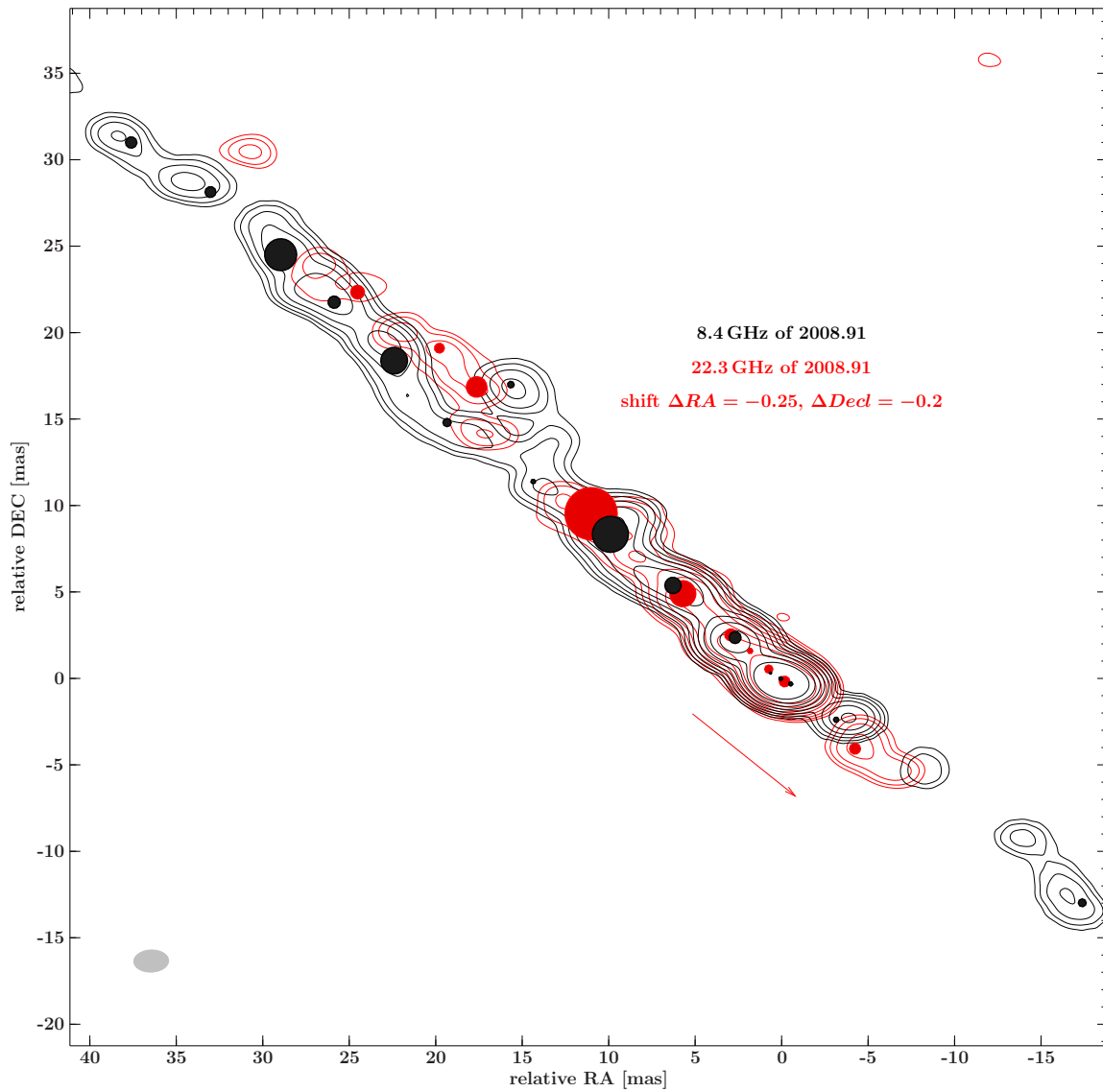
Figure 5.19: Result of core shift analysis: The 22.3 GHz image (red) is affected by a shift of $\Delta\alpha \approx -0.25$ mas and $\Delta\delta \approx -0.2$ mas with respect to the 8.4 GHz image (black). Both images are restored with a common beam of (2.01×1.27) mas at P.A. 87.9° (represented by the gray ellipse in the lower left corner). The filled circles present the FWHM of the Gaussian components at each frequency. Here, the higher resolved 8.4 GHz image was restored with the `clean` beam at 22.3 GHz. The red arrow displays the direction the core shift of the 22 GHz image enlarged by a factor of 10.

($\alpha \sim \pm 0$) for the prominent bright (stationary) component at ~ 3.5 mas. Subsequently, the spectrum steepens again with $\alpha \geq 1$. The widening of the jet (at a distance of ~ 23 mas from the phase center) at 8.4 GHz with accompanied decreasing of flux can be clearly seen. Contrary, at 22.3 GHz, significant emission is detected, which leads to an extremely inverted spectrum. The spectral index is only physically meaningful for overlaying jet features of
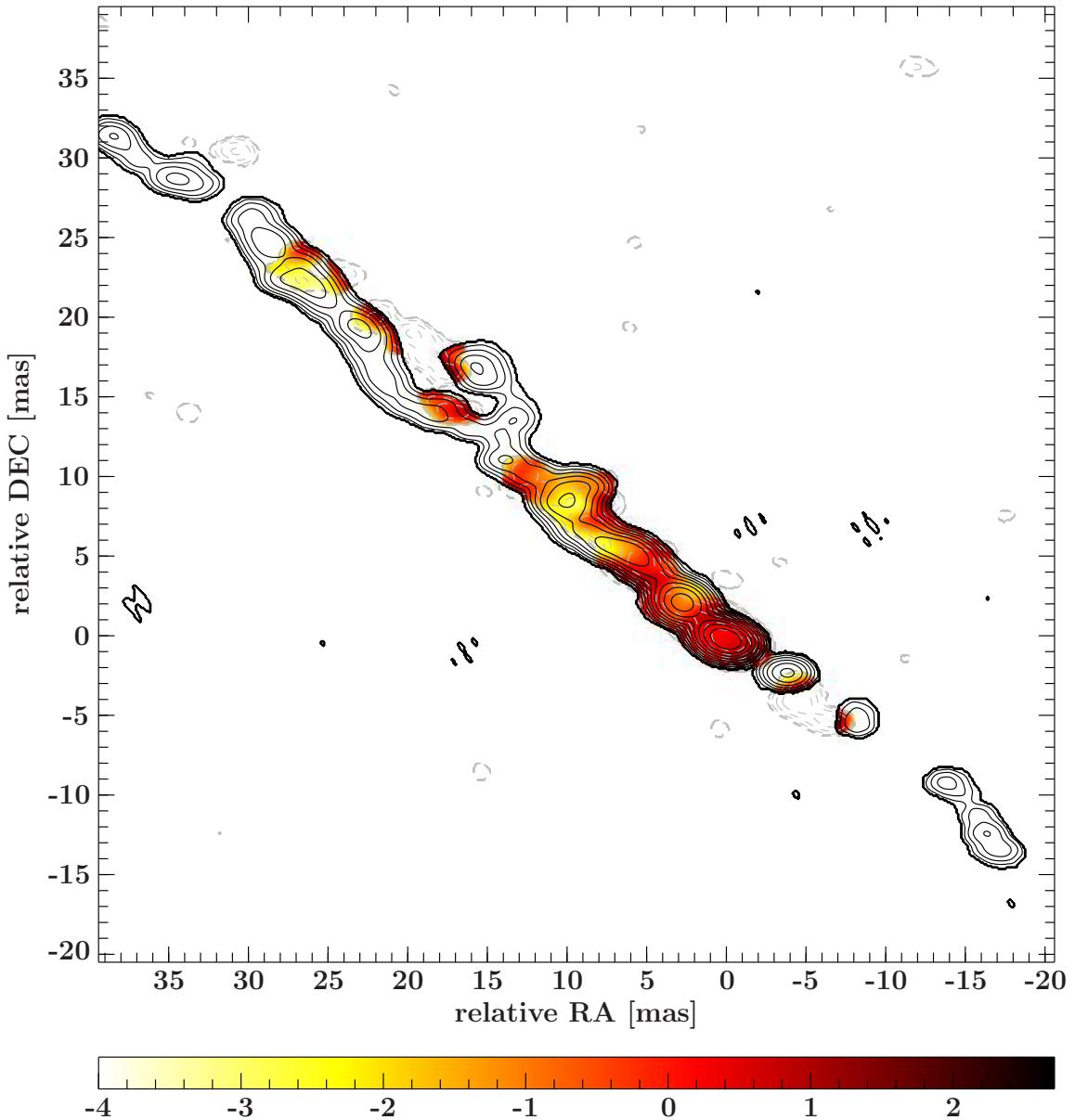
Figure 5.20: Spectral index map as calculated for $S_{8.4\,\mathrm{GHz}} \geq 3\sigma_{8.4\,\mathrm{GHz}}$ and $S_{22.3\,\mathrm{GHz}} \geq 3\sigma_{22.3\,\mathrm{GHz}}$. The spectral index α is defined as $S_\nu \propto \nu^{+\alpha}$. The color scheme represents the spatial spectral-index distribution. The overlaid contours show the flux density distribution at $8.4\,\mathrm{GHz}$ (solid black) and at $22.3\,\mathrm{GHz}$ (dashed gray), both restored with a common beam of $(1.61 \times 1.02)\,\mathrm{mas}$ with a P.A. $= 88°$ (see also Müller et al., 2010).

at both frequencies. Hence, the outer part of the spectral-index map, where significant emission zones and regions at noise level coincidence, need to be treated with caution.

The location of the recent detection of γ-ray emission from the Cen A core by *Fermi*/LAT (Abdo et al., 2010c) can be constrained with this result. Flat spectrum regions in the sub-
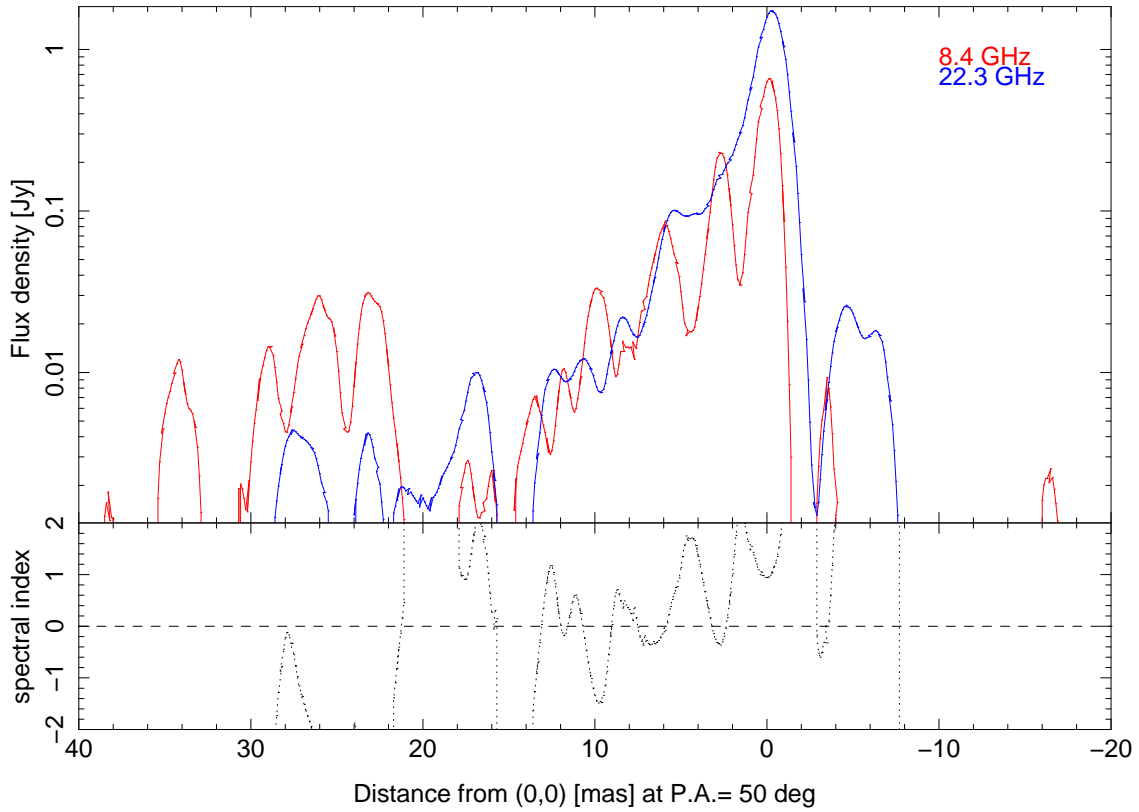
Figure 5.21: Flux density (top) at $8\,\mathrm{GHz}$ (red) and $22\,\mathrm{GHz}$ (blue) and spectral index (bottom) distribution for a narrow strap of $0.1\,\mathrm{mas}$ along jet at a P.A.$=50°$ corrected for the core shift of $\Delta\alpha \approx -0.25\,\mathrm{mas}$ and $\Delta\delta \approx -0.2\,\mathrm{mas}$.

parsec scale radio jet are possible production regions of high energetic photons (Marscher, 2009). In the optical thick emission zones of a jet photons can be upscattered to higher energies by relativistic particles. Hence, the inner $\sim\!6\,\mathrm{mas}$ ($\sim\!0.15\,\mathrm{pc}$) of the Cen A radio jet can be identified as possible sources of γ-ray emission with the strongest inverted-spectral emission coming from the jet core on scales of $\leq 0.05\,\mathrm{pc}$. Also for the counterjet, an optical thick emission region can be identified. The core region shows distinct spectral changes within the innermost $3\,\mathrm{mas}$ (see Fig. 5.20). At $\sim\!5\,\mathrm{mas}$ downstream of the jet, a subsequent rise of the spectral index is detected. Fujisawa et al. (2000) claimed a detection of a large jet bending around $\geq 3\,\mathrm{mas}$ away from the phase center which might be identical with the second bright stationary component. Such structure can explain an increase of the observed optical thickness (Jorstad et al., 2001b) regarding Doppler beaming effects. However, Horiuchi et al. (2006) did not find any recognizable bending in their image. This high resolution observation confirms this result as no significant jet bending is seen, only a slight kink might be present at a distance of $\sim\!8\,\mathrm{mas}$. Further observations need to confirm these possible high energy emission sites.

The spectral index $\alpha_{8,22\,\mathrm{GHz}}$ displays the change of the spectral slope between the both observing frequencies $8\,\mathrm{GHz}$ and $22\,\mathrm{GHz}$. To determine exactly the turnover frequency ν_t
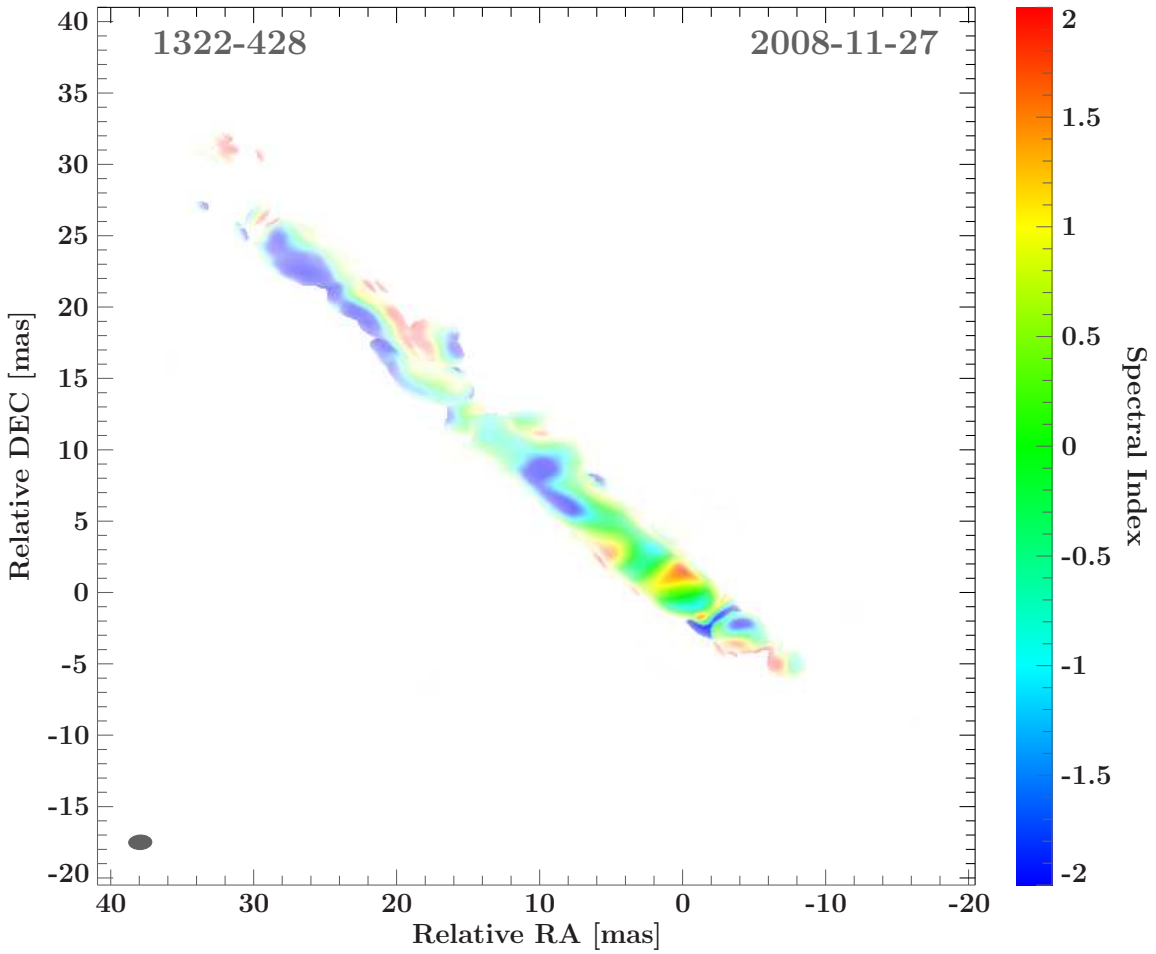
Figure 5.22: Spectral-index map (for 8 GHz and 22 GHz observation of November 2008) determined with the cross-correlation method excluding the core. The resulting spectral index per pixel is weighted depending on the corresponding cross correlation value. The color scheme represents the spatial spectral index distribution.

(cf. Eq. 3.14) a larger spectral coverage in the radio band is required.

Alternatively to the method applied above, one can use a normalized cross-correlation method to find the proper alignment of two images. The normalized cross correlation coefficient $CCC(a, b)$ for the overlapping region restricted by (a, b) is defined after Lewis (1995)

$$CCC(a, b) = \frac{\sum_{x,y}[f(x, y) - \bar{f}_{a,b}][t(x - a, y - b) - \bar{t}]}{\sqrt{\sum_{x,y}[f(x, y) - \bar{f}_{a,b}]^2 \sum_{x,y}[t(x - a, y - b) - \bar{t}]^2}} \tag{5.4}$$

with $\bar{t}$ being the mean of the feature located at (a, b) and $\bar{f}_{a,b}$ being the mean of the image in the region under the feature. The maximum correlation is therefore given by unity. A cross-correlation algorithm[6] was applied to the dual-frequency November 2008 images excluding

---

[6]These calculations could be made thanks to the work of Christian Fromm (MPIfR), Christoph Grossberger,

the core region (by using the beam size). The images are shifted with respect to each other to determine the cross correlation coefficient for each pixel. For every shift position the spectral index is calculated and weighted by the corresponding cross correlation result. This method leads to a (smeared-out) spectral-index map including the uncertainty for the determined shift (see Fig. 5.22). The CCC has high values along the jet ridge line and especially for an almost direct match of the inner few mas. Spectral indices calculated for shifts with high CCC values get a higher weight. Hence, this result is consistent with the calculation presented above: this smeared-out, averaged spectral-index map results in a flat to inverted spectrum for the inner few mas for all shifts specifying the region with the highest optical depth.

5.5 Jet kinematic analysis

In the following section the relativistic motion of the subparsec jet of Cen A is investigated. Figure 5.23 shows a composite of all four 8. GHz observations used for this analysis. In general, it is expected, that most of the jet components move with a similar characteristic velocity representing an underlying continuous bulk flow. However, jet often show also stationary or apparently inward-moving components (e.g., Kellermann et al., 2004).

Previous VLBI studies over a 10 years period of the inner Cen A jet by Tingay et al. (1998) and Tingay et al. (2001) resulted in a kinematical model with an overall angular motion $1.7^{+0.5}_{-0.2}\,\mathrm{mas\,yr^{-1}}$ corresponding to an apparent speed of $\beta_{\mathrm{app}} = \frac{v_{\mathrm{app}}}{c} = 0.11^{+0.03}_{-0.01}$. These authors achieved to analyze three distinguishable components with a restoring beam of $(3 \times 13)\,\mathrm{mas}$ and P.A.$=5°$ at $8.4\,\mathrm{GHz}$ up to a distance of $\sim 30\,\mathrm{mas}$ from the core. Moreover, they found an additional component, approximately $4\,\mathrm{mas}$ away from the core, without significant motion. With these measurements, they estimated the jet inclination angle θ to the line of sight to be 50–$80°$ (cf. Eq. 3.21). Combined *Chandra* and VLA observations by Hardcastle et al. (2003) showed subluminal motions of $\sim 0.5c$ on arcsec scales within the inner $100\,\mathrm{pc}$ leading to $\theta \sim 15°$. Hence, if these are really the bulk speeds, this would imply an acceleration from sub-parsec scale to a few 100 pc. Tingay et al. (1998) pointed out that some individual jet components show a short-time variability which can be explained by a higher apparent speed of $\sim 0.45c$. Thus, it is possible that the measured parsec-scale motion does not represent the underlying jet flow.

With the help of overlay images, different jet speeds (assuming a steady homogeneous jet flow) can be tested by displacing two epochs with respect to each other according to a certain angular motion. A comparison of three different possible apparent speeds is presented in Fig. A.7. The visual comparison of the space-VLBI image by Horiuchi et al. (2006) and the 3$^{\mathrm{rd}}$ epoch TANAMI image (Fig. 5.7) suggests an apparent speed much less than the one determined by Tingay et al. (2001) due to the astonishing similarity of both images. Therefore, the first column of Fig. A.7 assumes a negligible overall motion, thus $v_{\mathrm{app}} \sim 0\,\mathrm{mas}$. The jet knot at $\sim 3.5\,\mathrm{mas}$ shows no positional change with time, the core-component separation stays constant between November 2007 and September 2009. Within the uncertainties due to different angular resolutions, this is consistent with the result by Tingay et al. (2001)

Andrew S. Richers (RISE student) and Moritz Böck.
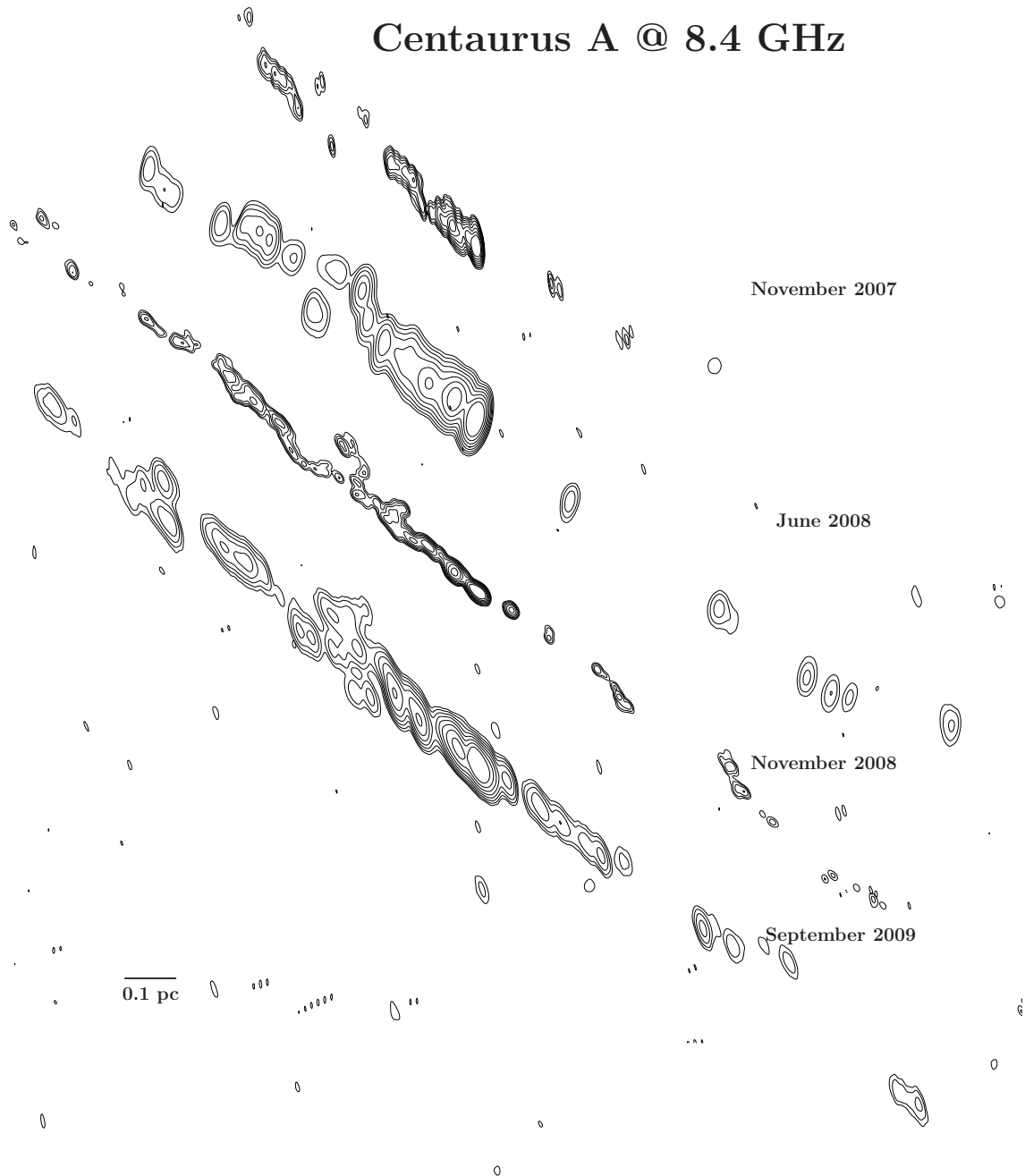
Figure 5.23: Composition of all 8.4 GHz TANAMI epochs of Centaurus A with the relative phase reference positions as base line. The lowest contours denote the 3σ-noise-level.

confirming the presence of a stationary jet feature at $\sim$4 mas downstream from the core. Moreover, the broadend, low luminosity region at about 20 mas to 25 mas, where the jet flow expands and recollimates subsequently, seems to be stationary, agreeing with the very similar broad feature seen in the space-VLBI image of August 2000 (Horiuchi et al., 2006) at the
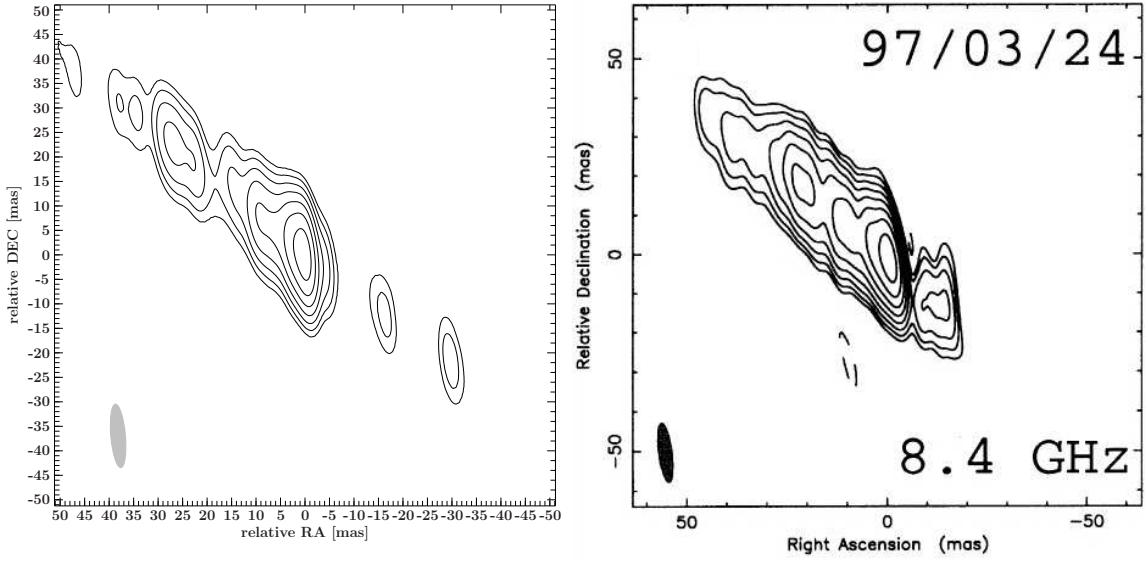
Figure 5.24: Left: The highest resolved 8.4 GHz TANAMI image of Cen A (3$^{\text{rd}}$ epoch, cf. Fig. 5.7) restored with a beam of (3×13) mas, P.A.=5° (represented by the gray ellipse in the lower left corner) and lower sensitivity (according to Tingay et al., 2001). This demonstrates the effect of smearing out the jet fine structure to a few separable broad jet knots ending up with about three distinct jet features. Right: For comparison, an example of the 8 GHz observation by Tingay et al. (2001).

same distance from the core. The overlaid images in the second column test the results by Tingay et al. (1998), assuming an apparent motion of $1.7^{+0.5}_{-0.2}$ mas yr^{-1} for the continuous jet flow. Tingay et al. (1998) and Tingay et al. (2001) only analyzed the angular separation of two separable components giving this mean subluminal speed. To adopt this, one has to take into account, that the angular resolution between these former VLBI measurements and the TANAMI observations differs by about one order of magnitude. Restoring the highest resolved 8.4 GHz TANAMI image (3$^{\text{rd}}$ epoch) with a beam of (3×13) mas, P.A.=5° of the VLBA array (cf. Tingay et al., 2001), only the most significant emission features remain distinguishable in the resulting image (see Fig. 5.24). This smeared-out view ends up with comparable structure information like in the images by Tingay et al. (1998) losing the fine-scale structure. In principle, the core feature and the major emission zones downstream before and after the jet widening are still clearly separable. Therefore, the former speed determination has to be treated with caution. With the higher resolved TANAMI images a more accurate speed determination can be made considering especially heterogeneously behaving features. In principle, a comparison to check this speed can be made by considering only the brightest jet features in order to avoid an overinterpretation based on the low resolution information. Figure A.7 (column 2) clearly shows that former speed determination represent the TANAMI data only when assuming a very simple (or low resolved) view, i.e., regarding only the significant and brightest features like in Fig. 5.24. The true nature of the Cen A jet flow is far more complicated and cannot be represented by an averaged continuous apparent motion for each resolved emission feature.

Figure 5.25: Linear regression to the separation of the second bright component besides the core of every 8 GHz epoch.This jet feature has no significant angular motion ($\sim 0.074\,\mathrm{mas\,yr^{-1}}$) and is therefore treated as a stationary jet component, labeled as $\mathrm{J_{stat}}$.
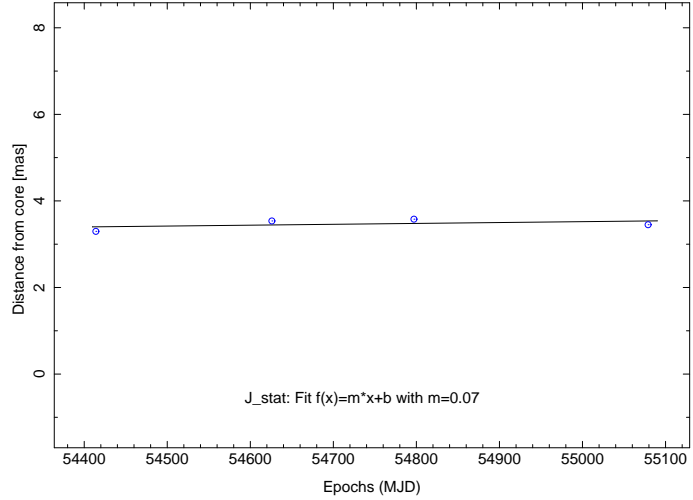
In the third column of Fig. A.7 the displacements according to the determined averaged speed ($\sim 2.7\,\mathrm{mas\,yr^{-1}}$) from the TANAMI measurements are presented. The Gaussian model components found for each epoch represent the main emission zones of the bright jet features or knots. Their position with respect to the core were used to determine the proper motion of the jet flow assuming ballistic motion and a stationary core. For the kinematic analysis the `modelfits` presented in Sect. 5.3 were applied and compared. To find an overall apparent jet speed the individual jet components of the four 8 GHz observations were tracked with time. Figure 5.26 shows the time dependent separation for each Gaussian component from the reference position of each image which was chosen to be the base line. In order to determine an overall speed for the jet flow, respective components at every epoch need to be identified at first. As already mentioned, two characteristic features besides the core can be definitely detected at all four 8 GHz epochs: the second bright component at $\sim$3.5 mas and a feature with increasing brightness after the jet widening at $\sim$23 mas. These jet structures were used as reference points for the cross identifications of components at every epoch. One should keep in mind that the position of the core can vary and, thus, the reference position is also affected by a certain positional error.

For the very significant feature at $\sim$3.5 mas at all 8 GHz epochs and also in the 22 GHz image (cf. Sect. 5.4), an unweighted linear least square fit obtaining a separation from the core with $\sim 0.074\,\mathrm{mas\,yr^{-1}}$ confirmed the previously proposed stationary behaviour of this component (see Fig. 5.25). In the following this component is named $\mathrm{J_{stat}}$ according to the results of the fit. The `modelfit` components determined in Sect. 5.3 were then identified and labeled. Unweighted linear least squares fits were applied in order to get the apparent speed of each individual component and the overall averaged motion, respectively. The fit results[7] for the individual apparent speeds are shown in Fig. A.8 and Table 5.3 with the component labels registered in Table A.1 to A.4. In total, eight individual jet components can be identified and tracked. This gives an overall mean apparent speed of $v = 2.7\,\mathrm{mas\,yr^{-1}}$ corresponding to $v = 0.158c$. For determining this averaged velocity, the stationary component $\mathrm{J_{stat}}$ and the components between J6 and J5, displaying the emission

---

[7]Only the absolute positions without error bars were considered due to the lack of uncertainty estimation within `DIFMAP`.

region of the jet widening, were excluded. As discussed in Sect. 5.2, the broadend region is in fact a reliable feature observable in every 8 GHz TANAMI image. However, the emission is widely spread and thus, the positions of the Gaussian model components fitted to the visibility data by the `modelfit` algorithm contains large uncertainties. Together with the preliminary considerations refering to the overlay plots in Fig. A.7, this jet widening shows also no remarkable angular motion. Comparing this to the image by Horiuchi et al. (2006), this disturbance of the jet flow and collimation might be stationary as well. A summary of the jet kinematic fits are given in Fig. 5.26 showing all associations of individual components and their core separation with time giving an overall jet flow motion.

It is worth noting that the resulting mean speed of $2.7\,\mathrm{mas\,yr^{-1}}$ cannot be taken as the representative underlying velocity of a steady flowing jet, since the values of the resulting linear fits scatter from $\sim 0.3\,\mathrm{mas\,yr^{-1}}$ to $5.6\,\mathrm{mas\,yr^{-1}}$ for all components. For the components detected in all four epochs (see Table 5.3), the speeds scatter only from $\sim 1\,\mathrm{mas\,yr^{-1}}$ to $4\,\mathrm{mas\,yr^{-1}}$, with J4 being the fastest component. This highlights the strong variety in motion within the jet making it difficult to state a single apparent jet speed corresponding to a steady plasma flow. From Fig. 5.26, it is also very obvious that the subparsec scale jet of Cen A exhibits a very complex kinematic behaviour. Besides the definitive stationary component J_{stat}, also the components J8, J7 and J2 show no significant angular motion (Fig. A.8). Excluding J2, the linear least square fits for J1 to J6 give a mean of $3.82\,\mathrm{mas\,yr^{-1}}$, corresponding to a subluminal movement of $v = 0.22c$ while passing, e.g., an obstacle at $\sim23\,\mathrm{mas}$ which is observed as a standing, diffuse emission feature. The flux density evolution of the individual components with time constrains this result (see Fig. A.9 and Sect. 5.6 for more details). While moving downstream, the flux density of each component decreases. Thus, this can also be used for the cross-epoch-identification. To summarize the kinematic analysis, Fig. 5.27 combines all four 8 GHz TANAMI epochs of the subparsec Cen A jet with overlaid and labeled Gaussian model components.

Name of model component	# of epochs detected	fitted v_{apparent} [mas yr^{-1}]
J_{stat}	4	0.07
J8	4	0.94
J7	4	1.24
J6	4	3.77
J5	4	3.25
J4	4	4.07
J3	2	3.24
J2	3	0.23
J1	2	5.66

Table 5.3: Linear regression results for the speed of individual jet components. The corresponding plots are shown in Fig. A.8.
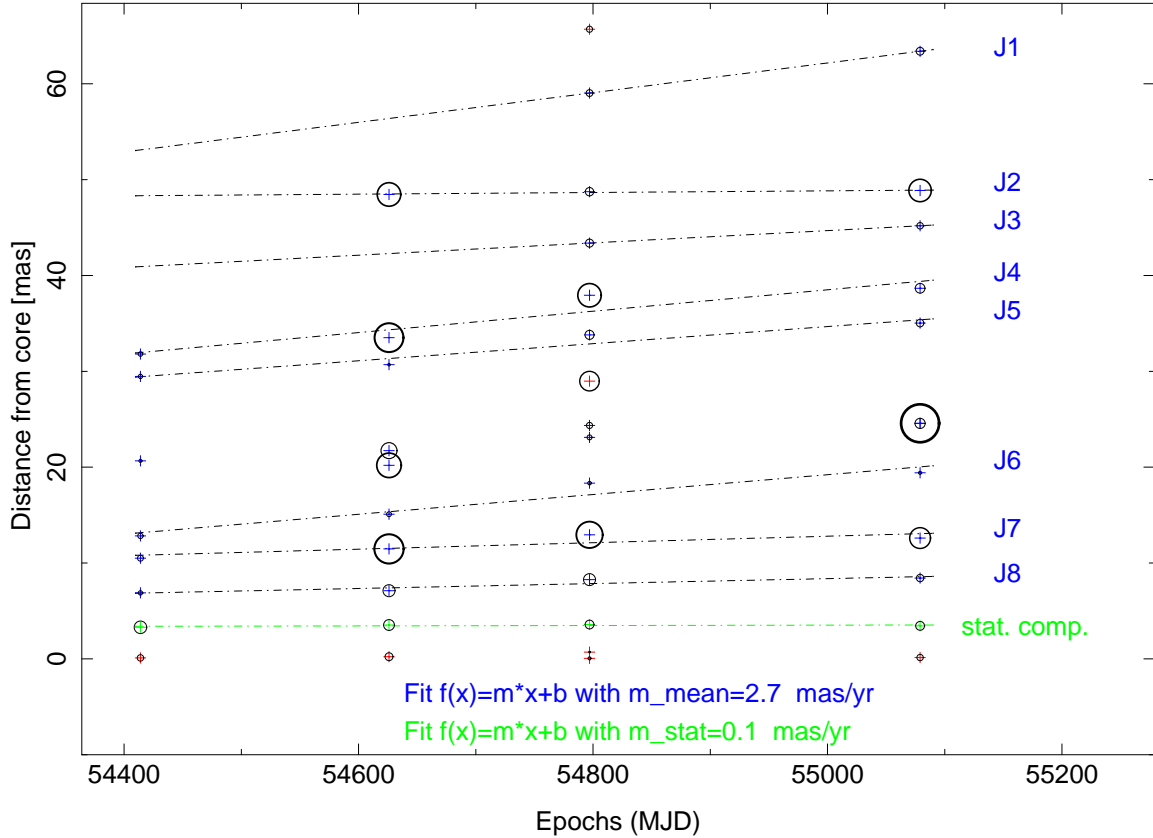
Figure 5.26: Time dependent evolution of the Cen A jet components at all four 8 GHz TANAMI epochs. The unweighted linear least squares fits (with $f(x) = m \cdot x + b$) to the associated components are shown, excluding the Gaussian model components displaying the emission of the broadend emission region at $\sim 23 \pm 4$ mas. The linear least squares fit for the stationary component J_{stat} next to the core gives $m_{stat} = 0.1 \, \mathrm{mas} \, \mathrm{yr}^{-1}$ (shown in green). The circles represent the FWHM of the Gaussian model components. The mean angular motion obtained is $m_{mean} = 2.7 \, \mathrm{mas} \, \mathrm{yr}^{-1}$ corresponding to the assumption of a continuously and uniformly flowing jet plasma. Red crosses denote the central positions of the Gaussian components which are not taken into account for determining angular motions, i.e., especially the component in the 3rd epoch image at 28.9 mas has no counterpart in the previous and the following epochs.

Centaurus A @ 8.4 GHz
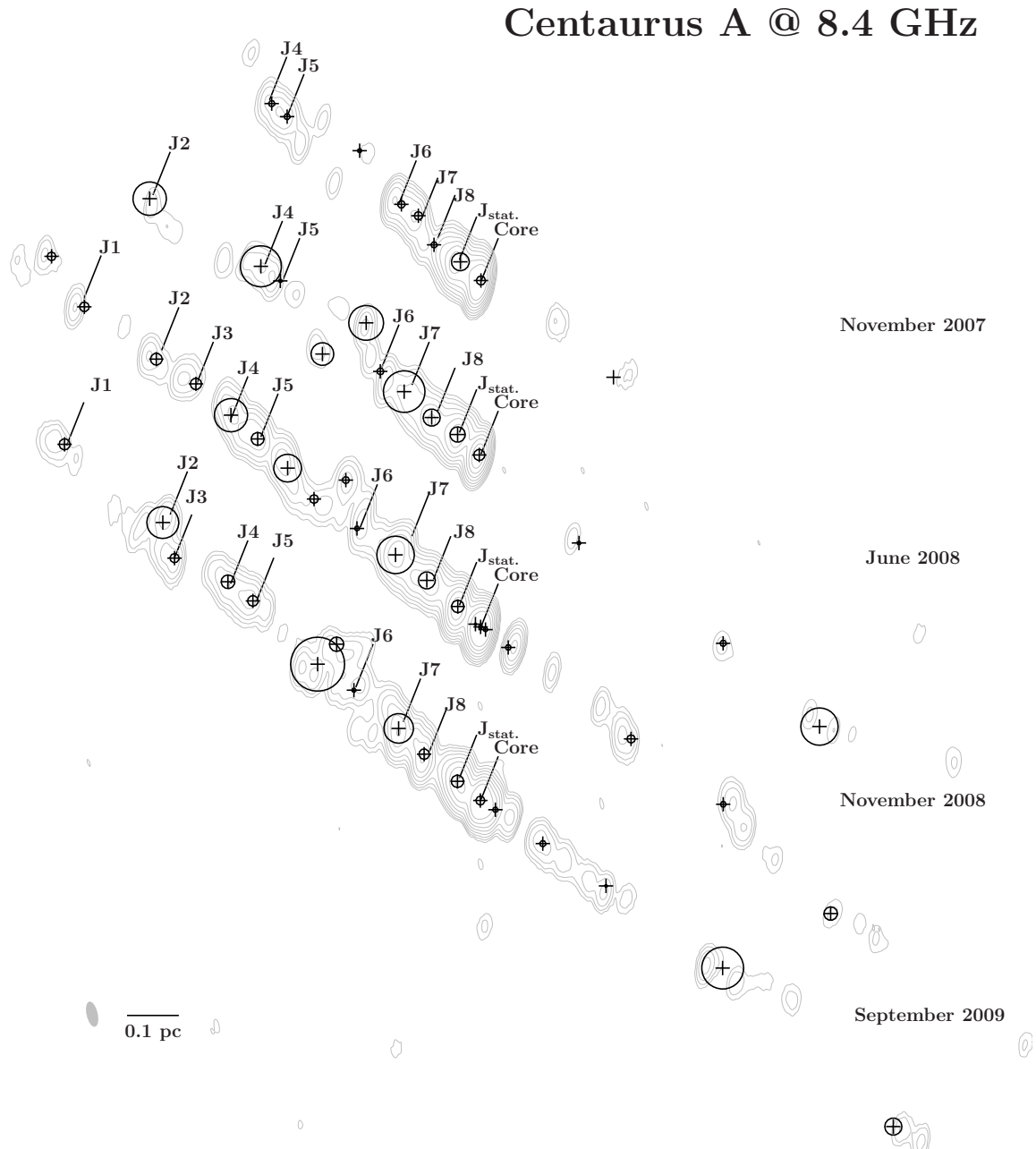
Figure 5.27: Result of the kinematic analysis using Gaussian model components for all
four 8.4 GHz TANAMI epochs of Cen A. Shown are the `clean` images (gray) restored
with with a common beam of (2.86×1.16) mas at a P.A.$=-13°$ (presented by the gray
ellipse in the lower left corner) and the relative phase reference positions as base line.
The Gaussian model components (with the corresponding FWHM) are overlaid (black)
and named according to the kinematic analysis.

5.6 Brightness temperature distribution

In this section, the brightness temperature distribution of the individual Gaussian model components for all observation epochs is discussed. In Sect. 4.1.1 the quantity T_{B} was already introduced (see Eq. 4.6), which gives the emission strength of a regional source within the jet normalized by its area. In the case of Gaussian model components as emission features, this corresponds to the particular flux density and the apparent diameter at half maximum (FWHM for a circular Gaussian), respectively. It is a measure to characterize the flux density distribution along the jet taking into account the angular extend of the individual emission zones. For non-thermal emission, the brightness temperature is frequency dependent with $T_{\mathrm{B}} \propto \nu^{-2}$.

In general, due to the expansion of the jet while the plasma is moving outwards, a steady decline of T_{B} downstream is expected. The flux density decreases while the sizes of the emission regions increase (e.g., Königl, 1981). Furthermore, considering one individual outwards moving component, both the flux density S and the brightness temperature T_{B} should decrease with time. In Fig. A.10 and A.9, the time dependent evolution of S and T_{B} of all fitted and tracked Gaussian model components of all 8 GHz epochs, respectively, is shown. For J1, J2, J3, and J6 both, the flux density and T_{B} show this expected behaviour. The stationary component J_{stat} shows a steady decline in flux density (cf. Fig. 5.11) while the brightness temperature drops only slightly. The components J8 and J7, which have no significant apparent motion (cf. Fig. A.8) compared to the outer model components, show only a small variability in flux density. Excluding the 1st epoch yields to almost no time dependence of T_{B} for both components. This exclusion is feasible since the `modelfit` for this epoch is comparably simple (see Table A.1. The evolution in S and T_{B} of J5 and J4 is consistent with the theoretical predictions as long as special care is taken for the 2nd epoch. As discussed in Sect. 5.2.2, the second VLBI data set suffered from a failure of the Parkes antenna and therefore these data are less reliable. The emission region represented by J5 and J4 in this 2nd epoch image, is modeled by two Gaussian components, but the fit reveals a high uncertainty in the flux distribution of both components. The low flux density and T_{B} of J5 and J4 in the 1st epoch data set can be explained by being the ending of the jet, partially resolved by the array.

A comparison of T_{B} evolving along the jet with time is reasonable to get information about jet expansion and collimation. Figure 5.28 shows the brightness temperature distribution as a function of distance from the core for all four 8 GHz epochs. Overall, the distribution of the Gaussian model components of all data sets are comparable showing a flat T_{B} behaviour for the inner $\sim$20 mas and a decline of T_{B} after the broadend jet region. For the highly resolved and confident 3rd 8 GHz data set, the outer jet components (i.e., those after the broadend jet region) were fitted with a linear function $\log(T_{\mathrm{B}}) \propto s \cdot \log(R)$ giving a slope of $s \approx -1.67$. This result can also be checked by comparing related components of the quasi-simultaneous, dual-frequency visibility data of November 2008 (Fig. 5.29) giving a slope of $s(22\,\mathrm{GHz}) = -2.04$. The frequency dependence of $T_{\mathrm{B}} \propto \nu^{-2}$ can be clearly seen in the offset between the 8 GHz and 22 GHz brightness temperatures. Moreover, it seems that this relation reflects the collimation-broadening-recollimation behaviour visible in the images since the decrease of T_{B} along the 8 GHz jet is very similar before and after the dis-
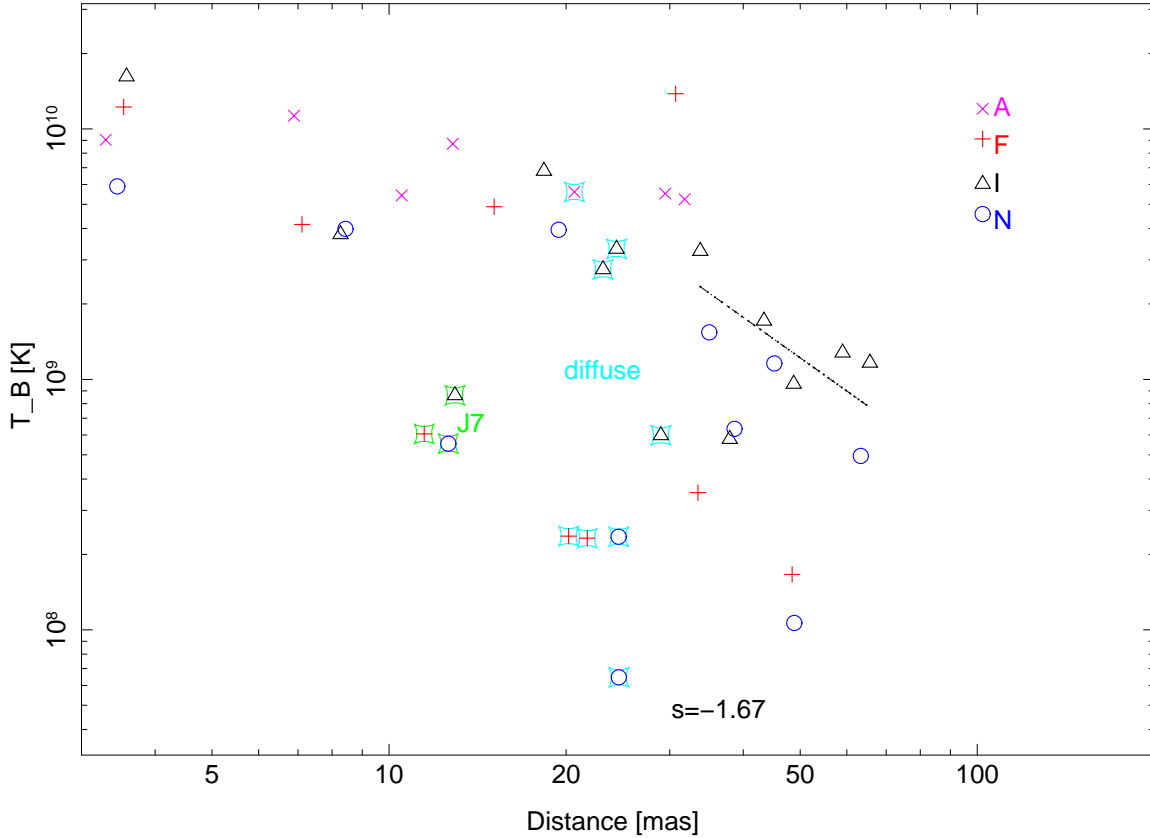
Figure 5.28: Brightness-temperature distribution of individual components along the jet for all four 8.4 GHz epochs. In general, the behaviour of all epochs is comparable with a nearly constant T_B for the inner ~ 20 mas and a decline of T_B after the broadend jet region. In particular the T_B of J7 and of the components displaying the jet broadening are marked in green and light blue, respectively, since both features show a divergence compared to the overall T_B distribution along the jet representable by a linear function $\log(T_B) \propto s \cdot \log(R)$ with $s \approx -1.67$.

turbance. The sizes of the modeled Gaussian components within the inner 20 mas increase with distance. This is consistent with the expectations of an expanding jet (Fig. 5.19).

Kadler (2005) discusses a basic model for the brightness temperature distribution in parsec-scale radio jets assuming that the jet diameter d, the magnetic field B, and the particle density n are functions of the distance R from the jet origin, all described by a powerlaw

$$d \propto R^l, \quad B \propto R^b, \quad n \propto R^n \quad . \tag{5.5}$$

This leads to

$$T_B \propto R^{l+n+b(1-\alpha)} \tag{5.6}$$

with the spectral index α (for more details, see, Kadler, 2005). For a sample of AGN with classical core-jet structure, the brightness temperature as a function of distance can be described by a powerlaw with a typical powerlaw-index $s = l + n + b(1-\alpha)$ of -1.5
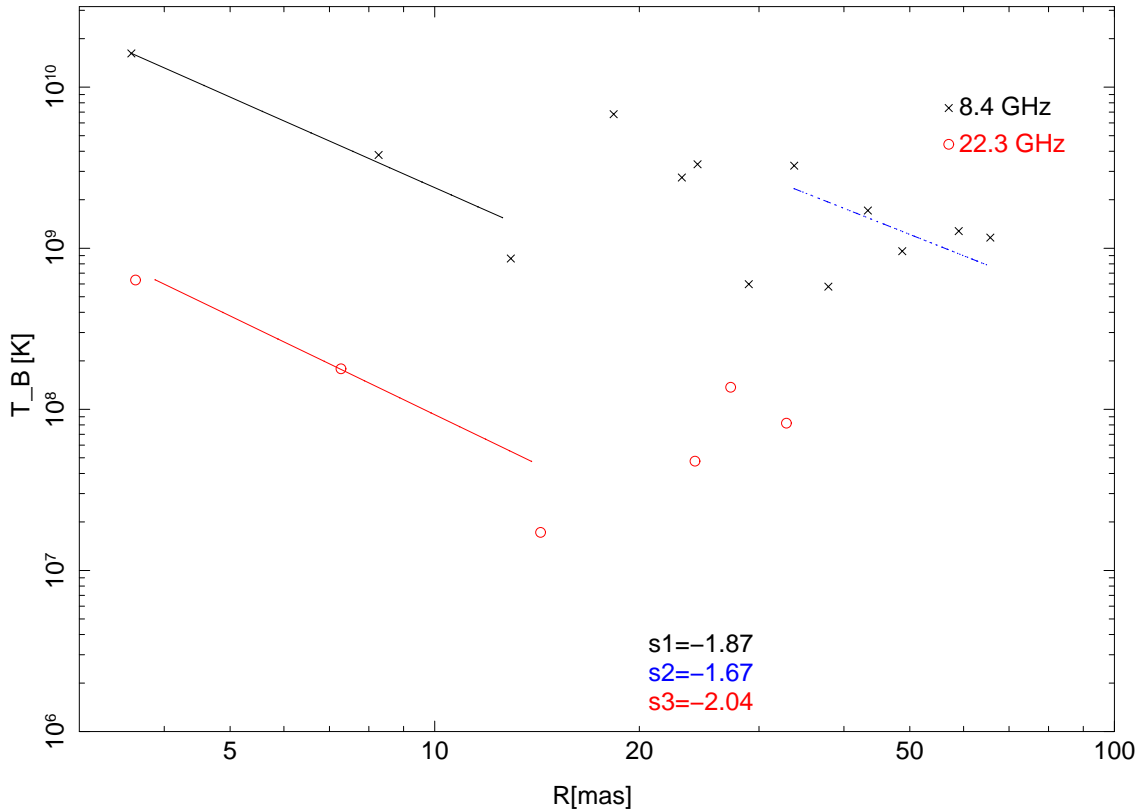
Figure 5.29: Brightness-temperature distribution of dual-frequency, quasi-simultaneous
observations in Nov. 2008. For the inner 20 mas a linear fit with $\log(T_{\mathrm{B}}) \propto s \cdot \log(R)$
obtains $s1(8\,\mathrm{GHz}) = -1.87$ (black) and $s3(22\,\mathrm{GHz}) = -2.04$ (red), comparable to the fit
of the outer parts of $s2(8\,\mathrm{GHz}) = -1.67$ (blue).

to -3. This can set constraints on the dependence of the magnetic field and the particle
density in well collimated and accelerating jets. Assuming conservation of particle flux and
magnetic energy along an accelerating jet, the measured brightness temperature gradient
of $s \sim -1.7$, implies for the Cen A jet a similar behaviour like AGN jets on parsec scales.

The $\log(T_{\mathrm{B}})$-$\log(R)$-relation seen in Figs. 5.28 and 5.29 supports the suggestion that the
component J7 behaves unexpectedly when assuming a continuous jet flow with downstream
decreasing brightness. The brightness temperature of this component drops by about one
magnitude while the previous and subsequent components show a steady behaviour. This
can be explained by the comparable large FWHM (see Tables A.2 to A.5), suggesting a
broad or even diffuse emission region. However, this significant and untypical decrease in
T_{B} besides the persistent performance of the overall jet might be an indicator for more
complicated underlying physical processes. The same accounts for the $\log(T_{\mathrm{B}})$-$\log(R)$-
relation of all components modeling the jet widening at $\sim$23 mas. This drop in brightness
temperature at 8 GHz and the synchronous brightening at 22 GHz is consistent with the
increase of emission at higher frequency discussed in Sect. 5.4. This might suggest the
presence of a stationary, absorbing feature resulting in the imaged concave and broadend
shape (see Chap. 6 for a more detailed discussion).

6 Discussion, conclusion and outlook

W^ITH VLBI techniques the central region of the closest active galaxy Centaurus A was observed at 8.4 GHz and 22.3 GHz and resolved down to scales of lightdays. The southern hemisphere VLBI array used by the TANAMI project achieves angular resolutions of milliarcseconds resulting in the so far highest resolved image of an AGN jet-counterjet system. Due to these exceptional observing conditions and the proximity of Cen A, the dual-frequency images reveal a highly collimated jet with a detailed substructure with a complex spectral and kinematical behaviour, offering valuable clues to the underlying physical situation. To conclude, I will give first an overall picture of the obtained results and, second, an outlook to further planned investigations.

6.1 Overall picture

The previous chapter presented the approaches which were undertaken in order to understand and interpret the high resolution radio data of Cen A's central region. The combined analysis of the five TANAMI observations of the inner Cen A jet at two frequencies provide an illuminating picture of an AGN jet. These VLBI measurements allow us to set up a physical model explaining the observed jet phenomena in Cen A based on the general view of the unification scheme (Sect. 2.2 and 3.4). In the following, the main obtained results are highlighted:

1. The dual-frequency VLBI images clearly resolve the innermost Cen A region into a jet-counterjet system. The jet at P.A.~50° shows distinctive structures at scales of ≤ 0.02 pc. In particular, the highly collimated jet flow within the inner ~50 mas is disturbed as it exhibits a broadend shape at a distance of ~23 mas from the core and recollimation corresponding to a significant drop and subsequent increase in flux density along the jet ridge line. Discrete components of the fainter counterjet at P.A.~180° are clearly detected, showing a slight displacement with respect to the jet axis.

2. Spectral analysis of the quasi-simultaneous dual-frequency images of Cen A results in a highly spatially resolved spectral-index map for Cen A. It shows a strongly absorbed core feature with $\alpha \geq 2$ explainable with synchrotron-self and free-free absorption. Moreover, the spectral index varies along the jet revealing further optically thick

regions without showing a simple steepening behaviour. These are indications for several production sites of high energetic photons besides the VLBI core. At the jet widening region at $\sim$23 mas, with a concave or hollow shape at 8 GHz, the 22 GHz image shows a bright compact component suggesting an absorbing feature.

3. On a baseline of nearly two years, the TANAMI observations of Cen A allow to determine an apparent jet speed of $v \sim 2.7\,\mathrm{mas\,yr^{-1}}$ corresponding to $v \sim 0.16c$ excluding the stationary component J_{stat} next to the core. However, due to differential motion of individual components, this speed determination cannot easily be interpreted as a representative overall jet flow. The fastest speed for the components detected in all four epochs is $v \sim 4\,\mathrm{mas\,yr^{-1}}$, obtained for the model component J4. Excluding all components without substantially reliable motion (see below), the mean jet speed ends up with $\sim$3.8 mas yr^{-1}, corresponding to a subluminal apparent speed of $v \sim 0.22c$.

4. The kinematic analysis gives evidence for stationary and slower moving features within the jet, respectively. The most prominent stationary component J_{stat} has a distance of $\sim$3.5 mas to the core. It is seen in all images and at both frequencies, having a flat to optically thin spectrum. Downstream, the following components J8 and J7 both show no significant motion either. In the spectral-index map, the region in between the jet components J_{stat} and J8 is characterized by an inverted spectrum indicating denser jet material seen along the line of sight.

5. For the highest resolved 8 GHz image of November 2008, the brightness temperature of the jet components (without the broadend region) decrease with the distance from the core following a slope of $s \sim -1.7$ in a $\log(T_{\mathrm{B}})$-$\log(R)$-plot giving information about the jet expansion, the particle density and the magnetic field along the jet. At 22 GHz, a consistent behaviour is seen.

6. The evolution of T_{B} for individual jet components over time reflects the complex kinematical behaviour. Especially the jet component J7 shows no variations in T_{B} with time. Moreover, together with the Gaussian model components representing the jet widening, these particular components do not fit into the overall $\log(T_{\mathrm{B}})$-$\log(R)$-relation. For the moving components a decline of T_{B} with time can be seen displaying the outwards flow with increasing jet opening. Obviously the behaviour of these special features represents other physical conditions.

7. The comparison of these high resolution images to former VLBI observations of Cen A by Tingay et al. (2001) and Horiuchi et al. (2006) allows to check the reliability of the obtained results. Due to high similarity, it is very likely that the overall jet structure, in particular the prominent features J_{stat} and the broadend jet disturbance, do not rapidly evolve with time.

According to the unified AGN model, the central region of Cen A is seen edge-on, i.e. the jet inclination angle is large while the accretion disk and the absorbing torus lie almost in the plane parallel to the line of sight. Hence, observing the central region, it is expected to see emission affected by absorption. The highly inverted spectral index towards the SMBH confirms this. Due to synchrotron-self absorption within the jet, the core feature is seen absorbed at lower frequencies. Free-free absorption by an obscuring dust torus may also explain the inversion of the spectrum towards the BH. Moreover, optically thick re-

gions can be indications for kinks or shocks within the jet. The spectral analysis combined with the complex kinematical behaviour suggests a turbulent jet flow strongly affected by such internal changes. The core and the stationary component J_{stat} can be interpreted as a standing shock or even a jet nozzle, recollimating the jet flow caused by imbalances between the jet plasma and the ambient medium (Daly & Marscher, 1988; Jorstad et al., 2001b). Subluminal moving jet knots are generally interpreted as moving shocks. Their ejection, i.e., their propagation through the core with coincident increase of radio brightness, may be associated with γ-ray flares (Lähteenmäki & Valtaoja, 2003; Jorstad et al., 2010; Marscher & Jorstad, 2010) assuming that the compression of jet plasma leads to the production of high energetic photons due to the SSC mechanism. Simultaneous multifrequency observations are needed to distinguish between external or internal SSC producing the high energy emission (e.g., Abdo et al., 2010c) and give information about the putative origin of cosmic rays (Abraham et al., 2007). The inspection of the spectral-index map of November 2008 reveals several jet regions besides the core having an optically thick appearance. This suggests that the origin of the γ-ray emission seen by *Fermi*/LAT can be localized also within the jet, e.g., within shocks.

The kinematic analysis gives a presumable underlying jet flow of $\sim 0.2c$ which is disturbed by a major feature at a distances of 20 mas to 25 mas from the core. It seems that the jet pierces through an obstacle which causes an expansion of the emitting material. Since the emission from the broadend region seems to have no apparent motion, it might be an external dusty feature in the line of sight absorbing the jet emission at lower frequencies. On the other hand, the concave emission seen at 8 GHz can be explained by an additional disturbance and possible compression of the outer jet layers by an obstacle partially blocking the flow path. In this case, the apparent recollimation further downstream would represent just the continuous, unaffected jet flow. This is consistent with the measured motion before and after the jet widening. Furthermore, the T_B behaviour of J6 can support this since it shows the expected flux density decrease for outwards moving components. According to this result, the disturbance might have its starting point closer to the core at the position of J7, while J6 displays the unaffected flow passing through.

The counterjet detection is trustworthy while the displacement from the jet axis needs further verification. This offset can be due to disturbances at the launching region of the jet. However, at larger scales, the Cen A jets show a diversly tilted structure (see Sect. 5.1.2) which might be due to bending or asymmetric behaviour on smaller scales. With a jet-to-counterjet surface brightness ratio (see Eq. 3.21) $R \sim 12$, an upper limit for the jet inclination angle of $\theta \sim 70°$ can be derived, assuming optically thin emission with $\alpha = -0.5$ and a maximum speed of $v = 1c$. Since subluminal apparent velocity is measured, this suggests that the jet points closer to the line of sight with an inclination angle of $\theta \leq 70°$.

To summarize, the TANAMI high resolution observations of Cen A give the most detailed view of an AGN jet ever achieved. The jet-counterjet system on sub-parsec scales is clearly detected showing individual features of particular nature distinguishable from the underlying plasma outflow. Cen A's jet seems to exhibit turbulent structures due to interaction with the ambient medium.
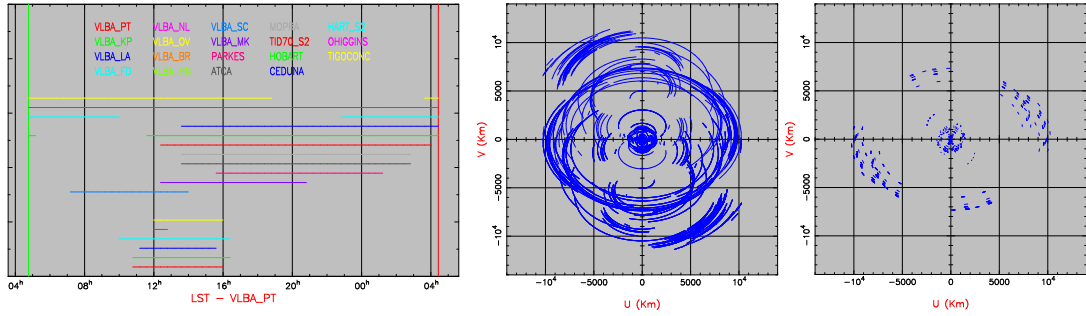
Figure 6.1: Combined VLBA-LBA observations. Left: uptime of all participating anten-
nas, middle: (u, v)-coverage for proposed global experiment, right: for comparison the
(u, v)-coverage of the highest fidelity image of Cen A at 8.4 GHz (3$^{\text{rd}}$ epoch)

6.2 Outlook

Further investigations are needed to gain more insight into the underlying physics of this
particular jet, to lead over to AGN in general and to test the unification model. Cen A
will be continuously monitored for the next 5 - 10 years in the framework of the TANAMI
program, which will regularly produce dual-frequency images of extragalactic jets through-
out the mission lifetime of *Fermi*, in order to study their multiwavelength behaviour. The
next succeeding 8 GHz observation of Cen A was undertaken in December 2009. Thus,
its analysis will give the chance to strengthen the results presented in this diploma thesis.
To manifest an overall jet speed, in general five epochs are needed at the minimum. The
same applies to the speed determination of the counterjet. It is expected that, at the
end of 2011, a basic and reliable velocity model will be set up. Based on this, e.g., the
inclination angle to the line of sight can be constrained which is currently only roughly
known ($50° − 80°$, Tingay et al., 1998). Combined dual-frequency epochs will give further
information about the radio-gamma-connection. Moreover, the TANAMI observations will
provide the radio part to quasi-simultaneous multifrequency measurements which try to
cover as much of the electromagnetic spectrum to construct time dependent SEDs. With
these, different emission mechanism models can be tested. Besides the regular TANAMI
observations, one big global VLBI project is going to be observed. Thanks to a success-
ful proposal (PI: C. Müller), passed to the Australia National Telescope Facility (ATNF)
asking for observing time for the LBA, after observing time for the VLBA antennas was
awarded through a Fermi cycle 3 proposal, these two VLBI arrays are going to be combined
for one multifrequency observation. Cen A will be observed at 2.3, 5.0, 8 and 22 GHz by
8 VLBA antennas, the LBA, and the antennas at Hartebeesthoek, TIGO and O'Higgins.
Figure 6.1 illustrates the on-source time of all telescopes and the resulting (u, v)-coverage
compared to the one of the high resolution 8 GHz image of November 2008. This global
observation will result in the highest fidelity image of an AGN jet ever made. The angular
resolution will increase only slightly but due to the extremely improved (u, v)-sampling, the
imaged structures are expected to be rich in trustworthy details. The main scientific goal of
these proposed observations is to measure the exact radio spectral shape of the candidate
sites for high energy emission identified within the work for this diploma thesis.

A Appendix

In the following, all additional tables and figures are presented which were referred in the text.

| Flux density | Radius | θ | b_{maj} | Axial ratio | P.A. | Name |
Jy	[mas]	[°]	[mas]	[°]		
0.022	18.94	-125.9	0	1	86.2	C
1.293	0.10	7.9	0.64	1	-130.2	Core
0.805	3.3	46.6	1.24	1	84.6	J$_{\mathrm{stat.}}$
0.123	6.9	52.2	0.43	1	36.9	J8
0.106	10.5	43.7	0.58	1	-133.8	J7
0.141	12.8	46.0	0.53	1	-19.7	J6
0.0301	20.7	42.9	0.30	1	-65.4	
0.058	29.5	49.7	0.43	1	-97.6	J5
0.060	31.8	49.7	0.45	1	9.5	J4

Table A.1: Model components for 1$^{\mathrm{st}}$ 8.4 GHz epoch of November 2007 ($\chi^2 = 6.7$); names according to Sec. 5.5, "C" labels counterjet components. Side note: The comparable high value of χ^2 can be explained by the underdetermined representation of the core feature by only one model component. A more extensive `modelfit` gives two nearly identical Gaussian components since the core feature is an elongated feature. However, for the kinematic analysis the simpler model was chosen for convenience reasons.

Flux density	Radius	θ	b_{maj}	Axial ratio	P.A.	Name
Jy	[mas]	[°]	[mas]	[°]		
0.039	35.59	−128.0	0.44	1	−57.9	C
0.059	50.32	−128.8	2.59	1	−111.8	C
0.042	15.31	−132.2	0.28	1	−13.3	C
1.33	0.22	115.8	0.78	1	50.8	Core
0.812	3.54	50.1	1.07	1	−72.2	$J_{\mathrm{stat.}}$
0.341	7.11	53.5	1.19	1	−132.6	J8
0.29	11.47	50.9	2.89	1	−122.7	J7
0.066	15.09	50.6	0.481	1	−143.8	J6
0.080	20.26	41.2	2.42	1	−133.3	
0.034	21.72	57.8	1.58	1	−23.5	
0.052	30.70	49.2	0.256	1	−120.5	J5
0.17	33.51	49.5	2.85	1	48.6	J4
0.052	48.45	52.4	2.32	1	59.2	J2

Table A.2: Model components for 2nd 8.4 GHz epoch of June 2008 ($\chi^2 = 0.49$); names according to Sect. 5.5, "C" labels counterjet components.

Flux density	Radius	θ	b_{maj}	Axial ratio	P.A.	Name
Jy	[mas]	[°]	[mas]	[°]		
0.038	52.37	-129.3	0.95	1	-95.0	C
0.028	86.39	-128.0	0.76	1	40.7	C
0.016	34.77	-126.2	0.41	1	-122.5	C
0.024	80.58	-126.6	0.79	1	-30.3	C
0.034	21.69	-126.8	0.58	1	0.0	C
0.060	3.95	-127.1	0.40	1	-83.4	C
0.493	0.61	-121.5	0.32	1	60.8	
0.772	0.05	105.9	0.30	1	65.5	Core
0.335	0.71	64.6	0.18	1	36.5	
0.706	3.58	48.8	0.87	1	75.7	$J_{\mathrm{stat.}}$
0.309	8.27	49.4	1.19	1	45.0	J8
0.339	12.94	49.9	2.61	1	70.5	J7
0.049	18.33	51.6	0.35	1	-24.6	J6
0.038	23.10	42.7	0.49	1	-18.4	
0.071	24.36	52.6	0.61	1	-82.9	
0.129	28.98	50.6	1.93	1	-54.0	
0.152	33.81	49.9	0.90	1	-66.4	J5
0.179	37.94	49.8	2.31	1	-30.3	J4
0.062	43.38	49.6	0.79	1	-68.2	J3
0.038	48.74	50.5	0.83	1	-70.0	J2
0.033	59.03	51.1	0.67	1	-68.6	J1
0.025	65.69	49.2	0.61	1	-116.0	

Table A.3: Model components for 3rd 8.4 GHz epoch of November 2008 ($\chi^2 = 0.67$); names according to Sect. 5.5, "C" labels counterjet components.

Flux density	Radius	θ	b_{maj}	Axial ratio	P.A.	Name
Jy	[mas]	[°]	[mas]	[°]		
0.013	60.95	-128.4	1.2	1	-15.3	C
0.023	34.12	-124.9	2.9	1	-124.4	C
0.022	17.59	-124.6	0.22	1	-17.4	C
0.018	8.79	-125.5	0.44	1	-42.1	C
0.138	2.04	-125.5	0.38	1	-136.9	C
0.641	0.14	145.8	0.63	1	-128.7	Core
0.260	3.45	52.2	0.87	1	-136.5	$J_{\mathrm{stat.}}$
0.124	8.43	51.4	0.73	1	102.8	J8
0.135	12.6	49.2	2.06	1	147.5	J7
0.022	19.42	49.3	0.31	1	-46.8	J6
0.053	24.58	50.4	3.75	1	49.9	
0.014	24.56	42.9	1.01	1	43.7	
0.050	35.03	49.0	0.75	1	-115.77	J5
0.034	38.67	49.3	0.96	1	-143.1	J4
0.028	45.19	51.8	0.64	1	2.05	J3
0.030	48.87	49.0	2.22	1	-40.6	J2
0.017	63.39	49.54	0.77	1	-126.9	J1

Table A.4: Model components for 4th 8.4 GHz epoch of September 2009 ($\chi^2 = 0.47$); names according to Sect. 5.5, "C" labels counterjet components.

Flux density	Radius	θ	b_{maj}	Axial ratio	P.A.	Name
Jy	[mas]	[°]	[mas]	[°]		
0.044	5.88	-133.8	0.79	1	9.9	C
1.620	0.25	-136.5	0.77	0.17	60.2	Core
0.809	0.92	54.2	0.59	0.87	-80.3	
0.314	2.42	48.9	0.40	1	-84.8	
0.192	3.88	49.5	0.86	1	-52.4	$J_{\mathrm{stat.}}$
0.257	7.53	49.4	1.88	1	-61.2	J8
0.099	14.56	49.1	3.77	1	-52.6	J7
0.0424	24.40	46.3	1.48	1	-113.8	
0.028	27.50	46.0	0.71	1	-77.7	
0.033	33.17	47.7	0.99	1	-25.0	J5

Table A.5: Model components for 22.3 GHz epoch of November 2008 ($\chi^2 = 0.31$); names according to Sect. 5.4 and 5.5, "C" labels counterjet components.
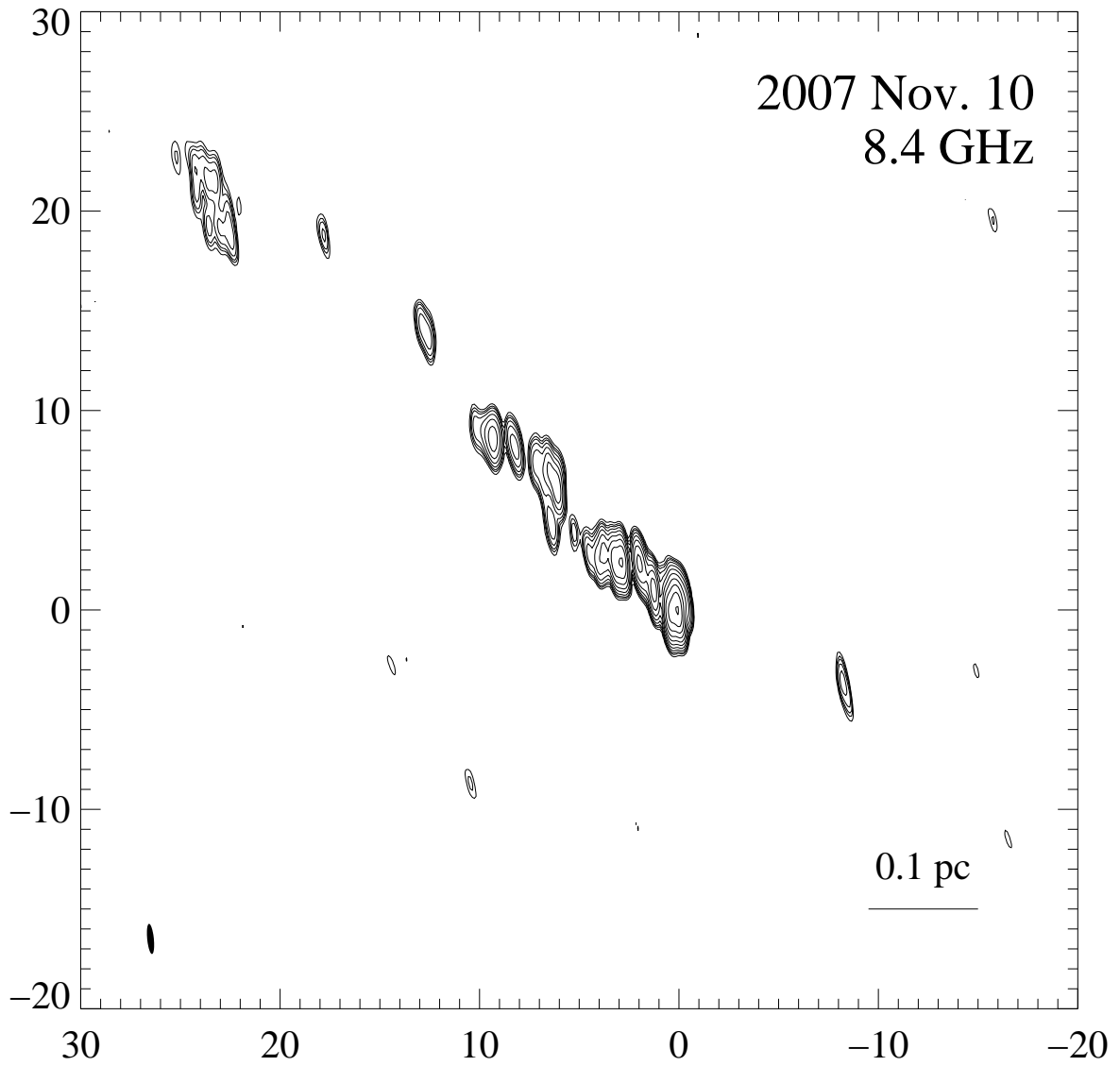
Figure A.1: 8.4 GHz image (of November 2007) with uniform weighting. The lowest contours denote the 3σ-noise-level. The image parameters are given in Table 5.2. The axes are in units of mas.
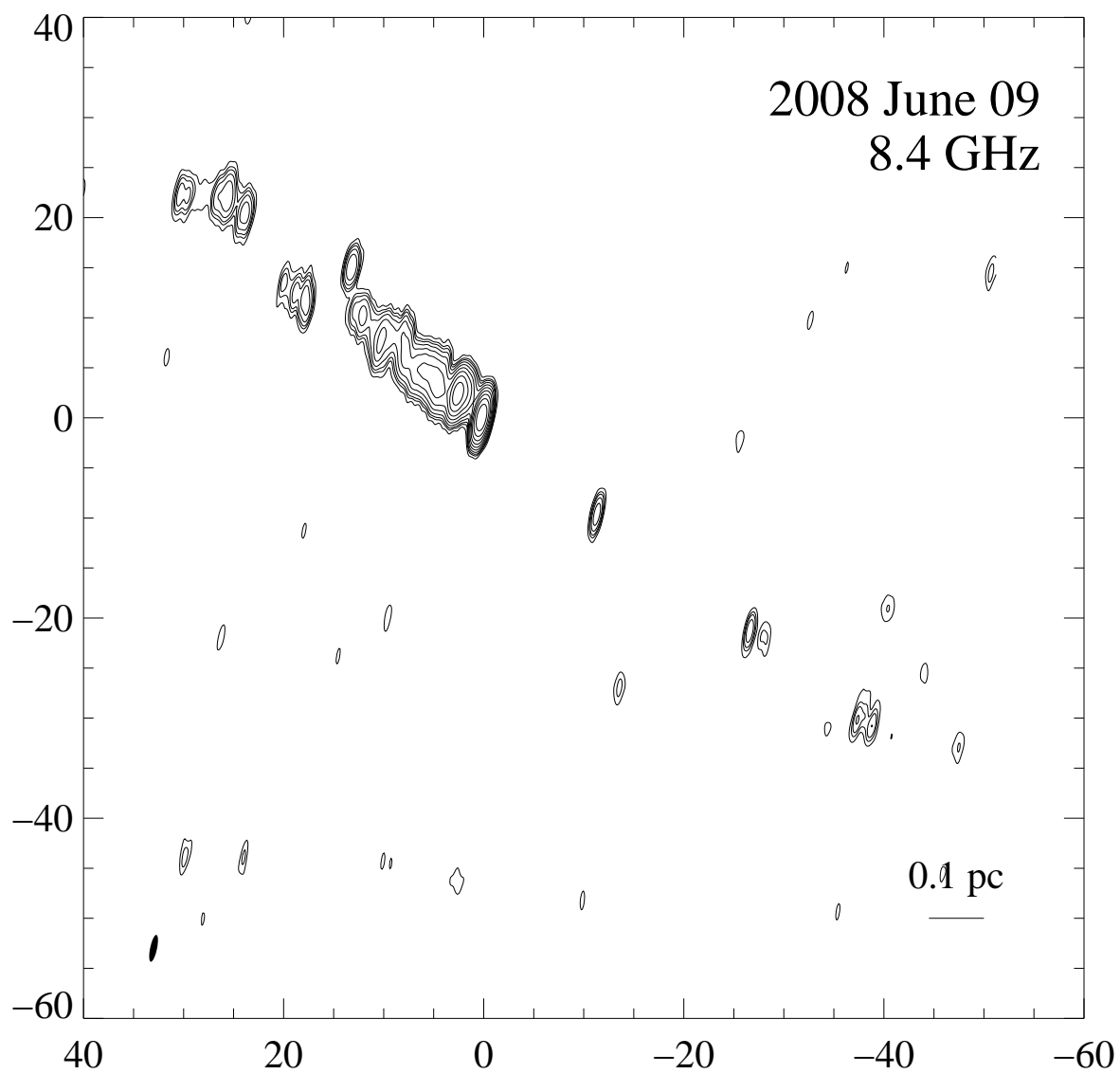
Figure A.2: 8.4 GHz image (of June 2008) with uniform weighting. The lowest contours denote the 3σ-noise-level. The image parameters are given in Table 5.2. The axes are in units of mas.
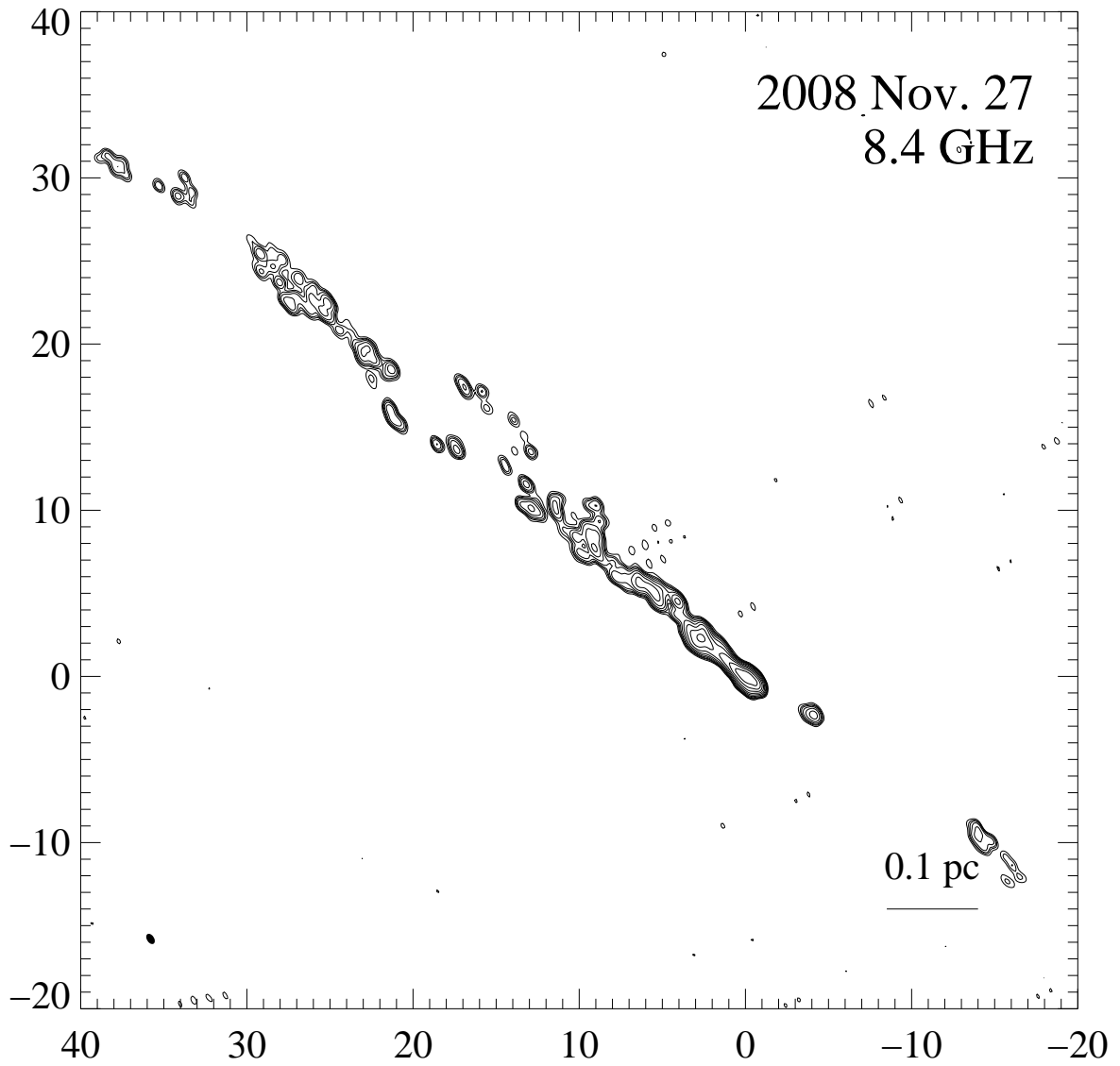
Figure A.3: 8.4 GHz image (of November 2008) with uniform weighting. The lowest contours denote the 3σ-noise-level. The image parameters are given in Table 5.2. The axes are in units of mas.
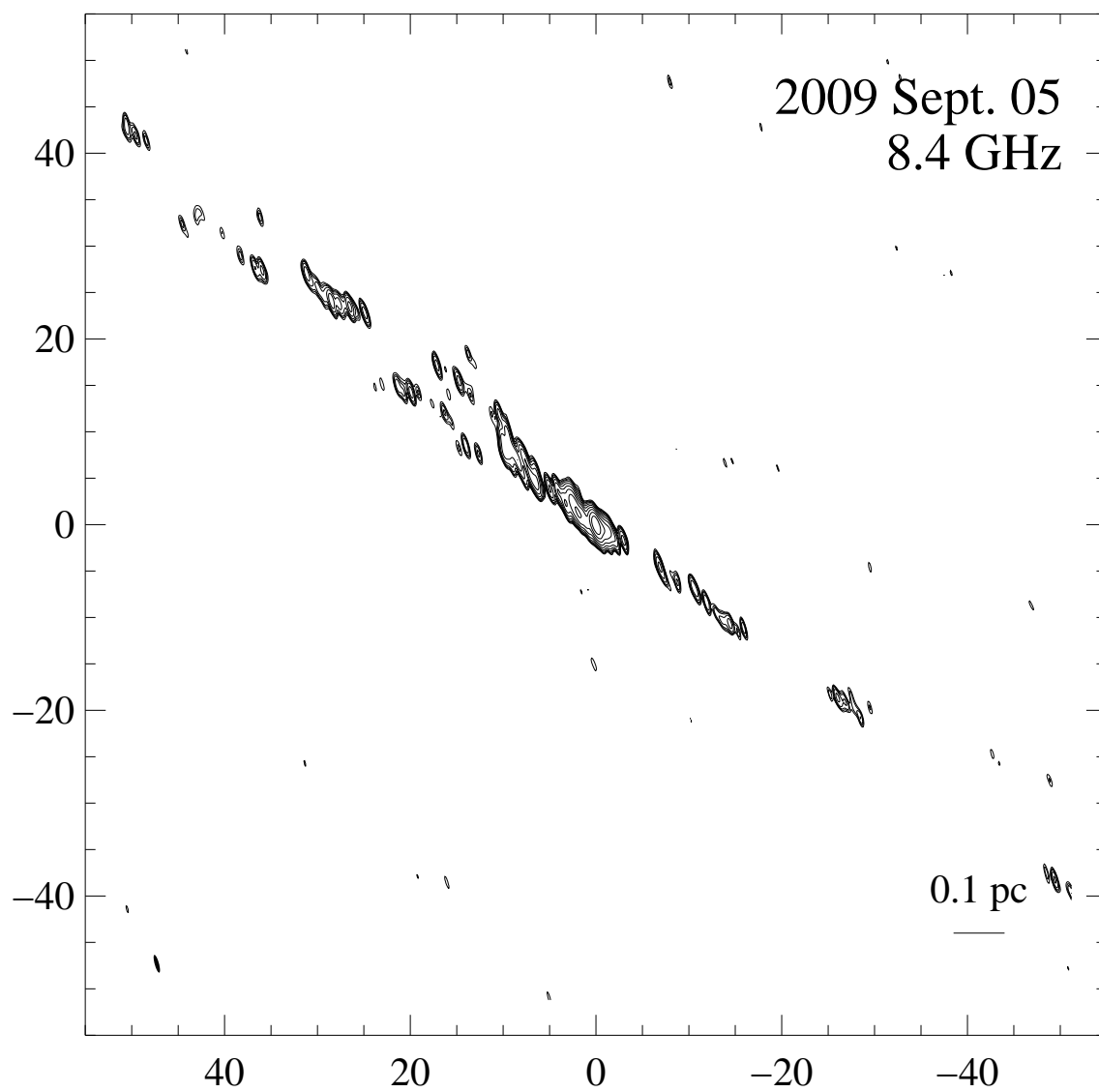
Figure A.4: 8.4 GHz image (of September 2009) with uniform weighting. The lowest contours denote the 3σ-noise-level. The image parameters are given in Table 5.2. The axes are in units of mas.
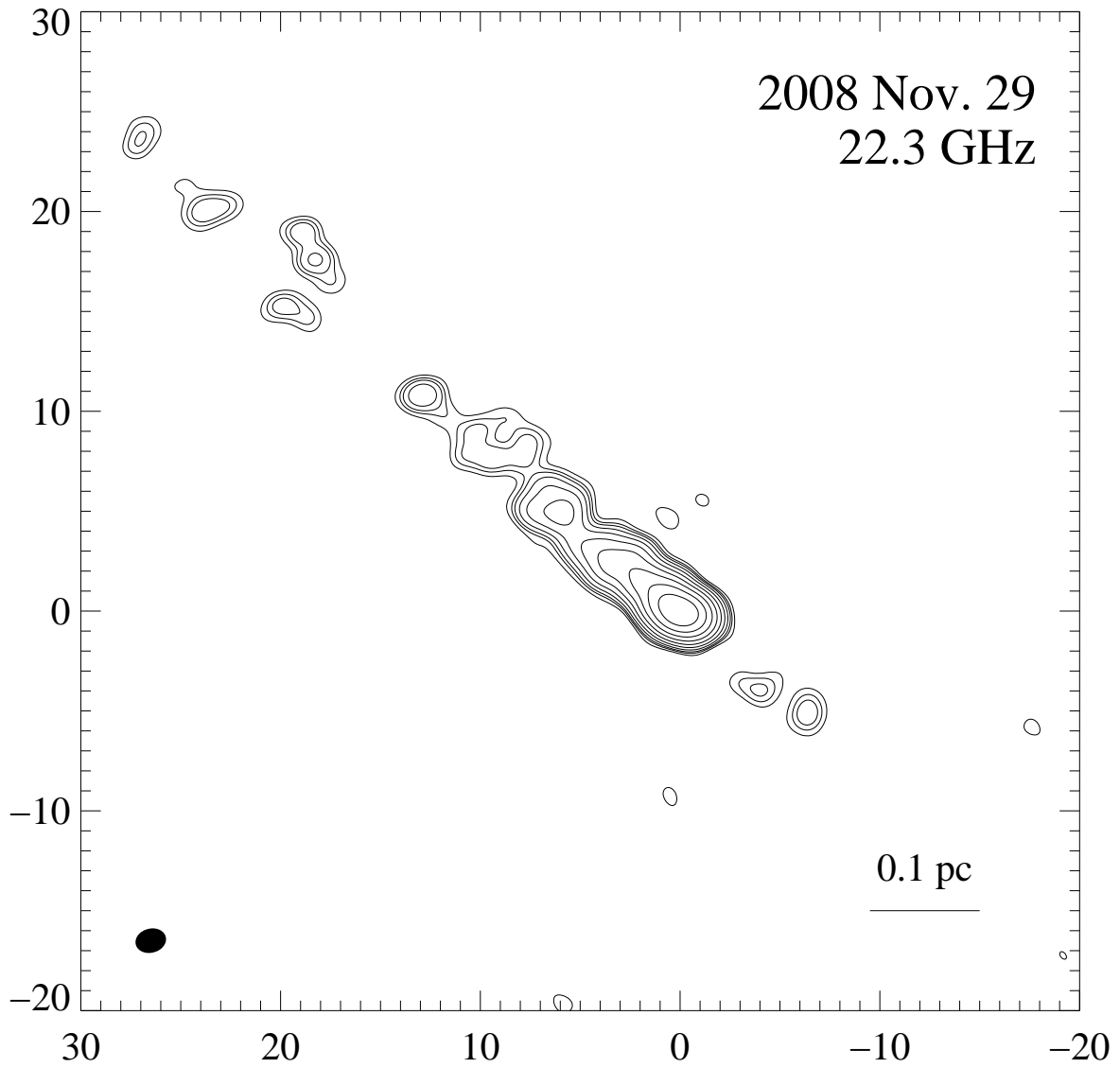
Figure A.5: 22.3 GHz image (of November 2008) with uniform weighting. The lowest contours denote the 3σ-noise-level. The image parameters are given in Table 5.2. The axes are in units of mas.
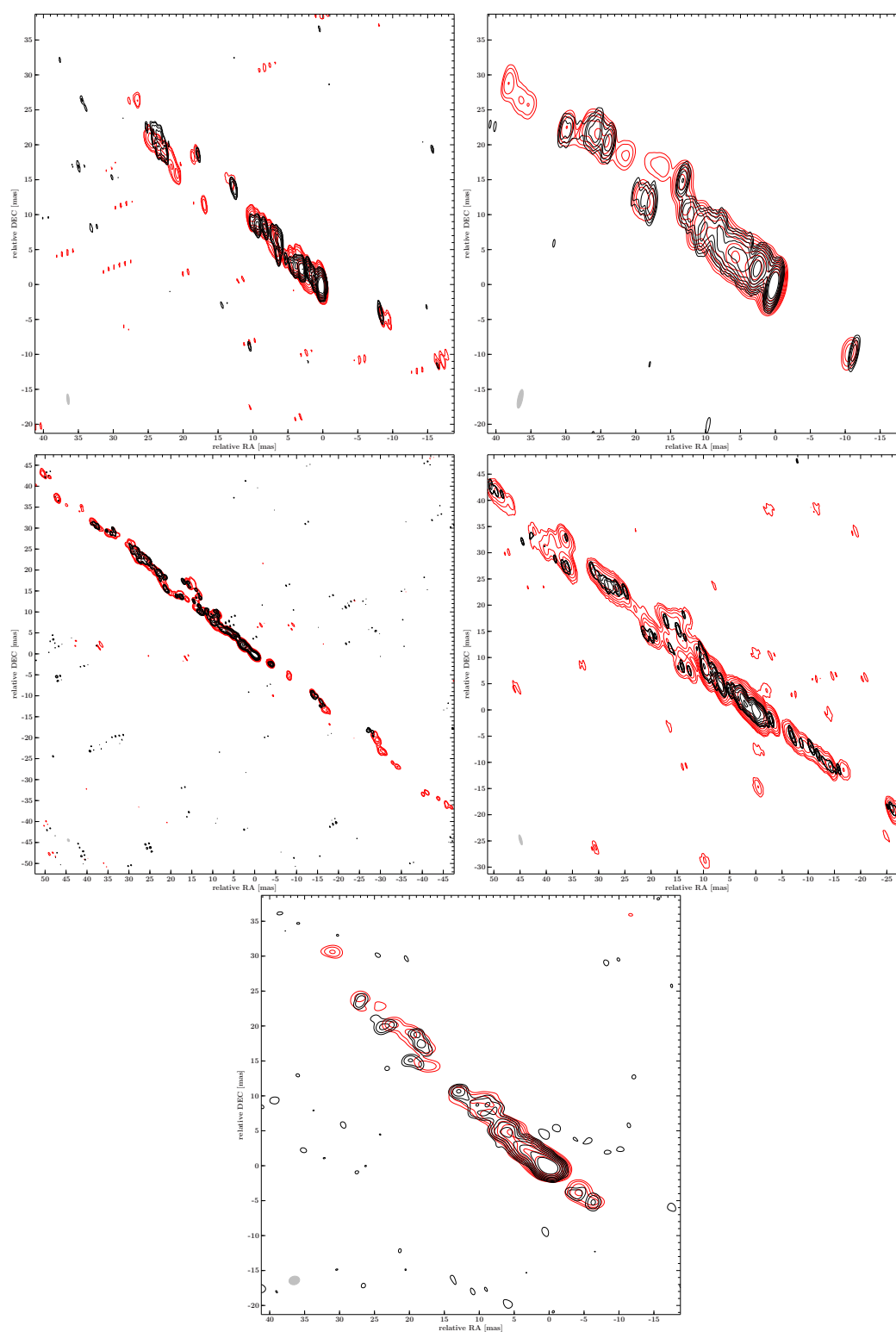
Figure A.6: Comparison via contour overlay of natural (red) and uniform (black) images (order: from top left to bottom: 8.4 GHz Nov. 2007, 8.4 GHz June 2008, 8.4 GHz Nov. 2008, 8.4 GHz Sept. 2009, 22.3 GHz Nov. 2008)
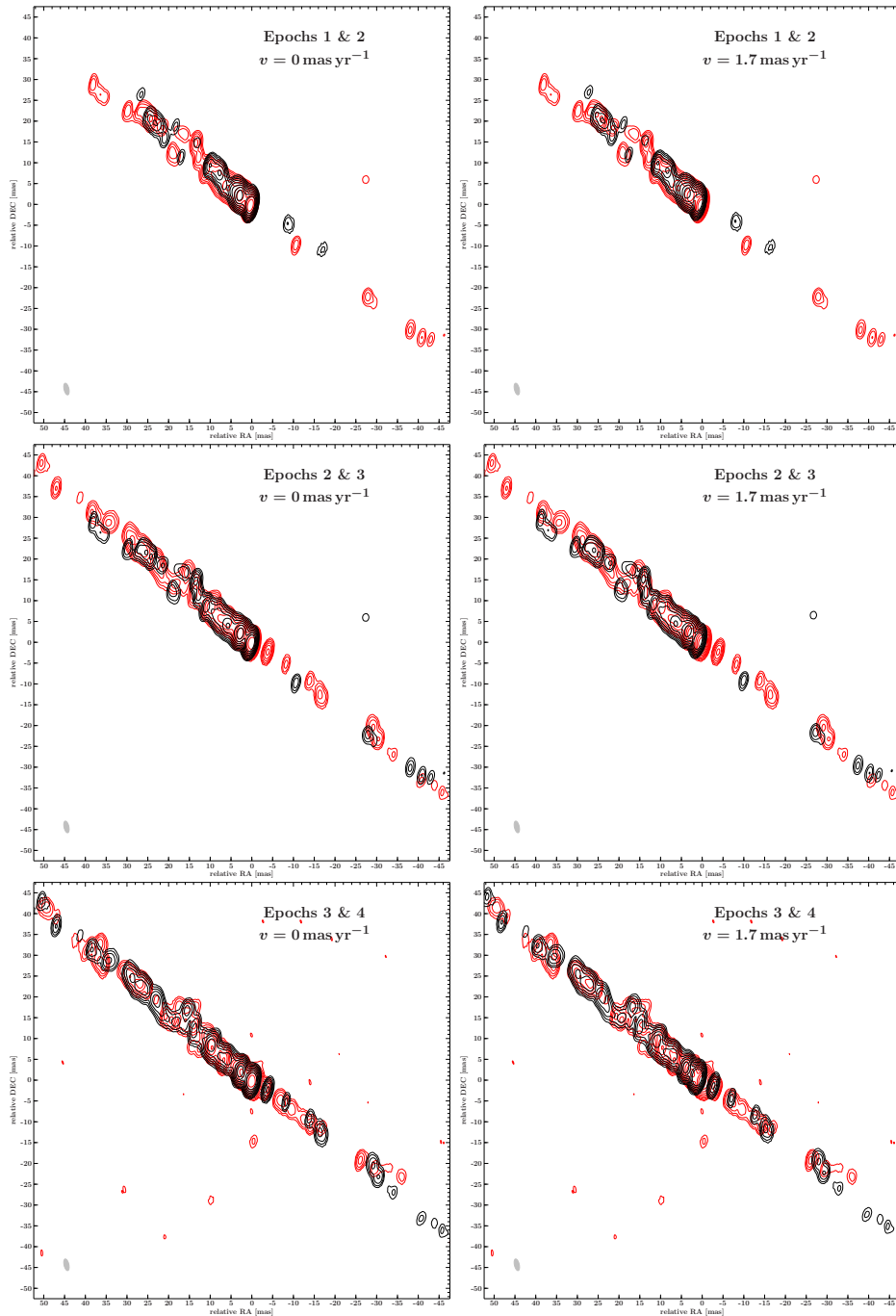
Figure A.7: Jet speed comparison. Rows: Comparison between two 8.4 GHz epochs respectively with the preceding epoch in black (from top to bottom: 1$^{\text{st}}$ & 2$^{\text{nd}}$, 2$^{\text{nd}}$ & 3$^{\text{nd}}$, 3$^{\text{rd}}$ & 4$^{\text{th}}$). Columns: 1. no motion $v = 0c$, 2. shift according to an angular motion with $v \sim 1.7\text{mas yr}^{-1} \approx 0.1c$ (Tingay et al., 1998), 3. shift according to an angular motion with $v \sim 2.7\text{mas yr}^{-1} \approx 0.155c$)
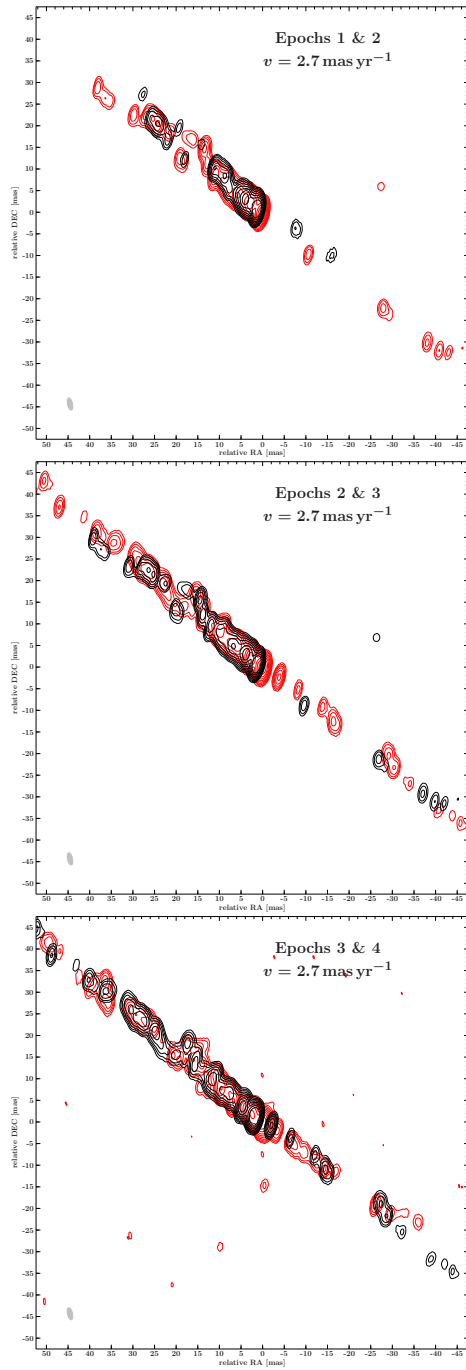
Figure A.7: Jet speed comparison (continued).Rows: Comparison between two 8.4 GHz epochs respectively with the preceding epoch in black (from top to bottom: 1st & 2nd, 2nd & 3nd, 3rd & 4th). Columns: 1. no motion $v = 0c$, 2. shift according to an angular motion with $v \sim 1.7\text{mas yr}^{-1} \approx 0.1c$ (Tingay et al., 1998), 3. shift according to an angular motion with $v \sim 2.7\text{mas yr}^{-1} \approx 0.155c$)
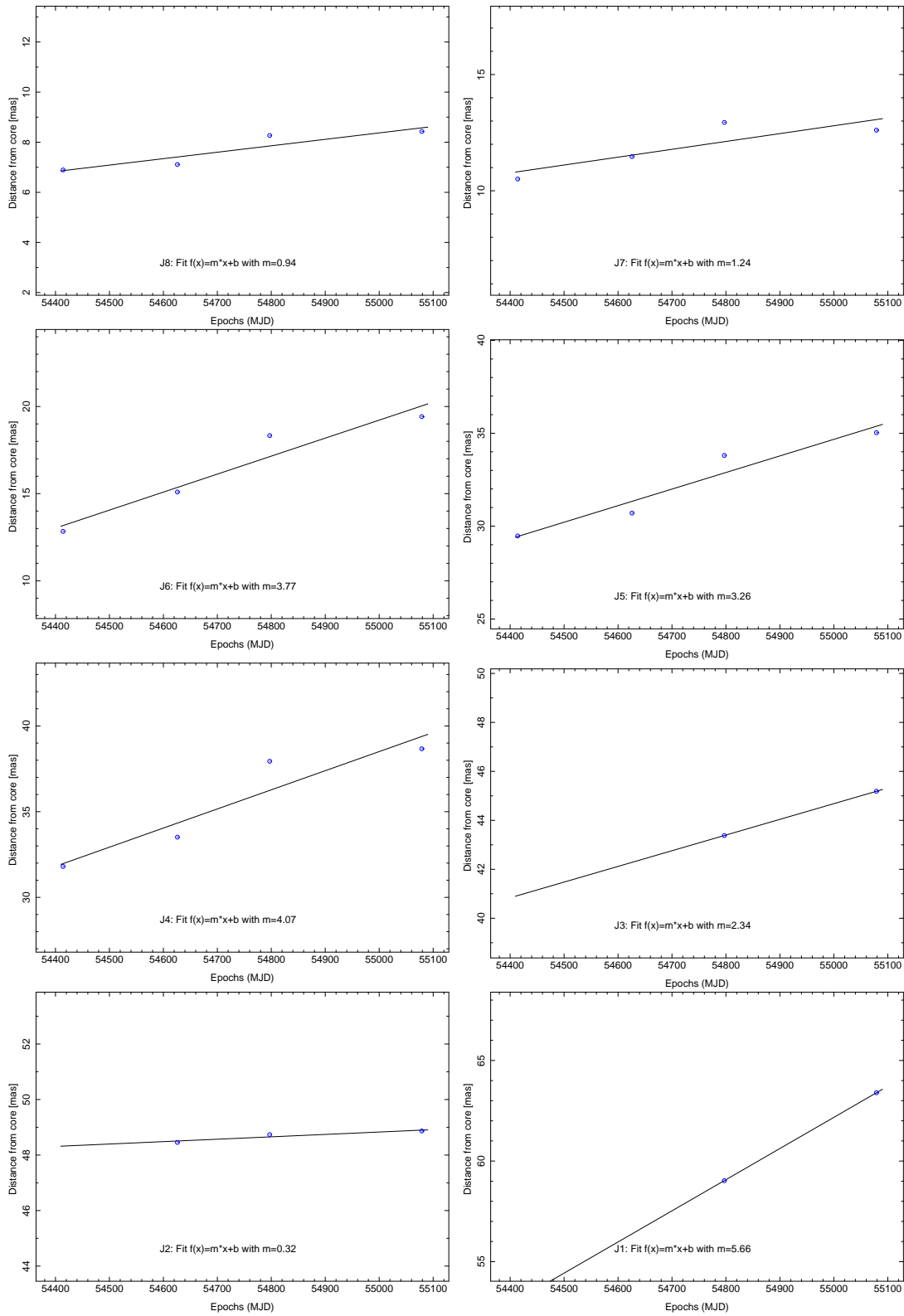
Figure A.8: Unweighted linear regression to the separation of jet components from the designated phase center, m denotes the apparent jet speed in mas yr^{-1} (see also Table 5.3). From top left to bottom right (jet downstream): J8, J7, J6, J5, J4, J3, J2, J1.
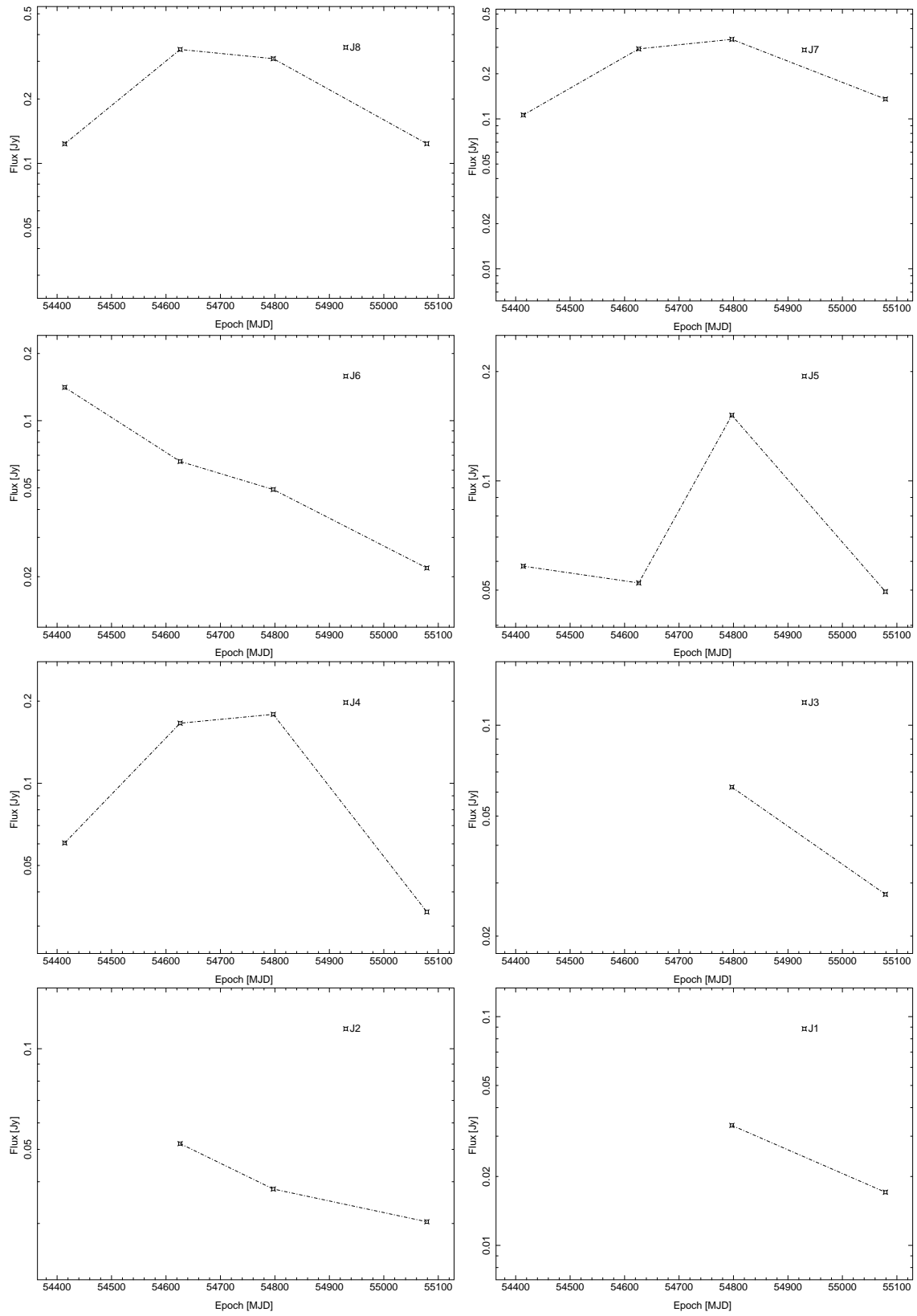
Figure A.9: Flux density evolution of individual components. From top left to bottom right (jet downstream): J8, J7, J6, J5, J4, J3, J2, J1.
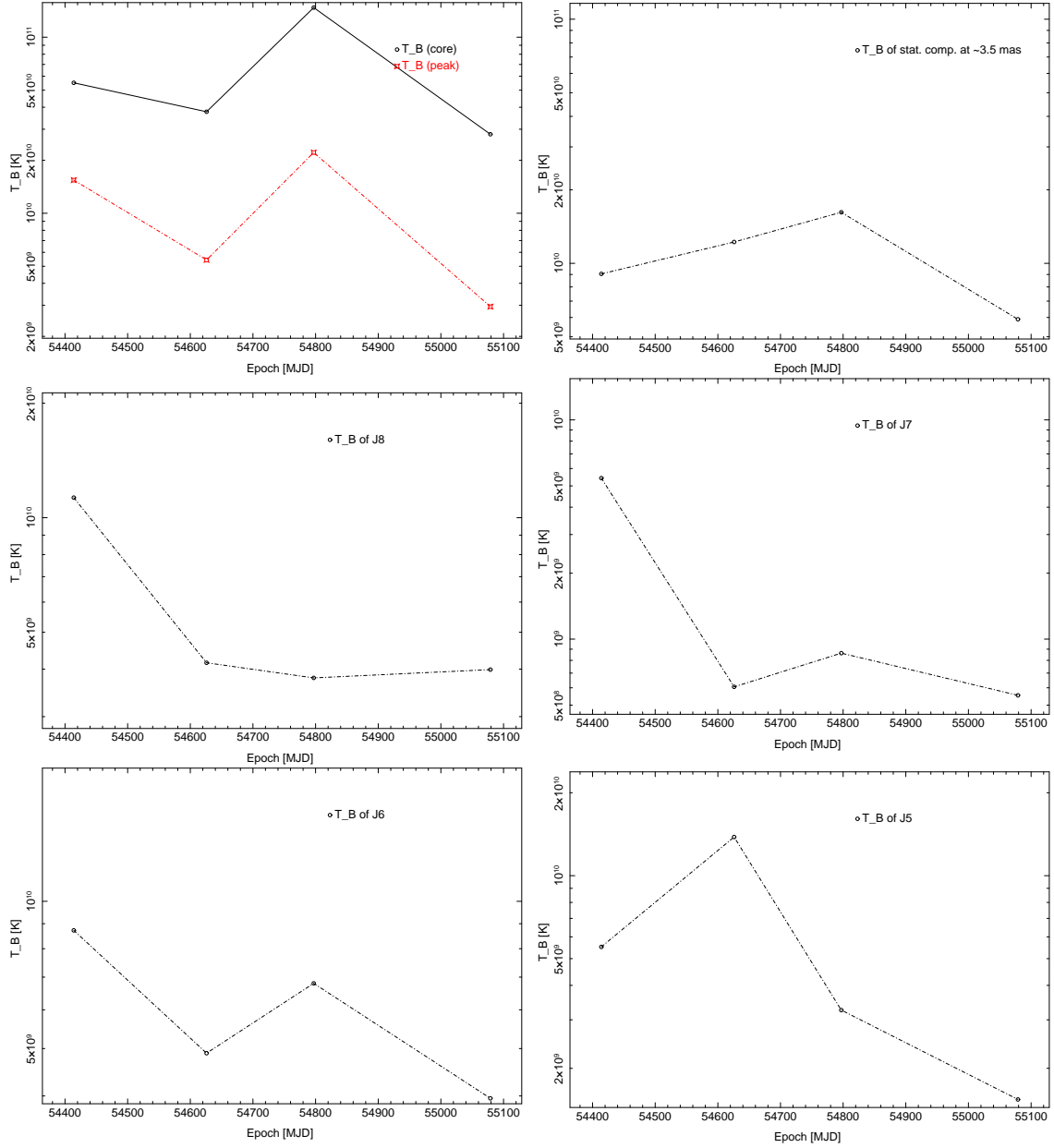
Figure A.10: Brightness temperature evolution of individual components. From top left to bottom right (jet downstream): core component, stationary component J_{stat}, J8, J7, J6, J5. For the core feature, T_{B} is calculated for the peak flux depending on the beam size (red) and for the Gaussian model component identified as the core (black, see Tables A.1 to A.4).
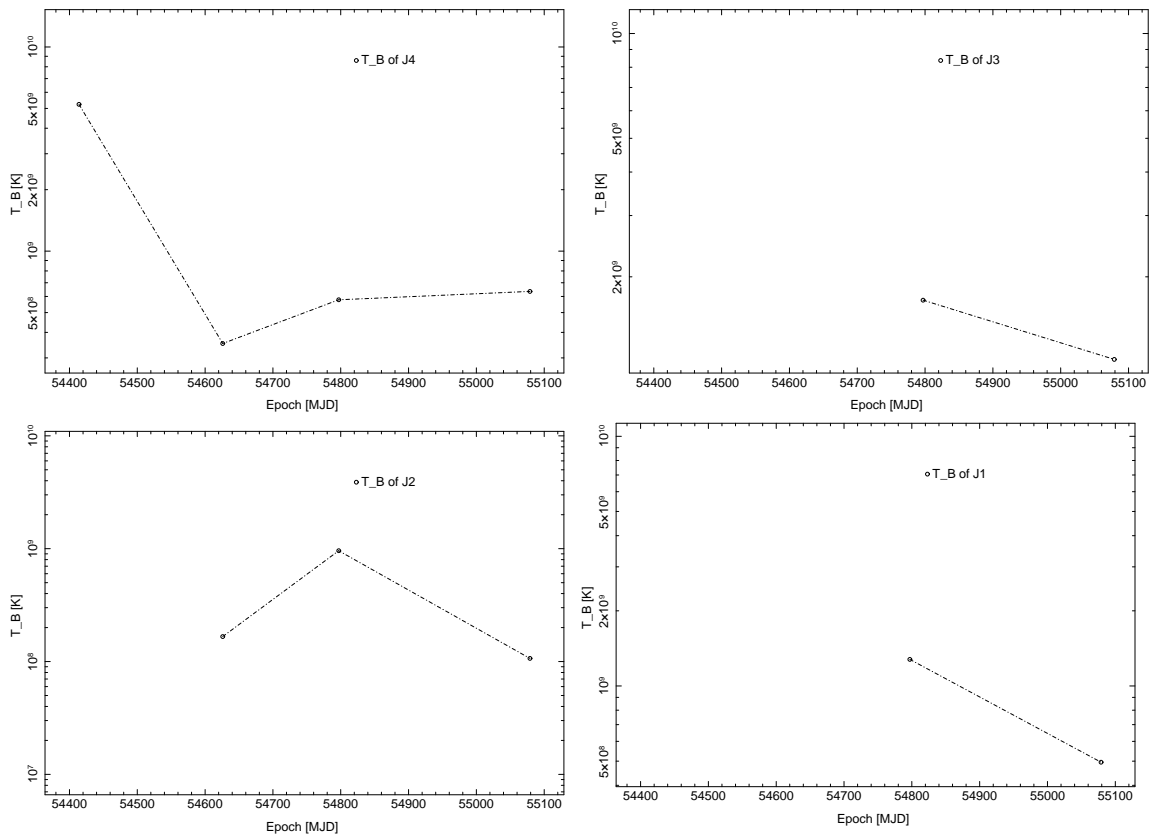
Figure A.10: Brightness temperature evolution of individual components (continued). From top left to bottom (jet downstream): J4, J3, J2, J1.

List of Figures

List of Tables

Bibliography

Abdo A.A., Ackermann M., Ajello M., et al., 2010a, ApJS 188, 405

Abdo A.A., Ackermann M., Ajello M., et al., 2009, ApJ 700, 597

Abdo A.A., Ackermann M., Ajello M., et al., 2010b, Science 328, 725

Abdo A.A., Ackermann M., Ajello M., et al., 2010c, ApJ 719, 1433

Abraham J., Abreu P., Aglietta M., et al., 2009, In: 31st International Cosmic Ray Conference, Lodz, Poland, Vol. 794.

Abraham J., Abreu P., Aglietta M., et al., 2007, Science 318, 938

Aharonian F., Akhperjanian A.G., Anton G., et al., 2009, ApJL 695, L40

Alvarez H., Aparici J., May J., Reich P., 2000, A&A 355, 863

Antonucci R., 1993, ARA&A 31, 473

Antonucci R.R.J., Miller J.S., 1985, ApJ 297, 621

Atwood W.B., Abdo A.A., Ackermann M., et al., 2009, ApJ 697, 1071

Baade W., Minkowski R., 1954, ApJ 119, 215

Baity W.A., Rothschild R.E., Lingenfelter R.E., et al., 1981, ApJ 244, 429

Barthel P.D., 1989, ApJ 336, 606

Becker J.K., Biermann P.L., 2009, Astroparticle Physics 31, 138

Begelman M.C., Blandford R.D., Rees M.J., 1984, Reviews of Modern Physics 56, 255

Benlloch S., Rothschild R.E., Wilms J., et al., 2001, A&A 371, 858

Bevington P.R., Robinson D.K., 2003, Data reduction and error analysis for the physical sciences, Boston: McGraw-Hill

Blandford R.D., Königl A., 1979, ApJ 232, 34

Blandford R.D., Payne D.G., 1982, MNRAS 199, 883

Blandford R.D., Rees M.J., 1978, Physica Scripta 17, 265

Blandford R.D., Znajek R.L., 1977, MNRAS 179, 433

Block D.L., Sauvage M., 2000, A&A 353, 72

Böck M., Kadler M., Tosti G., et al., 2009, In: 2009 Fermi Symposium. eConf Proceedings C091122

Bolton J.G., Clark B.G., 1960, PASP 72, 29

Bolton J.G., Stanley G.J., Slee O.B., 1949, Nature 164, 101

Bond I.A., Ballet J., Denis M., et al., 1996, A&A 307, 708

Bourda G., Charlot P., Le Campion J., 2008, A&A 490, 403

Bowyer C.S., Lampton M., Mack J., de Mendonca F., 1970, ApJL 161, L1

Bridle A.H., Perley R.A., 1984, ARA&A 22, 319

Burke B.F., 1969, Nature 223, 389

Burke B.F., Graham-Smith F., 2002, An Introduction to Radio Astronomy: Second Edition, Cambridge, Cambridge University Press

Burns J.O., Feigelson E.D., Schreier E.J., 1983, ApJ 273, 128

Cappellari M., Neumayer N., Reunanen J., et al., 2009, MNRAS 394, 660

Ciaramella A., Bongardo C., Aller H.D., et al., 2004, A&A 419, 485

Clark B.G., 2003, In: J. A. Zensus, M. H. Cohen, & E. Ros (ed.) Radio Astronomy at the Fringe. ASP Conf. Proc., 300

Clay R.W., Whelan B.J., Edwards P.G., 2010, PASA in press

Cohen M.H., Linfield R.P., Moffet A.T., et al., 1977, Nature 268, 405

Cohen M.H., Lister M.L., Homan D.C., et al., 2007, ApJ 658, 232

Condon J.J., Condon M.A., Gisler G., Puschell J.J., 1982, ApJ 252, 102

Condon J.J., Cotton W.D., Greisen E.W., et al., 1998, AJ 115, 1693

Cornwell T., Braun R., Briggs D.S., 1999, In: G. B. Taylor, C. L. Carilli, & R. A. Perley (ed.) Synthesis Imaging in Radio Astronomy II. ASP Conf. Proc., 180, p. 151

Cornwell T.J., 1989, Science 245, 263

Croton D.J., Springel V., White S.D.M., et al., 2006, MNRAS 365, 11

Cuoco A., Hannestad S., 2008, Phys. Rev. D 78

Daly R.A., Marscher A.P., 1988, ApJ 334, 539

Dauser T., Wilms J., Reynolds C.S., Brenneman L.W., 2010, MNRAS 1460

Deller A.T., Tingay S.J., Bailes M., West C., 2007, PASP 119, 318

Dermer C.D., Gehrels N., 1995, ApJ 447, 103

Di Matteo T., Springel V., Hernquist L., 2005, Nature 433, 604

Diamond P.J., 1995, In: J. A. Zensus, P. J. Diamond, & P. J. Napier (ed.) Very Long Baseline Interferometry and the VLBA. ASP Conf. Proc., 82, p.227

Dunlop J., 1828, Royal Society of London Philosophical Transactions Series I 118, 113

Edge D.O., Shakeshaft J.R., McAdam W.B., et al., 1959, MmRAS 68, 37

Fabian A.C., Iwasawa K., Reynolds C.S., Young A.J., 2000, PASP 112, 1145

Falcke H., Biermann P.L., 1995, A&A 293, 665

Falcke H., Malkan M.A., Biermann P.L., 1995, A&A 298, 375

Fan J.H., Liu Y., Yuan Y.H., et al., 2007, A&A 462, 547

Fanaroff B.L., Riley J.M., 1974, MNRAS 167, 31P

Fath E.A., 1909, Popular Astronomy 17, 504

Fermi E., 1949, Physical Review 75, 1169

Fomalont E., 1981, NRAO Newsletter 3, 3

Fossati G., Maraschi L., Celotti A., et al., 1998, MNRAS 299, 433

Fujisawa K., Inoue M., Kobayashi H., et al., 2000, PASJ 52, 1021

Garofalo D., Evans D.A., Sambruna R.M., 2010, MNRAS 820

Ghez A.M., Klein B.L., Morris M., Becklin E.E., 1998, ApJ 509, 678

Ghisellini G., Celotti A., 2001, A&A 379, L1

Gomez J.L., Alberdi A., Marcaide J.M., 1993, A&A 274, 55

Greisen E.W., 1998, In: R. Albrecht, R. N. Hook, & H. A. Bushouse (ed.) Astronomical Data Analysis Software and Systems VII. ASP Conf. Proc. ,145, p. 204

Greisen K., 1966, Physical Review Letters 16, 748

Grindlay J.E., Helmken H.F., Brown R.H., et al., 1975, ApJL 197, L9

Hardcastle M.J., Worrall D.M., Kraft R.P., et al., 2003, ApJ 593, 169

Hardee P.E., 1986, ApJ 303, 111

Harris G.L.H., Rejkuba M., Harris W.E., 2009, PASA in press

Hartman R.C., Bertsch D.L., Bloom S.D., et al., 1999, ApJS 123, 79

Hartman R.C., Bertsch D.L., Fichtel C.E., et al., 1992, In: C. R. Shrader, N. Gehrels, & B. Dennis (ed.) NASA Conference Publication, Vol. 3137., p.116

Haslam C.G.T., Salter C.J., Stoffel H., Wilson W.E., 1982, A&AS 47, 1

Hinshaw G., Weiland J.L., Hill R.S., et al., 2009, ApJS 180, 225

Hirabayashi H., Hirosawa H., Kobayashi H., et al., 2000, PASJ 52, 955

Hoffmeister C., 1929, Astronomische Nachrichten 236, 233

Högbom J.A., 1974, A&AS 15, 417

Horiuchi S., Meier D.L., Preston R.A., Tingay S.J., 2006, PASJ 58, 211

Hovatta T., Tornikoski M., Lainela M., et al., 2007, A&A 469, 899

Israel F.P., 1998, A&ARv 8, 237

Jaffe W., Ford H.C., Ferrarese L., et al., 1993, Nature 364, 213

Jansky K.G., 1933, Nature 132, 66

Jansky K.G., 2005, In: N. Kassim, M. Perez, W. Junor, & P. Henning (ed.) From Clark Lake to the Long Wavelength Array: Bill Erickson's Radio Science. ASP Conf. Proc., 345, p.3

Jones D.L., Tingay S.J., Murphy D.W., et al., 1996, ApJL 466, L63

Jorstad S.G., Marscher A.P., Larionov V.M., et al., 2010, ApJ 715, 362

Jorstad S.G., Marscher A.P., Lister M.L., et al., 2005, AJ 130, 1418

Jorstad S.G., Marscher A.P., Mattox J.R., et al., 2001a, ApJ 556, 738

Jorstad S.G., Marscher A.P., Mattox J.R., et al., 2001b, ApJS 134, 181

Kachelrieß M., Ostapchenko S., Tomàs R., 2009, New Journal of Physics 11, 065017

Kadler M., 2005, PhD Thesis, Rheinische-Friedrich-Wilhelms-Univ. Bonn, Bonn

Kadler M., Ojha R., Tingay S., et al., 2007, In: Bulletin of the American Astronomical Society, Vol. 38., p. 732

Kellermann K.I., Lister M.L., Homan D.C., et al., 2004, ApJ 609, 539

Kellermann K.I., Moran J.M., 2001, ARA&A 39, 457

Kellermann K.I., Pauliny-Toth I.I.K., 1969, ApJL 155, L71

Königl A., 1981, ApJ 243, 700

Kovalev Y.Y., Aller H.D., Aller M.F., et al., 2009, ApJL 696, L17

Kovalev Y.Y., Lobanov A.P., Pushkarev A.B., Zensus J.A., 2008, A&A 483, 759

Kraft R.P., Forman W.R., Jones C., et al., 2002, ApJ 569, 54

Krolik J.H., 1999, Active galactic nuclei : from the central black hole to the galactic environment, Princeton New Jersey, Princeton University Press, 1999

Krolik J.H., Hawley J.F., 2010, In: T. Belloni (ed.) General Relativistic MHD Jets, Vol. 794. Lecture Notes in Physics, Berlin: Springer, p. 265

Kunkel W.E., Bradt H.V., 1971, ApJL 170, L7

Lagos C.D.P., Cora S.A., Padilla N.D., 2008, MNRAS 388, 587

Lähteenmäki A., Valtaoja E., 2003, ApJ 590, 95

Landt H., Bignall H.E., 2008, MNRAS 391, 967

Lawrence A., 1987, PASP 99, 309

Levenberg K., 1944, Quarterly of Applied Mathematics 2, 164

Lewis J.P., 1995, Vision Interface 95, 120

Lind K.R., Blandford R.D., 1985, ApJ 295, 358

Lister M.L., Aller H.D., Aller M.F., et al., 2009a, AJ 137, 3718

Lister M.L., Homan D.C., Kadler M., et al., 2009b, ApJL 696, L22

Lobanov A.P., 1998, A&AS 132, 261

Lobanov A.P., Zensus J.A., 2001, Science 294, 128

Ma C., Arias E.F., Eubanks T.M., et al., 1998, AJ 116, 516

Malin D.F., Quinn P.J., Graham J.A., 1983, ApJL 272, L5

Marconi A., Risaliti G., Gilli R., et al., 2004, MNRAS 351, 169

Marscher A.P., 2008, In: T. A. Rector & D. S. De Young (ed.) Extragalactic Jets: Theory and

Observation from Radio to Gamma Ray. ASP Conf. Proc. 386, p. 437

Marscher A.P., 2009, In: T. Belloni (ed.) The Jet paradigm - From Microquasars to Quasars, Lecture Notes in Physics, 794., p.175

Marscher A.P., Gear W.K., 1985, ApJ 298, 114

Marscher A.P., Jorstad S.G., 2010, In: Savolainen, T., Ros, E., Porcas, R.W. & Zensus, J.A. (ed.) Proceedings of the Workshop "Fermi meets Jansky - AGN in Radio and Gamma-Rays", Bonn: MPIfR., p.171

Marshall H.L., Miller B.P., Davis D.S., et al., 2002, ApJ 564, 683

McCready L.L., Pawsey J.L., Payne-Scott R., 1947, Royal Society of London Proceedings Series A 190, 357

Meier D.L., Koide S., Uchida Y., 2001, Science 291, 84

Merloni A., Heinz S., 2008, MNRAS 388, 1011

Moderski R., Sikora M., Lasota J., 1998, MNRAS 301, 142

Mücke A., Protheroe R.J., Engel R., et al., 2003, Astroparticle Physics 18, 593

Mueller C., Kadler M., Ojha R., et al., 2009, In: 2009 Fermi Symposium. eConf Proceedings C091122

Müller C., Kadler M., Ojha R., et al., 2010, In: Savolainen, T., Ros, E., Porcas, R.W. & Zensus, J.A. (ed.) Proceedings of the Workshop "Fermi meets Jansky - AGN in Radio and Gamma-Rays", Bonn: MPIfR., p.229

Napier P.J., 1995, In: J. A. Zensus, P. J. Diamond, & P. J. Napier (ed.) Very Long Baseline Interferometry and the VLBA. ASP Conf. Proc., 82, p. 59

Ojha R., Kadler M., Böck M., et al., 2010, A&A 519, A45

Penzias A.A., Wilson R.W., 1965, ApJ 142, 419

Pushkarev A.B., Kovalev Y.Y., Lister M.L., Savolainen T., 2009, A&A 507, L33

Quillen A.C., Brookes M.H., Keene J., et al., 2006, ApJ 645, 1092

Reber G., 1940, ApJ 91, 621

Reber G., 1944, ApJ 100, 279

Richards G.T., Strauss M.A., Fan X., et al., 2006, AJ 131, 2766

Rothschild R.E., Markowitz A., Rivers L., et al., 2010, ApJ, submitted

Rothschild R.E., Wilms J., Tomsick J., et al., 2006, ApJ 641, 801

Rybicki G.B., Lightman A.P., 1979, Radiative processes in astrophysics, New York: Wiley-Interscience

Ryle M., 1952, Royal Society of London Proceedings Series A 211, 351

Ryle M., 1962, Nature 194, 517

Ryle M., Hewish A., 1960, MNRAS 120, 220

Ryle, Sir M., Longair M.S., 1967, MNRAS 136, 123

Salpeter E.E., 1964, ApJ 140, 796

Sambruna R.M., Donato D., Ajello M., et al., 2010, ApJ 710, 24

Saviane I., Jerjen H., 2007, AJ 133, 1756

Schmidt M., 1963, Nature 197, 1040

Schneider P., 2006, Einführung in die extragalaktische Astronomie und Kosmologie, Berlin: Springer

Schwab F.R., Cotton W.D., 1983, AJ 88, 688

Seyfert C.K., 1943, Contributions from the Mount Wilson Observatory / Carnegie Institution of Washington 671, 1

Shakura N.I., Sunyaev R.A., 1973, A&A 24, 337

Shepherd M.C., 1997, In: G. Hunt & H. Payne (ed.) Astronomical Data Analysis Software and Systems VI. ASP Conf. Proc. 125, p. 77

SHEVE Team 1994, In: J. G. Robertson & W. J. Tango (ed.) Very High Angular Resolution Imaging. IAU Symposium, 158, p. 131

Shu F.H., 1991, Physics of Astrophysics, Vol. I, University Science Books, Mill Valley, CA (USA)

Sikora M., Begelman M.C., Rees M.J., 1994, ApJ 421, 153

Sokolovsky K.V., Kovalev Y.Y., Lobanov A.P., et al., 2010, In: Savolainen, T., Ros, E., Porcas, R.W. & Zensus, J.A. (ed.) Proceedings of the Workshop "Fermi meets Jansky - AGN in Radio and Gamma-Rays" (MPIfR, Bonn, June 21-23 2010)., p.167

Steinle H., 2006, Chin. J. of Astron. and Astrophys. Supplement 6, 1

Steinle H., 2010, PASA 27, 431

Steinle H., Bonnell J., Kinzer R.L., et al., 1999, Advances in Space Research 23, 911

Stickel M., Meisenheimer K., Kuehr H., 1994, A&AS 105, 211

Sullivan, III W.T., 1991, In: T. J. Cornwell & R. A. Perley (ed.) ASP Conf. Proc., 19. ASP Conf. Proc., 19, p. 132

Tavecchio F., Ghisellini G., Bonnoli G., Ghirlanda G., 2010, MNRAS 405, L94

Tavecchio F., Maraschi L., Ghisellini G., 1998, ApJ 509, 608

Thompson A.R., Moran J.M., Swenson, Jr. G.W., 2001, Interferometry and Synthesis in Radio Astronomy, 2nd Edition, New York : Wiley

Tingay S.J., Jauncey D.L., Reynolds J.E., et al., 1998, AJ 115, 960

Tingay S.J., Murphy D.W., 2001, ApJ 546, 210

Tingay S.J., Preston R.A., Jauncey D.L., 2001, AJ 122, 1697

Türler M., Paltani S., Courvoisier T., et al., 1999, A&AS 134, 89

Urry C.M., Padovani P., 1995, PASP 107, 803

Valtaoja E., Terasranta H., Urpo S., et al., 1992, A&A 254, 71

Verschuur G., 2007, The Invisible Universe, Berlin: Springer

Voges W., Aschenbach B., Boller T., et al., 1999, A&A 349, 389

Wagner S.J., Witzel A., 1995, ARA&A 33, 163

Walker R.C., 1995, In: J. A. Zensus, P. J. Diamond, & P. J. Napier (ed.) Very Long Baseline Interferometry and the VLBA. ASP Conf. Proc., 82, p. 247

Weisskopf M.C., Brinkman B., Canizares C., et al., 2002, PASP 114, 1

Wells D.C., Greisen E.W., Harten R.H., 1981, A&AS 44, 363

Williams R.E., Blacker B., Dickinson M., et al., 1996, AJ 112, 1335

Wilms J., Kadler M., 2009, Multiwavelength Astronomy, Lecture Notes, FAU Erlangen, http://pulsar.sternwarte.uni-erlangen.de/wilms/teach/multiwave_09/index.html

Wilms J., Kadler M., 2010, Active galactic nuclei, Lecture Notes, FAU Erlangen, http://pulsar.sternwarte.uni-erlangen.de/wilms/teach/agn_10/index.html

Wilson A.S., Colbert E.J.M., 1995, ApJ 438, 62

Winter L.M., Mushotzky R.F., Reynolds C.S., Tueller J., 2009, ApJ 690, 1322

Woltjer L., 1959, ApJ 130, 38

Zensus J.A., 1997, ARA&A 35, 607

Danksagung

Zum Abschluss möchte ich mich bei allen bedanken, die zum Gelingen dieser Arbeit beigetragen haben und mir im Laufe des Studiums mit Rat und Tat zur Seite standen.

An erster Stelle danke ich ganz herzlich meinen beiden engagierten und unermüdlichen Betreuern. Matthias Kadler hat in mir die Begeisterung für Radioastronomie geweckt. Er hat an mich sein Wissen über aktive Galaxien und VLBI-Datenreduktion weitergegeben und war bei jeder Frage und Diskussion ein hilfsbereiter und motivierender Ansprechpartner. Ich danke ihm für seine Zeit, Geduld und die beruhigenden Worte, wenn ich mal wieder fast die Nerven verloren hätte.
Jörn Wilms hat mich stets gefördert, hatte für alle Fragen ein offenes Ohr und hat mir immerzu neue Impulse gegeben. Ich bedanke mich für seine großartige Unterstützung und dafür, dass er sich trotz vieler Termine immer Zeit für ein Gespräch genommen hat.

Mir bedeutet es sehr viel, dass ich schon als studentische Hilfskraft die Möglichkeit bekommen habe, wissenschaftlich für TANAMI tätig zu sein und dabei Einblicke gewinnen und wertvolle Erfahrungen sammeln konnte. Die Aufenthalte am NASA's Goddard Space Flight Center und am Max-Planck-Institut für Radioastronomie in Bonn möchte ich hier nur stellvertretend als unvergessliche Erlebnisse nennen. An dieser Stelle möchte ich auch dem ganzen TANAMI-Team danken, dass sie mich mit der Auswertung der Centaurus A-Daten betraut haben. Insbesondere schätze ich die Zusammenarbeit und die interessanten Gespräche mit Roopesh Ojha und Eduardo Ros sehr und möchte mich bei ihnen für ihre Ratschläge und Hilfsbereitschaft bedanken.

Nichts geht ohne Motivation und den einen oder anderen Witz zwischendurch. Unter den Remeisen herrscht jederzeit eine freundschaftliche und angenehme Atmosphäre, so dass es mir unglaublich Spaß gemacht hat, an der Sternwarte zu arbeiten und aus Kollegen Freunde geworden sind. Ich danke allen für die auflockernden und anregenden Gespräche, ob im Groupmeeting, den Kaffeepausen, auf Konferenzen oder in unserer Fahrgemeinschaftsrunde.
Vor allem möchte ich Manfred, Moritz, Tommy und Felix für die Beantwortung unzähliger Fragen zu ISIS und anderen computertechnischen Problemen und natürlich für das Korrektur-Lesen dieser Arbeit danken. Sie hatten unbeschreiblich viel Zeit und Geduld, mir Tipps zu geben und mir weiterzuhelfen.
Dank der Idee und der Hilfe von Christian Fromm (MPIfR Bonn) wurde die CCC-Methode zur Berechnung von Spektralindexkarten weiterentwickelt. Ich möchte mich bei ihm, Moritz, Christoph und Andrew (RISE student) für die gute Zusammenarbeit an diesem Projekt bedanken.

Dem Max-Weber-Programm Bayern und dem Leonardo Kolleg der Uni Erlangen gilt mein besonderer Dank für die ideelle und finanzielle Förderung während des Studiums. Die Teilnahme an Sprachkursen und Konferenzen war eine ausgezeichnete Ergänzung und der Austausch mit anderen Stipendiaten war für mich persönlich etwas ganz Besonderes.

Die fünf Jahre Physikstudium waren wirklich eine sehr schöne Zeit mit unterhaltsamen Gesprächen, unvergesslichen Tagen in Schweden und vor allem vielen netten Menschen, die mein Leben bereichert haben und die ich nun nicht mehr missen möchte. Meine Mitstreiter, mit ihrer Motivation und Freundschaft, haben mir Durchhaltevermögen gegeben und mich nie den Spaß am Studium vergessen lassen. Ich danke auch den Mitgliedern der FSI Mathe/Physik für die gemeinsamen Stunden und Aktivitäten.

Doch Physik und Wissenschaft allein machen nicht glücklich und so möchte ich mich auch bei den Menschen bedanken, die mir die Augen für das wirklich Wichtige im Leben offen halten. Ich danke meinen Lieben für ihre Unterstützung, ihren Optimismus und für das Ertragen meiner Launen.
Meinen Eltern gebührt der größte Dank. Sie sind immer für mich da, haben mir das Studium ermöglicht und, vor allem, haben sie immer an mich geglaubt.

Hiermit erkläre ich, dass ich die Arbeit selbstständig angefertigt und keine anderen als die angegebenen Hilfsmittel verwendet habe.

Bamberg, 26. November 2010

Cornelia Müller